Tissue Engineering Active Biological Machines: Bio-Inspired Design, Directed Self-Assembly, and Characterization of Muscular Pumps Simulating the Embryonic Heart

Thesis by

Hesham Azizgolshani

In Partial Fulfillment of the Requirements

for the Degree of

Doctor of Philosophy

California Institute of Technology

Pasadena, California

2013

(Defended May 6, 2013)

Acknowledgments

Many years ago, in my childish musings I dreamt of building an artificial heart. I would like to express my gratitude to my advisor, Professor Morteza Gharib, for making it possible for me to pursue this dream through his vision, support, mentorship, understanding, and beyond all, his friendship. I am also grateful to the members of my thesis committee, Professors John Dabiri, Scott Fraser, and Guruswami Ravichandran for their guidance, encouragement, and resourcefulness.

I would like to thank Martha Salcedo for her daily support, Mark Gonzales at the PMA machine shop for the many skills he taught me during the years I sought his advice, and David Kremers for the many intellectual conversations we had.

I owe a great deal of my scientific success to my father, Houshang Azizgolshani, who promoted and encouraged my curiosity and creativity from an early age; no naïve or ambitious project of mine ever met resistance from him, be it my plan to build the impossible perpetual motion machine by connecting two small electric motors end-to-end to generate electricity with one to power the other or building a mirror telescope from scratch by carving its concave mirror. He always supported me through failure and success. I have always attributed my ability in working with my hands, which undoubtedly has strengthened my power of imagination, to my mother, Yafeh Behmanesh, who has also been an example of resilience and perseverance for me. I would not have been the person I am, were it not for my sister, Odisse Azizgolshani, who has been my role model and friend through the entirety of my life. And I owe a great deal of happiness to the love of my life, Annette Lienau, who has brought me multitudes of joy from the day I met her through her unconditional love and care.

My labmates, past and present, have also played a significant role in my growth both scientifically and personally; I would like to thank Derek Rinderknecht, Taly Lindner, Julia Cosse, Haejin Kang,

Daegyoum Kim, Niema Pahlevan, Indrat Aria, Brad Lyon, Francisco Pereira, Emilio Graff, John Meier, Matthew Munson, Anya Grosberg, Nikoo Saber, Jian Lu, David Jeon, and Elijah Sansom for their friendship and support.

Among my friends, I would like to especially thank Jason Perez, Laura Book, Esfandiar Alizadeh, Paula Popesco, Kakani Young, Mélanie Guittet, and Ajay Gopal for the many pleasant memories we shared, many of which revolved about good food and company.

Lastly, I would like to acknowledge the profound influence that nature has had on me over the latter half of my graduate studies. Taking care of trees has been a source of inspiration and a sense of greater purpose, and seeing them grow has been a source of joy and awe.

Abstract

Biological machines are active devices that are comprised of cells and other biological components. These functional devices are best suited for physiological environments that support cellular function and survival. Biological machines have the potential to revolutionize the engineering of biomedical devices intended for implantation, where the human body can provide the required physiological environment. For engineering such cell-based machines, bio-inspired design can serve as a guiding platform as it provides functionally proven designs that are attainable by living cells. In the present work, a systematic approach was used to tissue engineer one such machine by exclusively using biological building blocks and by employing a bio-inspired design. Valveless impedance pumps were constructed based on the working principles of the embryonic vertebrate heart and by using cells and tissue derived from rats. The function of these tissue-engineered muscular pumps was characterized by exploring their spatiotemporal and flow behavior in order to better understand the capabilities and limitations of cells when used as the engines of biological machines.

Contents

List of Figures **ix**

1 Introduction **1**

1.1 Motivation 1

1.2 Biological Machines: Potential Advantages and Limitations 4

1.3 Insights from the Heart and Cardiac Tissue Engineering 4

1.3.1 The Makeup of the Heart 5

1.3.2 Cardiac Tissue Engineering 5

1.4 Biologically Driven Muscular Pumps 7

2 Tissue Engineering Cell-Based Pumps **8**

2.1 Pumps in Nature 8

2.2 Biological Inspiration for the Cell-Based Pump: Studies of the Embryonic Zebrafish Heart 10

2.3 The Impedance Pump 10

2.3.1 Studies of Valveless Pumping Mechanism 10

2.3.2 General Characteristics of the Impedance Pump 11

2.3.3 Components of an Impedance Pump 13

2.3.4 The Effects of Excitation Parameters on the Pump Performance 13

2.3.4.1 The Effect of Excitation Frequency on the Flow Behavior 14

2.3.4.2 The Effect of Excitation Location on the Flow Behavior 15

2.3.4.3 The Effect of Excitation Amplitude and Width on the Flow Behavior 15

2.3.5 The Effects of the Pumping Element Parameters on the Pump Performance . 15
2.3.5.1 The Effect of Tube Mechanical Properties on the Flow Behavior . . 16
2.3.5.2 The Effect of Tube Geometric Properties on the Flow Behavior . . . 16
2.3.6 The Effects of the System Parameters on the Pump Performance 16
2.3.6.1 The Effect of Fluid Density and Viscosity on the Flow Behavior . . 17
2.3.6.2 The Effect of Systemic Resistance on the Performance of the Pump 17
2.3.6.3 The Effect of Transmural Pressure on the Performance of the Pump 17
2.3.6.4 The Effect of System Compliance on the Performance of the Pump 17
2.4 Biological Components for Tissue Engineering the Pump 18

3 Enabling Tools and Techniques 20

3.1 Cell and Tissue Harvest 20
3.1.1 Primary Harvest of Cardiac Muscle Cells 20
3.1.2 Harvest and Decellularization of Small Intestinal Submucosa 23
3.2 Bioreactor Design 24
3.2.1 General Design considerations 24
3.2.2 Bioreactor Components 25
3.3 Integration of the Actuator and the Pump Body: Tissue Engineering the Pumps . . 28
3.4 Electrical Stimulation 29
3.5 Imaging and Microscopy 30
3.5.1 Fluorescent Staining and Microscopy 30
3.5.2 Image Capture and Stereomicroscope Setup 31
3.5.3 Calibration Curve 32
3.5.4 Flow Visualization 33
3.6 Image Processing 34
3.6.1 Finding the Boundaries of the Moving Tube 35
3.6.2 Particle Tracking Velocimetry 40

4 Characterization of the Tissue-Engineered Pumps **42**

4.1 Raw Data and Preliminary Data Processing 42

4.2 Emergence of Contractile Patterns in the Tissue-Engineered Constructs 45

4.3 Frequency Response Characterization of a Fully Seeded Tissue-Engineered Pump . . 52

4.3.1 Tube Dynamics under Forced Electrical Stimulation 53

4.3.2 Flow Response under Forced Electrical Stimulation 59

4.4 Frequency Response Characterization of a Selectively Seeded Tissue-Engineered Pump 65

4.4.1 Tube Dynamics under Forced Electrical Stimulation 65

4.4.2 Flow Response under Forced Electrical Stimulation 74

5 Concluding Remarks and Future Directions **78**

5.1 Future Directions 79

5.1.1 Physical Stimuli for Cellular and Subcellular Organization 79

5.1.2 Addition of Valves as the Next Developmental Stage 80

5.1.3 Stem Cells for Tissue Engineering Muscular Pumps 81

A Error in Finding the Tube Profile **82**

B Calculating the Depth of Field for the Stereomicroscope in Relation to PTV Software **85**

Bibliography **87**

List of Figures

1.1 Conceptual framework for the tissue-engineered muscular pumps. 3

2.1 Biomechanics of the embryonic heart tube. 11

2.2 Liebau's original model, demonstrating valveless pumping. 12

2.3 A simplified schematic depicting the process of wave reflection and generation of flow in the Liebau phenomenon. 13

3.1 The bioreactor and its major components. 26

3.2 The assembled bioreactor with a tissue-engineered pump attached to the flow-loop. . . 27

3.3 Selective seeding of cardiomyocytes to create muscular band actuators. 28

3.4 Schematic diagram for the electrical stimulation setup. 30

3.5 Stereomicroscope calibration curve. 32

3.6 The flow-loop used for flow characterization of the tissue-engineered pumps. 33

3.7 Edge detection for the ideal case of a binary representation of the tube. 36

3.8 Edge detection for the case of a complex tube. 38

4.1 Representative images of the tubular pump at two time points. 43

4.2 Representative images of the tracer particles tracked at two time points. 44

4.3 Superposition of the tube profile for a spontaneously contracting tissue-engineered construct monitored for four consecutive days. 46

4.4 Deviations from mean diameter for a spontaneously contracting tissue-engineered construct. 48

4.5 Temporal profile of the tube's spontaneous contractions. 49

4.6 Spectral analysis of tube contractions for the spontaneously contracting tissue-engineered construct. 51

4.7 Contraction ratios along the longitudinal axis of the pump body for a fully seeded muscular pump under forced electrical stimulation. 54

4.8 Deviations from the mean diameter at two points of interest on a fully seeded muscular pump. 57

4.9 Spectral analysis of tube contractions for a fully seeded muscular pump. 58

4.10 Time and frequency domain representation of selected tracer particle displacements in response to the flow generated by the fully seeded pump. 60

4.11 Mean velocity profile in the flow-loop as generated by the fully seeded muscular pump. 63

4.12 Magnitude of mean volumetric flow rate as a function of the frequency of excitation for the fully seeded muscular pump. 64

4.13 Bright field and fluorescent Z-section images for a selectively seeded region of SIS tube showing the fluorescently labeled nuclei of the cells. 66

4.14 Contraction ratios along the longitudinal axis of the pump body for a selectively seeded muscular pump under forced electrical stimulation. 68

4.15 Temporal representation of the contraction ratio for a selectively seeded muscular pump. 69

4.16 Spectral analysis of tube contractions for a selectively seeded muscular pump. 70

4.17 Displacement time-course for the point of maximum contraction for a partially seeded pump. 72

4.18 Wall displacement velocity profile for the point of maximum contraction for the muscular band actuated pump. 73

4.19 Time and frequency domain representation of selected tracer particle displacements in response to the flow generated by the partially seeded pump. 75

4.20 Mean velocity profile in the flow-loop as generated by the partially seeded muscular pump. 76

4.21 Magnitude of mean volumetric flow rate as a function of the frequency of stimulation for the muscular band actuated pump. 77

A.1 Error associated with the edge detection algorithm. 83

B.1 The fraction of particles recognized by the particle tracking program at out-of-focus planes. 86

Chapter 1

Introduction

1.1 Motivation

Biological machines are active devices that are comprised of cells and other biological components. As the constituent materials of biological machines involve living cells and biologically derived or biocompatible building blocks, an inseparable link exists between engineering of biological machines and the field of tissue engineering. In fact, the broad definition of biological machines offered here encompasses many of the goals and objectives of tissue engineering and regenerative medicine. Nevertheless, distinctions exist. Many of tissue engineering's achievements in replacing diseased or damaged tissue are concerned with aggregates of cells on suitable scaffolding materials that provide a desired form. Although these tissues are functional, they could be considered as passive, with no higher function beyond that of the constituent cells and the form provided by the scaffolding matrix. Examples include tissue-engineered skin replacements, cartilage, and vascular grafts [49, 57, 63]. These tissue-engineered constructs can not be considered as biological machines since they mainly perform static and structural functions. Additionally complex biological machines have been envisioned, and simpler ones such as swimming and walking machines have been devised that are not intended for therapeutic purposes [35, 13, 52]. The objective of the work presented in this thesis was to design and engineer an active biological machine with potential use as a biomedical device.

Active fluid transport is a vital process in many living organisms. Furthermore, a large number of biomedical devices involve transport of fluids. The importance and relevance of fluid transport

motivated us to build a pump exclusively out of biological components as an example of active biological machines. In designing the pump, we were guided by previous observations and studies of the pumping mechanism of the embryonic vertebrate heart. In its earliest functional stage, the vertebrate heart is a valveless tubular organ with a contractile region, which generates pulsations traveling through the myocardium and pumps blood through the simple vascular network of the embryo [20, 50]. The pumping mechanism of this relatively simple heart is attributed to elastic wave propagation and reflection in the heart tube, a phenomenon known as the Liebau effect and discussed in further detail in Chapter 2.

The embryonic heart tube can be reduced to two major components in a physical model known as impedance pumping. A band of active cardiomyocytes constitutes the actuator in this model and the myocardial and endocardial layers along with the cardiac jelly constitute an elastic tube. As the cardiomyocytes contract, a bidirectional wave is originated and then reflected at the inflow and outflow tracts that have different impedances compared to the heart tube. The interference of the incoming waves with the reflected ones results in a net positive flow under the proper frequency of excitation [20].

The bio-inspired approach taken in the design of our tissue-engineered pump was advantageous for several reasons. First and foremost, the embryonic heart provided us with a functionally proven system capable of generating flow. Through years of evolution, this pumping mechanism has demonstrated its reliability and robustness that has meant the survival of the organism. Analogous developmental steps in the early stages of heart development among lower and higher vertebrates of various sizes indicates the scalability of this pumping mechanism that is also shown in the experimental investigations of the physical model [75, 55, 47, 29]. Furthermore, the ability of a small number of cardiac muscle cells to achieve this function at an early stage of development, while the cardiac conduction system has not yet developed, pointed to a relatively simple design that required minimal coordination [50].

Designs in nature have general features as opposed to rigid design specifications that would require exact duplication [4]. Borrowing these design features can afford a level of fault tolerance.

These observations convinced us that this pumping mechanism would be a suitable candidate for constructing a cell-based pump since it does not require valves, rotary elements, or complicated coordinated signals as required for other biologically occurring pumps like the peristaltic pumps in the digestive system of animals [72].

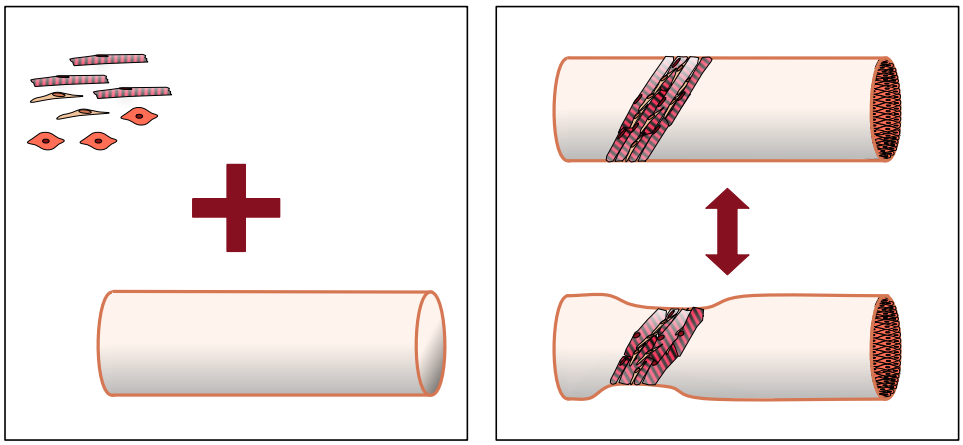

Figure 1.1. Conceptual framework for the tissue-engineered muscular pumps. Left: Functional elements of the pump, the actuator and the elastic tube (here cardiac cells and decellularized tissue from rats), as conceptualized in a cell-based pump. Right: Ideally, the cardiomyocytes are aligned and integrated with the tube into a contracting band which takes on the role of the actuator.

To tissue engineer such a valveless heart out of biological building blocks, two major components of the pump need to be realized and integrated: the elastic tube and the actuator. There have been many advances in the field of vascular tissue engineering which aided us in achieving the first component, that is, a biocompatible elastic tube [63]. For this purpose, we chose small intestinal submucosa (SIS), which is a decellularized tubular scaffold [41]. A number of research groups have been successful in using muscles as actuators in mechanical devices [74, 15, 66, 19]. We chose cardiac muscle cells or cardiomyocytes to realize the actuator element of the cell-based pump.

1.2 Biological Machines: Potential Advantages and Limitations

Biological machines could be thought of as devices powered through biological means. Such machines possess potential advantages over machines made out of traditional nonbiological components because of the unique properties of living cells. For example, these machines have the ability to metabolize their energy requirements from the food readily available in their physiological environment, eliminating the need for external energy sources such as batteries to power them. They also have the potential to self-repair, reorganize, and adjust to changes in their environment, owing to the regenerative and adaptive properties of their constituent cells. Furthermore, biological machines may have significant implications for biomedical devices, as the use of cells from patients could resolve the biocompatibility problem.

One the other hand, machines made out of living components have their own limitations that ought to be acknowledged. Many external factors affect the function of the cells. In the absence of a homeostatic regulatory system, these living machines are limited to environments with favorable conditions that support cellular function and survival. Furthermore, as the complexity and size of these machines increase, limited transport of gasses, nutrients, and wastes through diffusion becomes insufficient and the need for a circulatory system becomes necessary.

1.3 Insights from the Heart and Cardiac Tissue Engineering

Ideally, to grow such a primitive heart out of biological components, one would follow the developmental stages of the heart which involves a series of coordinated processes of cell proliferation, differentiation, and rearrangement. This, if even possible, would require a complete understanding and control over cell behavior, a knowledge and ability that we currently lack. Inevitably, we are forced to use tissue engineering techniques to reach our goal. It is then necessary to take a closer look at the makeup of the heart and some of the advances that have been made in the field of cardiac tissue engineering.

1.3.1 The Makeup of the Heart

Native cardiac tissue has different levels of organization. On the cellular level, cardiomyocytes along with cardiac non-myocytes form lamellae of parallel cells. These cells are structurally connected to each other through cell adhesion proteins such as cadherins, as well as to the weaves and struts of the collagen matrix of the heart [8]. On a subcellular level, cardiomyocytes possess a well-structured cytoarchitecture which enables their effective contraction. Cardiac cells are also connected chemically through gap junctions, and the heart relies on the synchronous activity of its cells to effectively pump blood in the body [38].

Although cardiac myocytes compose the bulk of the volume of the myocardium, in terms of population, cardiac fibroblasts are the most numerous cell type within the heart [5]. Function of fibroblasts in maintaining the structure of myocardial tissue is well established. Fibroblasts are involved in remodeling the extracellular matrix through their biochemical activities, including extracellular matrix protein secretion and matrix metalloproteinase activity [11]. More recently, it has been demonstrated that cardiac fibroblasts directly contribute to the electrophysiological properties of cardiac tissue. Fibroblasts have been shown to form gap junctions with cardiomyocytes in both native myocardium and culture, aiding the synchronization of electrical activity in the cardiac tissue over extended distances. Nevertheless, overgrowth and abnormal activity of fibroblasts can have adverse effects on cardiac function as is the case in many diseased states of the heart [24, 9].

1.3.2 Cardiac Tissue Engineering

Tissue engineering is an emerging field with the goal of developing cell, tissue, and organ substitutes for repair or replacement of lost or impaired biological function. Cardiac tissue engineering is concerned with the aforementioned endeavors which relate to the heart. In itself, cardiac tissue engineering seeks to find solutions for different structures of the heart including the heart muscle, the heart blood vessels, and the trileaflet valves of the heart [39]. The discussion that follows focuses on myocardial tissue engineering as it relates to the engineering of muscular pumps.

One stark difference between developing native cardiac tissue and tissue-engineered cardiac con-

structs is the order in which form and extracellular matrix appear. In the myocardium, shape precedes the formation of the collagen network [7]. On the contrary, current limitations in tissue engineering require us to provide the cells with a scaffolding matrix to dictate the shape of the construct. The substrate stiffness has long been known to influence cells in their morphology, cytoskeletal structure, and adhesion–cellular responses that influence cellular function. In particular, cardiomyocytes have been shown to respond to the non-optimal stiffness of their substrate with loss of function. Harvested cardiomyocytes cultured on rigid surfaces cease to beat rhythmically and lose their contractility compared to the ones cultured on softer substrates matching the micro-elasticity of the native myocardium [17].

Overwhelming evidence has emerged in recent years on the role of cardiac fibroblasts in cardiac function. Coculture of cardiac myocytes and fibroblasts has been reported to have superior contractile properties compared to the culture of cardiomyocytes alone, showing higher contraction amplitudes and lower excitation thresholds [25]. These pieces of evidence suggest the importance of a balanced cell population including both cardiac myocytes and fibroblasts in order to achieve full functionality in the tissue-engineered cardiac constructs.

Probably, the biggest challenge facing cardiac tissue engineering is achieving global and cellular levels of organization, alignment, and synchrony within the tissue-engineered constructs. Patterning of cells in monolayers through techniques such microcontact printing have been successful in recapitulating some of these levels of organization, but such techniques are not suitable for tissue engineering three-dimensional cardiac tissue [1, 19]. In the developing heart, along with biochemical factors, many biophysical factors such as mechanical and electrical stimuli are present and are believed to play a significant role in regulating the structure and function of the myocardial tissue. With the aid of bioreactors that replicate some of these physical stimuli, a number of the distinct structural and functional features of cardiac tissue have been achieved in tissue-engineered constructs, yet the successful capturing of all these features remains illusive [25].

1.4 Biologically Driven Muscular Pumps

There have been a limited number of attempts in the past to build cell-based muscular pumps *in vitro* [66, 67, 60, 40]. These attempt have mainly relied on sheets of cultured cardiomyocytes that were used as actuators. Net flow generation was only achieved through incorporation of check valves and was three orders of magnitude smaller than the flow generated in our studies [66, 67]. Others have not demonstrated generation of flow and have only established increases in the internal pressure upon actuation by the muscle sheets [60, 40].

Other attempts have also been made in making pumps using the decellularized matrix of cadaveric hearts as a template. In these studies, the scaffolding matrix was recellularized with live cardiomyocytes that populate the decellularized matrix and generate contractions [54]. The success of this approach has been limited, though, and only 2% of cardiac function was regained. In the chapters that ensue, we describe our approach to tissue engineering muscular pumps based on the working principles of the embryonic vertebrate heart and by using cardiomyocytes as actuators on a decellularized tubular scaffolding matrix.

Chapter 2

Tissue Engineering Cell-Based Pumps

In pursuit of a suitable design for the cell-based pump, Section 2.1 takes a look at some of the various pumping mechanisms employed in nature. Section 2.2 explores the pumping mechanism in the embryonic vertebrate heart tube which served as the biological inspiration for the cell-based pump that we have tissue engineered. An understanding of the physical principles governing the function of the pump is important. Section 2.3 provides the relevant background with an emphasis on the experimental observations relating to the effects of the parameters that influence the pump's function. Section 2.4 identifies the biological components for the pump and describes the criteria that was used for their selection.

2.1 Pumps in Nature

A pump can be defined as a device that moves fluids against a resistive load by mechanical action. The balance of forces requires a pressure gradient to exist across the fluid for it to move, and a pump achieves this task by performing work and adding energy to the fluid.

Pumps are essential for the survival of many biological organisms as they represent a major mechanism for the delivery of vital fluids in multicellular organisms for which transport of gasses, nutrients, and wastes merely through diffusion is not sufficient. Through the course of evolution, biological organisms have developed many diverse pumps, both in form and function, to meet their

needs.

Regardless of being manmade or naturally occurring, pumps can be classified into two distinct categories based on the mechanism by which energy is delivered to the fluid: displacement pumps and dynamic pumps [36, 72]. Displacement pumps impart energy to the fluid by repeated application of force through the movable boundary of an enclosed, fluid-containing chamber, resulting in a direct increase of pressure to impel fluid. Dynamic pumps continuously add kinetic energy to the system and increase the flow velocity to values greater than those occurring at the discharge such that the subsequent velocity decrease will result in an increase in pressure and hence propelling the fluid [36]. These distinct categories of pumps achieve their function through various mechanisms that involve components such as pistons, valves, and propellers–many of which are also utilized by living organisms.

Ciliary pumps of bivalve gills of suspension feeders such as mussels and clams constitute a dynamic pump as they use the repeated and synchronous motion of their protruding cilia to move water across their gill [71, 72]. Evaporative sap lifters of trees are displacement pumps that use the local changes in the volume of liquid due to evaporation of water from the leaves to lift the continuous column of liquid water from the roots against large pressure heads and systemic resistances [72]. Peristaltic pumps of the digestive systems of animals that use waves of contraction to displace boluses of highly viscous fluids down their muscular tubes are another example of displacement pumps in nature [71, 72]. Perhaps, the most recognized pump in nature is the familiar adult four-chambered heart that pumps the blood through our circulatory system. This valve-chamber displacement pump has its origins in a simpler valveless form before it develops its compartments that are separated by valves. This primitive form of the heart is the subject of the discussion in the following section.

2.2 Biological Inspiration for the Cell-Based Pump: Studies of the Embryonic Zebrafish Heart

As mentioned earlier in Chapter 1, the embryonic vertebrate heart has served as the biological inspiration for the design of the muscular pumps that are described in the present work. The pumping mechanism of this valveless stage of the heart and the studies that led to its discovery are deserving of further discussion.

Studies performed on zebrafish heart tube have revealed a valveless pumping mechanism that is based on elastic wave propagation and reflection [20, 21]. Visualization of the heart tube wall's motion combined with the motion of the blood cells for this primitive stage of the heart provided quantitative evidence for this conclusion. For example, bidirectional waves traveling the endocardial layer of the heart tube suggest generation and propagation of waves from the location of contraction, as depicted in the schematic diagrams of Figure 2.1. Furthermore, visible reflection of these waves at the inflow and outflow tracts of the heart tube along with nonlinear flow response to the frequency of contraction and presence of resonance peaks point to interactions of the outgoing and incoming waves in the heart tube. The characteristics of this wave based pumping mechanism which is known as Liebau phenomenon or impedance pumping is the topic of the discussion in Section 2.3.

2.3 The Impedance Pump

2.3.1 Studies of Valveless Pumping Mechanism

The Liebau phenomenon, also known as impedance pumping, was first recognized by Gerhart Liebau during his observations and investigations of the human circulation. It is a valveless pumping mechanism which utilizes a systematic asymmetry in the fluid-structure system to generate flow [56, 47]. In 1954, Liebau demonstrated the potential for valveless pumping by connecting two elastic tubes of different diameters in an arrangement similar to that of Figure 2.2 and used periodic

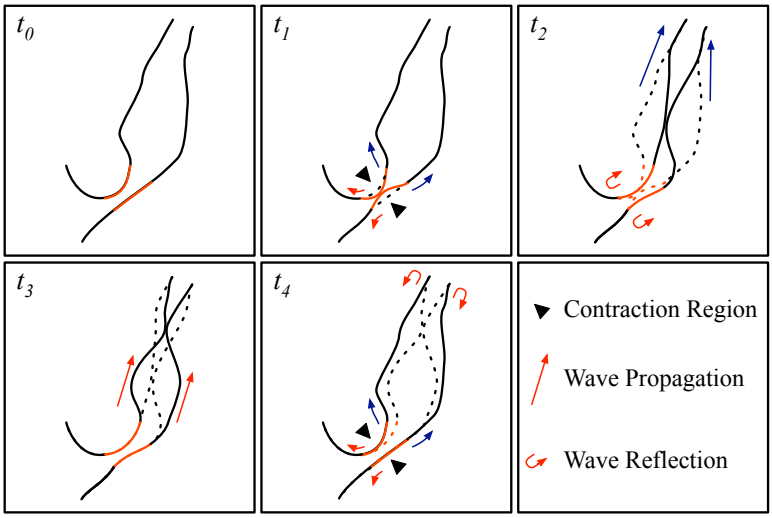

Figure 2.1. Biomechanics of the embryonic heart tube. Bidirectional waves originate from the active contractile region of the heart tube and travel towards the inflow and outflow tracts of the heart where they encounter a mismatched impedance. This mismatched impedance results in the reflection of the traveling waves and creation of a suction region which drives the flow of blood in the vascular network of the embryo. Figure adapted from [21].

compression of the larger diameter tube to move a fluid from a lower reservoir to a higher one, generating flow against a pressure head [44]. Since Liebau's first demonstration, several different closed and open arrangements have been devised where the pumping mechanism is attributed to the Liebau phenomenon. There have been many analytical, computational, and experimental studies to uncover the underlying physical principles responsible for the Liebau phenomenon, but no single model fully captures the observed experimental behavior exhibited, due to the large number of parameters involved that influence the performance of the pump [51, 2, 3, 29, 47]. Yet, it is instructive and elucidating to consider some relevant studies and characteristics before embarking on tissue engineering a pump *in vitro* based on the principles of the valveless pumping.

2.3.2 General Characteristics of the Impedance Pump

It has been suggested that the response of the fluid to the impedance of the system is responsible for generation of flow in Liebau phenomenon, that is, the fluid takes the path of least instantaneous resistance across a dynamic pressure gradient [51, 47]. This response of the fluid can explain the

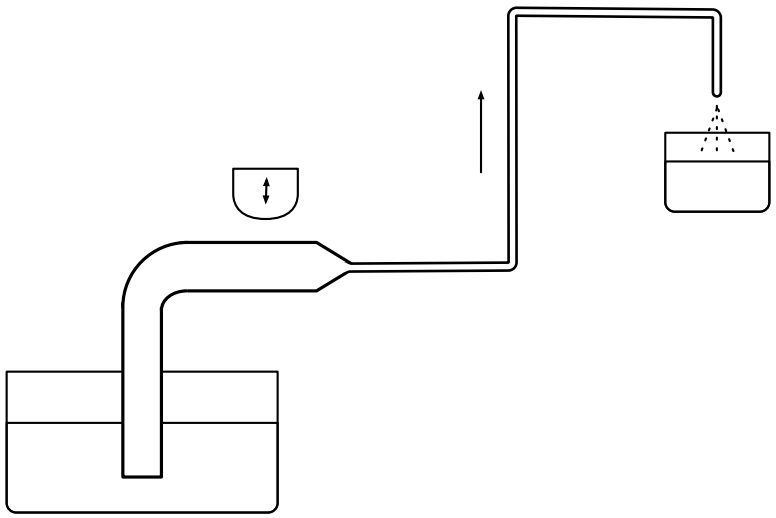

Figure 2.2. Liebau's original model, demonstrating valveless pumping. Rhythmic compressions of a large diameter tube coupled to a smaller diameter tube pumps water from a reservoir to a higher one. Figure adapted from [44].

observed generation of flow. Other observations have recognized the significance of mechanical wave impedances on the wave dynamics in the elastic tube for the induction of flow in the valveless impedance pump [29, 3, 47]. These studies point to the interactions of incoming and reflected waves in generating the observed flow.

Several parameters have been identified that significantly affect the performance and characteristic behavior of the impedance pump [30, 47]. These parameters arise from three distinct sources, two of which, the actuator and the pumping element are components of the pump, and the other is a consequence of the working fluid and the system in which the pump operates on [47]. Temporal parameters of excitation such as frequency drastically affect the flow. Spatial parameters of the excitation such as the amplitude, location, and width of the actuator play a significant role in the flow behavior. Geometric and material properties of the pumping element such as length, diameter, wall thickness, and modulus of elasticity determine the dominant parameters that influence the performance of the pump and alter the response of the pump to these parameters. Parameters external to the pump such as the density and viscosity of the working fluid, as well as the resistance and the compliance of the system also alter the performance of the pump [30, 47].

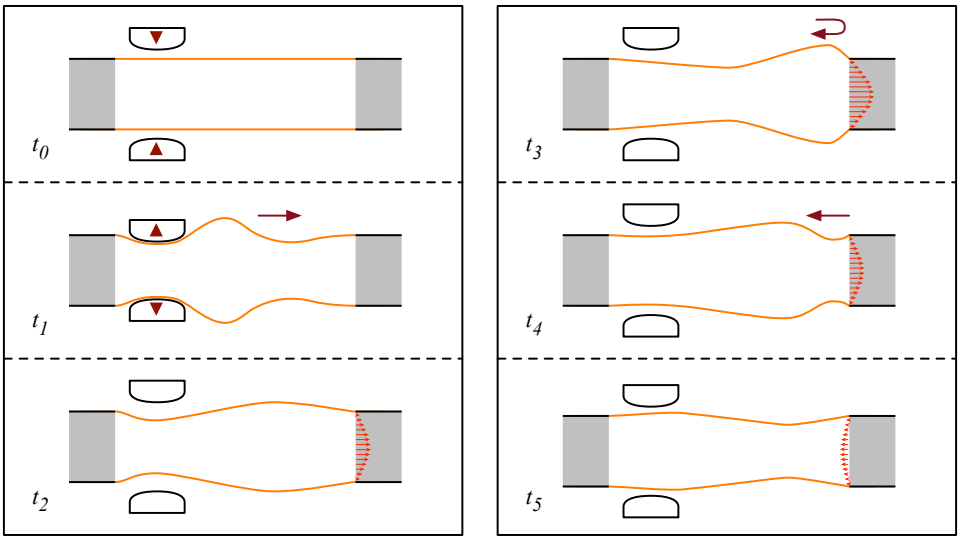

Figure 2.3. A simplified schematic depicting the process of wave reflection and generation of flow in the Liebau phenomenon. An elastic tube is actuated asymmetrically from both ends (t_0). The elastic wave generated to the right of the actuator travels to the end of the tube (t_1–t_3) and generates positive flow due to build up of pressure across the pump. The elastic wave partially reflects (t_3) and travels back toward the actuator (t_4). Due to the absence of valves, the pump exhibits an oscillatory flow characteristic, which can lead to back-flow of the fluid (t_5).

2.3.3 Components of an Impedance Pump

In its simplest form, an impedance pump is comprised of an actuator and an elastic tube coupled at both ends to wave reflection sites. Wave reflection sites may be devised in practice by coupling of the elastic tube with materials of different mechanical properties or by means of geometrical differences such as sudden changes in diameter or wall thickness at the tube ends [56]. The impedance pump can be part of a closed-loop system or an open configuration. In the closed-loop configuration, the function of the pump results in continuous circulation of the fluid in the system. In the open configuration where the pump is connected to two reservoirs, the pump can move the fluid from one reservoir to another against a pressure head [47].

2.3.4 The Effects of Excitation Parameters on the Pump Performance

As mentioned earlier, temporal and spatial parameters relating to the actuator have significant influence on the performance and characteristic behavior of the pump. Here we examine some of these parameters that are pertinent to our discussion.

2.3.4.1 The Effect of Excitation Frequency on the Flow Behavior

Experimental studies of the impedance pump have shown a nonlinear flow response to the frequency of actuation for pumps of various size scales [47, 30, 56]. The occurrence of flow peaks in response to the frequency of excitation and the presence of additional harmonic peaks in these studies indicate a resonance characteristic and signify the presence of wave behavior [30]. This resonance behavior is not surprising as the flow in an elastic tube propagates down the tube in the form of a wave and this wave can be partially reflected in the presence of obstacles [76]. The frequency at which the peaks in the flow occur can be predicted by a simple wave pulse model [31, 47] based on the speed of pressure wave propagation in the elastic tube, c, and the length of the tube, L, and is given by:

$$f_r = \frac{c}{2L}. \tag{2.1}$$

This resonant frequency corresponds to the frequency of actuation at which a newly generated pressure wave is in phase with the reflected wave from previous actuation that has doubly reflected at the ends of the tube and has traveled twice the length of the tube at a wave speed of c. The resonance behavior in this case is a consequence of the constructive interference of incoming waves and reflected waves from the ends of the elastic tube.

For the thin-walled elastic tubes that are the subject of the present work–with the wall thickness, h, much smaller than the tube diameter, d–the Moens-Korteweg wave speed of Equation (2.2), predicts the propagation velocity for a pressure disturbance in the tube with an elastic modulus of E, where the tube is filled with an incompressible fluid of density ρ:

$$c = \sqrt{\frac{Eh}{\rho d}}. \tag{2.2}$$

Equation (2.2) arises from solving the axisymmetric Navier-Stokes equation for a thin-walled linear elastic tube filled with an incompressible fluid and assumes amplitudes of the propagating pressure that are much smaller than the tube diameter and disturbance wavelengths that are much greater than the tube diameter [76].

2.3.4.2 The Effect of Excitation Location on the Flow Behavior

The dependence of the flow response to the location of excitation along the length of the tube signifies the importance of asymmetry in the system [29, 30, 47]. In the simple impedance pump described above, actuation at the midpoint of the elastic tube from its ends results in diminished flow. As the position of the actuator is moved away from the midpoint of the tube, the nonlinear behavior with distinct flow peaks described in Section 2.3.4.1 emerges. The flow behavior is found to be symmetric across this midpoint position, that is, changing the location of the actuator from one side of the midpoint to the other side leads to the reversal in the direction of generated flow [29, 47]. Increasing the asymmetry of the system by situating the actuator closer to the end of the tube and farther from the point of symmetry at the middle of the tube results in an increase in the generated mean flow [29, 47].

2.3.4.3 The Effect of Excitation Amplitude and Width on the Flow Behavior

It is intuitive that larger excitation amplitudes result in increased flow, as the volume of displaced fluid by the actuator increases. Studies of tubular impedance pumps suggest a linear relationship between the flow output and the volume of displaced fluid by the pincher. Furthermore, no appreciable change in the frequency of peak flow is observed when the amplitude of excitation is increased [47]. For similar reasons, an increase in the actuation width will yield higher flow rates.

2.3.5 The Effects of the Pumping Element Parameters on the Pump Performance

The pumping element is the fluid containing region of the pump, and depending on the pump configuration, can be a tube in tubular pumps or a membrane in a planar pump. Here we turn our attention to the tubular pump and its pertaining physical and geometric parameters that affect the pump performance.

2.3.5.1 The Effect of Tube Mechanical Properties on the Flow Behavior

Modulus of elasticity and compliance are two important parameters that can be used to characterize the mechanical properties of the pumping element. Increases in the elastic modulus of the system, results in increases in the wave speed, c, and upshift in the resonant frequency, f_r, as can be deduced from Equations (2.2) and (2.1). Compliance, defined as the rate of change of volume as a function of pressure and normalized by the resting volume, is another parameter that takes into account the elastic modulus as well as some geometric factors such as the tube diameter, length, and wall thickness. The importance of compliance of the pumping element in relation to that of the system's compliance is discussed in Section 2.3.6.4.

2.3.5.2 The Effect of Tube Geometric Properties on the Flow Behavior

Geometric parameters of the tube include the tube diameter, length, and wall thickness. The effects of change in the length or diameter of the pumping element on the performance of the pump can be easily discerned by referring to Equations (2.1) and (2.2). An increase in the diameter or the length of the pumping element will lead to a lower pressure wave speed and a downshift in the frequency of the peak flow.

Some behaviors observed in the case of the thin-walled tubes are not conserved for tubes with thicker walls. For example, the effect of transmural pressure which is discussed later in Section 2.3.6.3 is not observed for the thick-walled tubes. This discrepancy is attributed to the lower compliance of the thick-walled impedance pumps [47].

2.3.6 The Effects of the System Parameters on the Pump Performance

Systemic parameters external to the pump such as the physical properties of the fluid and the properties of the system that the pump is a part of also influence the pump performance. The following sections summarize some of these external factors and their relationship to the performance of the pump.

2.3.6.1 The Effect of Fluid Density and Viscosity on the Flow Behavior

Flow rate decreases with increasing viscosity and density of the working fluid. Increases in viscosity and density lead to higher frictional and inertial resistance of the system. Viewing the impedance pump as any black box pump generating differential pressure, this increase in the fluid resistance will reduce output flow. Furthermore, an increase in the density of the working fluid results in a decrease in the speed of pressure wave propagation, as can be seen in Equation (2.2); the lower wave speed leads to a downshift in the frequency of peak flow [47].

2.3.6.2 The Effect of Systemic Resistance on the Performance of the Pump

As expected, increasing the resistance of the system that the pump performs work on will lead to a decrease in the output flow. In the upper limit of infinite resistance obtained by the occlusion in the system, the pump generates no net flow [47].

2.3.6.3 The Effect of Transmural Pressure on the Performance of the Pump

In the case of the thin-walled impedance pump, an increase in the transmural pressure results in a shift in the frequency of peak flow to higher values. This behavior is attributed to an increase in the hoop stress and the tension of the tube wall, which leads to higher wave speeds and resonant frequencies [47]. This behavior is similar to the higher wave speeds encountered in a rope under higher tension.

2.3.6.4 The Effect of System Compliance on the Performance of the Pump

Difference between the compliance of the system and that of the pump is crucial for the independent performance of the pump. If the pump and the system on which it works on have similar compliances, the two will be coupled together and the pump response will be influenced by the system [47].

2.4 Biological Components for Tissue Engineering the Pump

Having a guiding design to construct the pump *in vitro*, the next objective in tissue engineering the muscular pumps described here was to identify suitable biological components for their construction. More specifically, the appropriate biological building blocks to take on the role of the actuator and the elastic body of the pump had to be determined.

Muscle cells were the obvious choice for the actuator of the pump as they are the natural contractile apparatus in living organisms. Neonatal rat ventricular cardiomyocytes, which were obtained from primary harvest for this purpose, were chosen as the actuator for the pump because of their easily achieved synchronous activity and relatively high frequencies and amplitudes of contraction when compared to other myocyte types such as skeletal and smooth muscle cells. Furthermore, cardiomyocytes are suited for extended durations of contraction as evidenced by the tireless beating of our hearts. We were additionally encouraged in our choice of actuator by previous demonstrations of the cardiomyocytes' ability to serve as actuators *in vitro* in the form of muscular thin films on elastic materials such as polydimethylsiloxane (PDMS) [19].

In selecting the tubular body of the pump, several criteria were applied. First, the tube had to be made out of biologically derived or biocompatible materials, as one of the main objectives of this study was to demonstrate the feasibility of manufacturing a biological machine solely out of biological components. For this reason, synthetic materials such as PDMS were eliminated from the pool of candidate materials. Second, the tubular substrate had to support the adhesion of the cardiac cells in order to integrate the actuator and the body of the pump. Third, the compliance of the tube had to be such that the stress generated by the cardiomyocytes was capable of deforming the fluid-filled tube. Additionally, it has also been shown that matching the elasticity of the substrate to that of native tissue can enhance the contractile properties of cardiac cells [18, 17]. Finally, we reasoned that for the biological pump to achieve optimal performance, the resonant frequency of the pump should be close to the natural beating frequency of the isolated cardiomyocytes actuating the pump.

From the survey of the candidate materials, small intestinal submucosa (SIS) met these criteria

[41]. SIS is a naturally occurring extracellular matrix derived from the small intestine of mammals that can be easily transformed into a thin acellular scaffold. It has the additional virtue of being similar in composition and elastic properties to that of native myocardial tissue [41, 58]. Predominantly comprised of collagen, the SIS scaffold contains a host of desired extracellular matrix cues such as growth factors and glycoproteins which promote cellular adhesion and integration [46]. The intrinsic tubular form of SIS was also attractive to us, as it eliminated the need to manufacture tubes out of protein-based biomaterials [63]. Furthermore, the relatively low porosity of the SIS tube allows for retention of fluid and transmural pressure by the pump [32]. Finally, our calculations of the resonant frequency based on the mechanical properties of SIS for a millimeter-scale pump yielded values on the same order of magnitude as the contraction frequencies of isolated cardiomyocytes.

The following chapter discusses the techniques that were used in order to obtain the biological components of the pump as well as the tools that were developed for their integration into a functional system. Also discussed are the techniques that were developed for the characterization of the tissue-engineered muscular pumps.

Chapter 3

Enabling Tools and Techniques

In this chapter, we turn our attention to the enabling tools and techniques that were used to tissue engineer, maintain, and characterize the cell-based pumps. Section 3.1 discusses in detail the methodology for obtaining the cells and the decellularized tissue which serve as the building blocks of the pump. Section 3.2 describes the design of a bioreactor that was constructed to maintain the tissue-engineered constructs. Sections 3.4, 3.5, and 3.6 relate to the characterization of the tissue-engineered pumps and cover the techniques used for data collection and their analysis.

3.1 Cell and Tissue Harvest

As discussed earlier, cardiac muscle cells were selected to serve as the actuators of the pump and the decellularized small intestinal submucosa was used as the tubular scaffold in tissue engineering the pumps. In obtaining the cardiac cells and the decellularized scaffolds, Sprague Dawley rats were used. Handling of the live animals, their euthanasia, and disposal were performed according to the guidelines set forth and protocols approved by Institutional Animal Care and Use Committee (IACUC) at the California Institute of Technology.

3.1.1 Primary Harvest of Cardiac Muscle Cells

Primary culture refers to a culture of cells started from cells, tissues, or organs that are taken directly from an organism [28]. Cardiac myocytes were isolated from three-days-old neonatal Sprague Dawley rats (Charles River Laboratories, Wilmington, MA, USA) using previously established primary

harvest techniques [19]. The choice of species and their age was motivated by the size of the available cardiac tissue as well as the extent of the maturity of the cells and the amount of the extracellular matrix present in the tissue. It was desired to obtain large quantities of differentiated cardiomyocytes while avoiding presence of a fully established extracellular network that makes the isolation of the cardiac cells difficult. The surgical procedures were conducted on a downdraft table using sterile tools. Further processing of the tissue was performed inside a biological safety cabinet and under aseptic conditions.

For each primary cell harvest, hearts from 10 neonates euthanized by decapitation were surgically removed by making an incision to the left side of the sternum through the ribcage of the animal down to the diaphragm. The ventricular tissue, approximately the lower 70% of the heart including the apex, was excised from each heart and used as the source for the cardiac cells. The ventricular tissue was maintained in ice-cold Hank's balanced salt solution (HBSS) and was periodically shaken to dilute the blood content from the excised tissue. Due to its high metabolic activity, the cardiac tissue is susceptible to ischemic injury after excision from the body as a consequence of lack of oxygen, depletion of cellular energy, cellular depolarization, breakdown of ion homeostasis, and eventual membrane rupture [69]. This hypothermic treatment of the isolated tissue is, therefore, crucial for preservation of the excised tissue through slowing down the rates of physical and chemical reactions that are detrimental to cellular function in absence of oxygen and by preventing irreversible damage to the cells [69]. After all hearts were removed, the ventricular tissues were minced by making several transverse and sagittal cuts per heart using a sterile razor.

The disaggregation of the isolated tissue was achieved using a combination of trypsin and collagenase enzymatic treatments. Trypsin helps dissociate cells from the extracellular matrix while the collagenase enzyme cleaves the peptide bonds of collagen present in the extracellular matrix of the myocardial tissue and facilitates the release of the cardiac cells. Since prolonged exposure of the cells to trypsin at elevated temperatures adversely affects cell viability, the cold trypsin technique was utilized [23]. The minced tissues were, therefore, transferred to a solution of 1 mg/mL of trypsin in HBSS (30 mL) and were incubated overnight at 4 °C while rotating on a laboratory shaker at

75 rpm.

The tissue treated with cold trypsin was subsequently subjected to multiple enzymatic digestions in a dissociation solution comprising of 1 mg/mL of collagenase in HBSS. Since collagenase activity is temperature dependant, the temperature of the tissue was raised by a washing step (4 min) using cell culture medium (25 mL) at 37 °C. The cell culture medium was comprised of media M199 supplemented with 10% heat-inactivated fetal bovine serum (FBS), 10 mM HEPES buffer, 0.1 mM MEM nonessential amino acids, 3.5 g/L glucose, 2 mg/L vitamin B-12, 2 mM L-Glutamine, and 50 U/mL penicillin. Additionally, the residual activity of trypsin was neutralized by the serum present in the cell culture medium during the washing step. The tissues were washed briefly with the collagenase solution (10 mL) to remove residual cell culture medium at a water bath held at 37 °C; the collagenase solution was aspirated and discarded without removing the tissue. The enzymatic digestions were then commenced. At each step, fresh collagenase solution (10 mL) was added to the remaining tissue which was rotated at 75 rpm in the 37 °C water bath for 2 minutes. The tissue explants were then gently pipetted up and down to disturb the tissue and to release the detached cells. The supernatant containing cells and some residual tissue was then transferred to ice-cold HBSS solution (4 mL) in 15 mL conical tube and were maintained on ice. The collagenase digestions were repeated for a total of 4 times, at which point most of the cardiac cells were removed, and only the connective tissue remained. The cell suspensions were then centrifuged for 5 minutes at 260 gcf (1200 rpm) and 4 °C in a refrigerated centrifuge equipped with a swing-bucket rotor to remove the collagenase solution. The supernatant from each conical tube was aspirated and discarded. The cell pellets were then suspended in ice-cold HBSS (6 mL per tube). The suspensions were subsequently filtered using a 40 µm cell strainer to remove the residual tissue and were pooled together into a 50 mL conical tube. The cell suspension was centrifuged for 5 minutes at 260 gcf and 4 °C. The supernatant was then removed and the cell pellet was suspended in warm cell culture medium (15 mL).

The resulting suspension was predominantly populated by cardiac myocytes and fibroblasts. Fibroblasts proliferate in culture at rates higher than the differentiation of cardiomyocyte progen-

itor cells present in the cell suspension. Overgrowth of fibroblasts generally leads to the eventual loss of the phenotypic characteristics of the native cardiac tissue such as its contractility [62]. In order to prevent this artifact, the higher adhesion properties of the fibroblasts were exploited to enhance myocyte population. Since fibroblasts are more adherent than cardiomyocytes, preplating the cell suspension in culture flasks and taking the supernatant yielded suspensions enriched with cardiomyocytes. The cell suspension was immediately used to seed the tubular scaffolds.

3.1.2 Harvest and Decellularization of Small Intestinal Submucosa

Female adult Sprague Dawley rats were used as donors for the source of small intestinal submucosa (SIS). SIS tubes were isolated following established protocols with slight modifications [41, 73]. The desired size of the tubular scaffold dictated the choice of species. Segments of rat proximal jejunum (∼5 cm long and ∼4 mm in diameter) were excised and washed in PBS. Mesenteric tissue was removed, taking care not to rupture the segments.

Gentle mechanical abrasion through repeated longitudinal wiping motion with a moistened gauze which was wrapped around a long tweezer was used to remove serosal and muscularis layers of each segment. The segments were then everted and mechanical abrasion with similar care was used to remove the superficial portions of tunica mucosa including the epithelium and lamina propria. What remained was a white, thin, translucent membranous tube which was predominantly made out of collagen.

The tubes were subsequently washed multiple times in PBS. To sterilized the tubes, they were washed in 70% ethanol. After sterilization, the tubes were treated under aseptic conditions, and the ethanol was removed by repeated washes in sterile PBS. For long term storage, the tubes were stored in 10% neomycin sulfate solution until ready for use.

3.2 Bioreactor Design

Bioreactors play an important role in successful tissue engineering of constructs *in vitro*. The main purpose of a bioreactor is to provide an *in vitro* environment that embodies the biochemical and physical signals that regulate development and maintenance of tissue *in vivo* [22]. Many bioreactors have been developed for engineering of cardiac and vascular tissues, providing perfusion of media as well as electrical and mechanical stimuli [37, 45, 68]. For the purposes of the present study, a bioreactor was designed to serve both as a testing platform to characterize the performance of the pumps as well as a suitable physiological environment to provide the constructs with the nutrients and physical stimuli needed for the growth of the tissue-engineered pumps.

3.2.1 General Design considerations

In keeping with the strict aseptic requirements of cell and tissue culture, when designing and constructing the bioreactor, the materials selected for its components were chosen such that they could be easily sterilized. With autoclaving being the most effective sterilization tool available to the researcher in the laboratory, the selected materials had to withstand repeated cycles of being subjected to high-pressure saturated steam at 121 °C for extended periods of 15–30 minutes. Furthermore, the selected materials had to be chemically inert and resistant to treatments with alcohols such as ethanol. Additionally, the materials that directly or indirectly through cell culture medium came into contact with the living cells had to be biocompatible, in the sense that they had to be chemically stable and not produce any byproducts that would be harmful to the viability or the function of the living cells.

Polycarbonate was selected for components that optical clarity was of importance. For structural rigidity and durability, acetal also known as Delrin was used. Silicone o-rings were used where sealing was required. Corrosion resistant stainless steel was utilized for the fasteners used in the bioreactor. Tubes used were pharmaceutical grade translucent platinum-cured slicone tubing. Other components used such as Luer-Lock connectors, Tuohy Borst adapters, or four-way stopcocks were either supplied sterile or were easily autoclavable.

Furthermore, the bioreactor was designed with future modifications in mind and can support addition of heaters, perfusion systems, and various forms of mechanical stimuli that were not utilized in this study.

3.2.2 Bioreactor Components

Figure 3.1 shows the major components of the bioreactor. The bioreactor consisted of a main chamber made out of acetal and measured 101.6 mm × 63.5 mm × 12.7 mm with an internal volume of ∼30 mL for the cell culture medium. Top and bottom visualization windows made out of optically clear polycarbonate were used to allow for transmitted illumination and visualization of the pumps and their generated flow under a stereomicroscope. The top and bottom faces of the bioreactor chamber included carefully designed rectangular grooves to accommodate circular silicone o-rings which made a liquid-tight seal at the top and bottom interfaces of the bioreactor chamber and the visualization windows. The visualization windows were each secured to the bioreactor chamber with the aid of 6 stainless steel fasteners which provided the required force to create the seal. Access to the tissue-engineered constructs required occasional breaking of this seal. To avoid spillage of the cell culture medium which could compromise the sterility of the bioreactor, the chamber was never filled with cell culture medium completely. The air gap between the liquid interface and the top visualization window posed a challenge during imaging of the constructs. As the temperature of the visualization window decreased in the course of image capture, the vapor present in the air gap condenses on the window, obscuring the view of the constructs. This problem was alleviated by altering the design of the top window as can be seen in Figure 3.1. An extrusion from the optically clear window submerges into the cell culture medium filled chamber and eliminates the air gap at the locations where visual access is important.

Access ports were incorporated into the design using Luer-Lock connectors which made a liquid-tight seal with the bioreactor chamber. Gas exchange was facilitated through a PTFE vent filter (EMD Millipore, Billerica, MA 01821, USA) connected to one of the access ports, as can be seen in Figure 3.2. Wire electrodes for electrical stimulation of the pump were introduced into the bioreactor

by using the access ports connected to Tuohy-Borst adapters (Merit Medical, South Jordan, UT 84095, USA). The remaining access ports allowed for changing of the media or could be utilized for monitoring of the chamber conditions in future designs. The bioreactor was maintained under standard cell culture conditions at 37 °C and 5% CO_2 inside a water jacketed incubator, eliminating the need to control the temperature and gas content of the bioreactor independently.

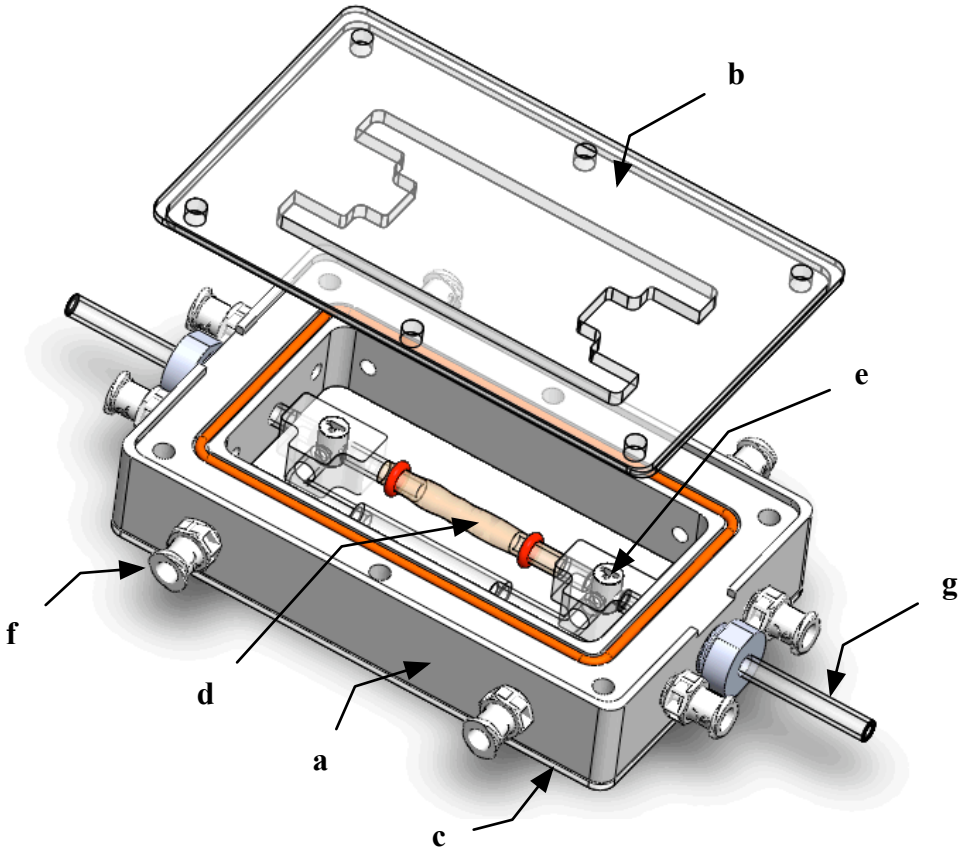

Figure 3.1. The bioreactor and its major components: bioreactor chamber (a), top and bottom visualization windows (b and c), a flow-loop (d) for flow characterization of the tissue-engineered pumps, custom-made three-way valves (e) for isolation of the flow-loop from the luminal ports (g), and ports for gas exchange, media change, and delivery of the electrical stimulation electrodes (f).

Also included in the design was a flow-loop that was used for flow characterization of the tissue-engineered pumps. The flow-loop consisted of two low-profile three-way valves connected to rigid glass tubing, as can be seen in Figure 3.6. Glass tubing was used for its optical clarity, providing visual access to the tracer particles that were used for flow characterization. Additionally, the smooth

fire-polished ends of the glass tubing facilitated the cannulation of the tubular scaffolds. Each end of the tubular scaffold was held fixed to the rigid glass tubes with the aid of two silicone o-rings. The bioreactor was also equipped with two luminal access ports for the priming of the system and introduction of the tracer particles into the flow-loop. The three-way valves were used to direct the flow when priming the system and isolated the flow-loop from the luminal access ports during characterization of the pumps.

The two L-shaped glass tubes of the flow-loop were connected with a short length of silicone tubing in order to accommodate possible variations in the lengths of the pumps. The connection between the glass tubes and the three-way valves was made by tapering the walls of the receiving holes of the valves. After sterilization, the flow-loop could be assembled with ease by this tapered connection. The body of the three-way valves were made out of polycarbonate as it is considered a relatively soft material. Harder materials such as acetal led to the fracture of the glass tubes.

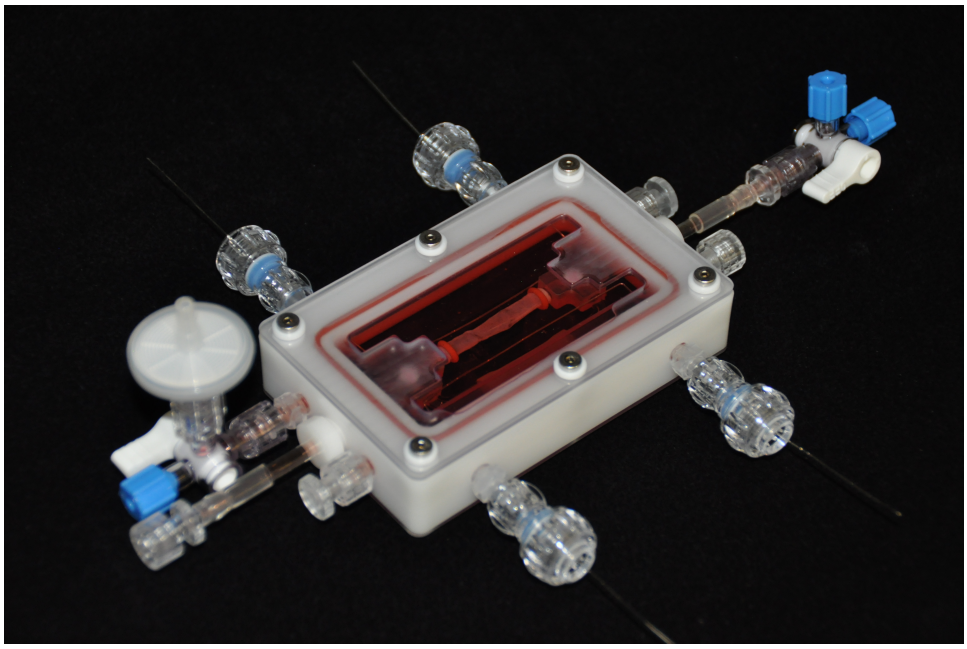

Figure 3.2. The assembled bioreactor with a tissue-engineered pump attached to the flow-loop. The platinum electrodes and the gas exchange vent can be seen in the image.

3.3 Integration of the Actuator and the Pump Body: Tissue Engineering the Pumps

Two types of muscular pumps were tissue engineered in the present study. One category, termed *fully seeded*, was a muscular pump which relied on the self-assembly of the harvested cardiac cells on the entirety of the scaffolding small intestinal submucosa. The other category, named *selectively seeded*, used directed self-assemply of the cardiac cells on the scaffold to engineer a muscular band actuator for the pump.

For the fully seeded pumps, the tubular SIS was cannulated on both ends to the glass tubes (OD = 4 mm, ID = ∼2.5 mm) of the flow-loop inside the bioreactor. The SIS tube was held fixed with the aid of two silicone O-rings (ID = ∼3.7 mm), as previously described. Cardiomyocytes (∼10^6 cells/mL) suspended in growth media (media M199 supplemented with 10% heat-inactivated FBS, 10 mM HEPES buffer, 0.1 mM MEM nonessential amino acids, 3.5 g/L glucose, 2 mg/L vitamin B-12, 2 mM L-Glutamine, and 50 U/mL penicillin) were seeded on the SIS substrate upon primary harvest.

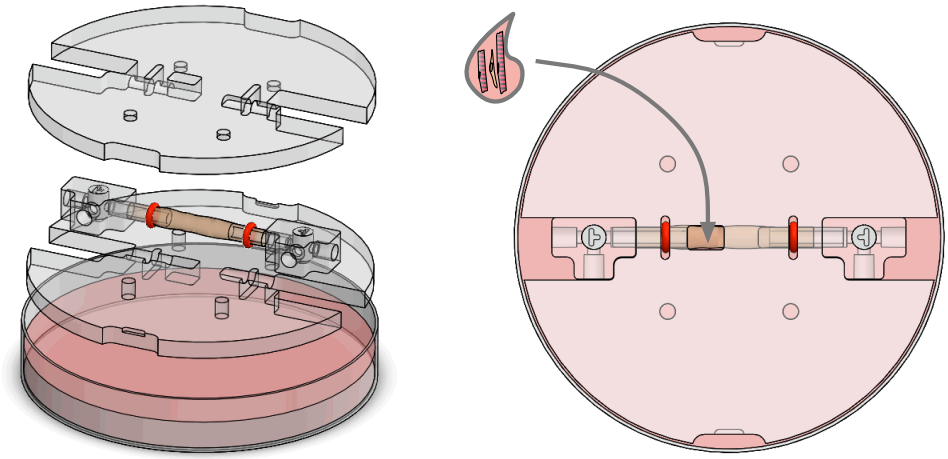

Figure 3.3. Selective seeding of cardiomyocytes to create muscular band actuators. The decellularized small intestinal submucosa from adult rats is cannulated on glass tubes and sandwiched between two polycarbonate masks with windows allowing for selective seeding of cardiomyocytes onto the tube (L = ∼20 mm). Ventricular cardiomyocytes suspended in cell culture medium are seeded on the unobstructed portion of the SIS tube upon primary harvest from three-days-old neonatal rats.

To selectively seed the cardiac cells into a predefined muscular band on the SIS tube, a physical masking process was used, as shown in Figure 3.3. The cannulated SIS was sandwiched between two polycarbonate masks that covered the length of the tube except for two coincident seeding windows positioned on both masks. The cells were delivered to the upper and lower sides of the tube through these seeding windows in two steps, which were 3 hours apart in order to allow for cell attachment before inverting the construct. The constructs were maintained in a cell culture dish until the unmasked portion of the tube exhibited spontaneous contractions, at which point, the cannulated SIS was transferred to the bioreactor.

3.4 Electrical Stimulation

Electrical stimulation was used in order to control the contraction frequency of the pumps' muscular actuators. Electrical stimulation was performed using field electrical stimulation which was delivered to the constructs by two U-shaped platinum wire electrodes (0.5 mm in diameter) that spanned the length of the constructs, as can be seen in the schematics of Figure 3.4 and the assembled bioreactor in Figure 3.2. The electrodes were separated from each other at a spacing of $\sim$13 mm. The electrodes exited the bioreactor through four Tuohy-Borst adapters as described in Section 3.2 which allowed for access to the electrodes without compromising the sterile conditions of the bioreactor chamber and the constructs.

Bipolar electrical pulses of 10, 15, or 20 V in amplitude, A, and 10 ms in duration, w, were generated using a Master-8 pulse generator (A.M.P.I. Jerusalem, Israel) which was connected to a Model BOP 50-4M bipolar operational power supply (Kepco, Inc. Flushing, NY 11352, USA). The stimulation frequencies were controlled by the temporal spacing of the electrical pulses, T. Seven physiologically relevant frequencies, ranging from 1 to 4 Hz in 0.5 Hz increments were used. A period of rest was maintained between each frequency of stimulation to allow for the recovery of the constructs to their normal spontaneous contractions.

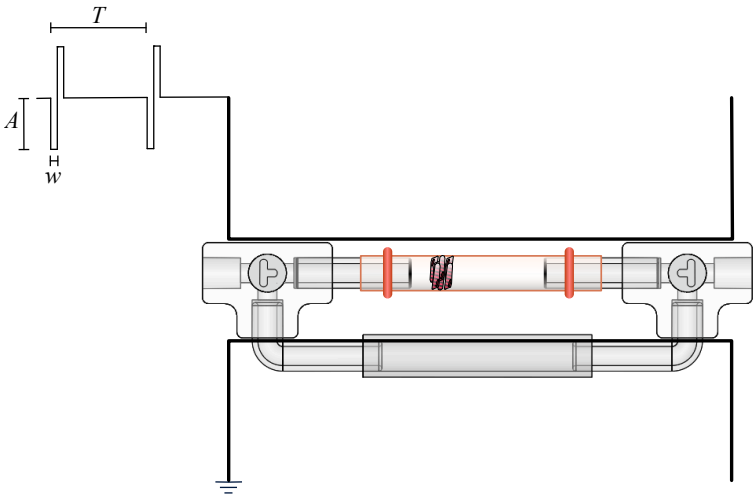

Figure 3.4. Schematic diagram for the electrical stimulation setup. Two parallel platinum wire electrodes span the length of the tube with each positioned on either side of the tissue-engineered pumps. One electrode is attached to a common ground and the other to a programmable pulse generator. Bipolar pulses were delivered to the cell culture medium filled chamber of the bioreactor to control the excitation frequency of the pump.

3.5 Imaging and Microscopy

3.5.1 Fluorescent Staining and Microscopy

Fluorescent staining was performed on the samples to visualize the cytoskeletal structure of the cardiac muscle cells seeded on the tubular small intestinal submucosa scaffold of the tissue-engineered pumps. The fluorescent stains also served as a verification method for selective seeding of the cardiac cells into muscular bands around the tube.

To visualize the Z lines of the sarcomeres in the cardiomtocytes, alpha-actinin was stained using an anti-alpha-actinin monoclonal antibody developed in mouse as the primary antibody [27]. As a secondary antibody, a goat anti-mouse IgG antibody conjugated to Alexa Fluor 594 was used. The secondary antibody was highly cross-absorbed against IgG from several species including rat IgG. This reduces the nonspecific binding of the secondary antibody to rat IgG present in the harvested cells instead of the mouse IgG from the primary antibody due to the close relation of the two species. This was of importance since the cardiac muscle cells in this study were derived from rats. To visualize actin filaments, phalloidin conjugated to either fluorescein or Alexa Fluor 488 was used. Hoechst stain was used to stain for the cell nuclei [34].

Rinsed tissue constructs comprising of the cardiac cells and the SIS tube were fixed in a 4% solution of paraformaldehyde (PFA) overnight at 4 °C. The fixed constructs were permeabilized in a 1% solution of Triton X-100 in phosphate buffered saline (PBS) for 15 minutes at room temperature. After permeabilization, the samples were rinsed 3 times using a wash buffer consisting of a solution of 1% Tween 20 in PBS. The cells were subsequently blocked to prevent nonspecific binding of the primary antibody for 45 minutes on a shaker at room temperature using a filtered blocking buffer consisting of 5% bovine serum albumin (BSA) and 1% Tween 20 in PBS.

The samples were then incubated at 4 °C on a shaker in a 1:200 dilution of the primary antibody in the blocking buffer. After incubation, the constructs were washed 3–4 times with the wash buffer for a duration of 5 minutes on a shaker at room temperature. Diluted secondary antibody in the blocking buffer (1:200) was used to fluorescently label the cells by incubating the constructs for an hour at room temperature on a shaker and were protected from light. The samples were washed 3–4 times as previously described. The cells were then stained for F-actin and their nuclei by appropriate dilutions of fluorescently labeled phaloidin (5 U/mL) and Hoechst (1 µg/mL) in PBS for 20 minutes at room temperature. The constructs were subsequently washed 3 times with PBS.

The samples were prepared for microscopy by carefully positioning the tubes along their axis on No. 2 glass cover slips, noting the axial and circumferential directions of the original tube. A Zeiss Axiovert Observer 10 (Carl Zeiss MicroImaging, Inc. Thornwood, NY 10594, USA) with the appropriate excitation and emission filters and equipped with 5×, 10×, and 20× objectives and an auxiliary 1.6× optovar magnification was used to visualize the constructs. Images were obtained using a Zeiss AxioCamMR3 camera and were processed to subtract the background fluorescence.

3.5.2 Image Capture and Stereomicroscope Setup

The tissue-engineered constructs had dimensions in the order of centimeters, while the particles used for flow visualization were in the order of microns. Such dichotomous magnification and field of view needs combined with the long focal length requirement imposed by the dimensions of the bioreactor motivated the use of a stereomicroscope for capturing images.

Imaging was performed on a Zeiss Discovery V20 stereomicroscope equipped with a 0.63× Achromat S objective lens. Images were captured using a MotionPro X3 CMOS camera (Integrated Design Tools, Inc., Tallahassee, FL 32301, USA) at a frame rate of 30 fps. Images were collected for a minimum of 20 S for each experimental data point. To synchronize the electrical stimulation and the recording of the images, the camera and the pulse generator were simultaneously triggered using one of the channels of the Master-8 pulse generator.

3.5.3 Calibration Curve

In order to relate the pixel size of captured images to physical unites, a calibration slide was imaged at various magnifications with a similar objective and camera as used for the rest of the experiments and a calibration curve was produced, as depicted in Figure 3.5.

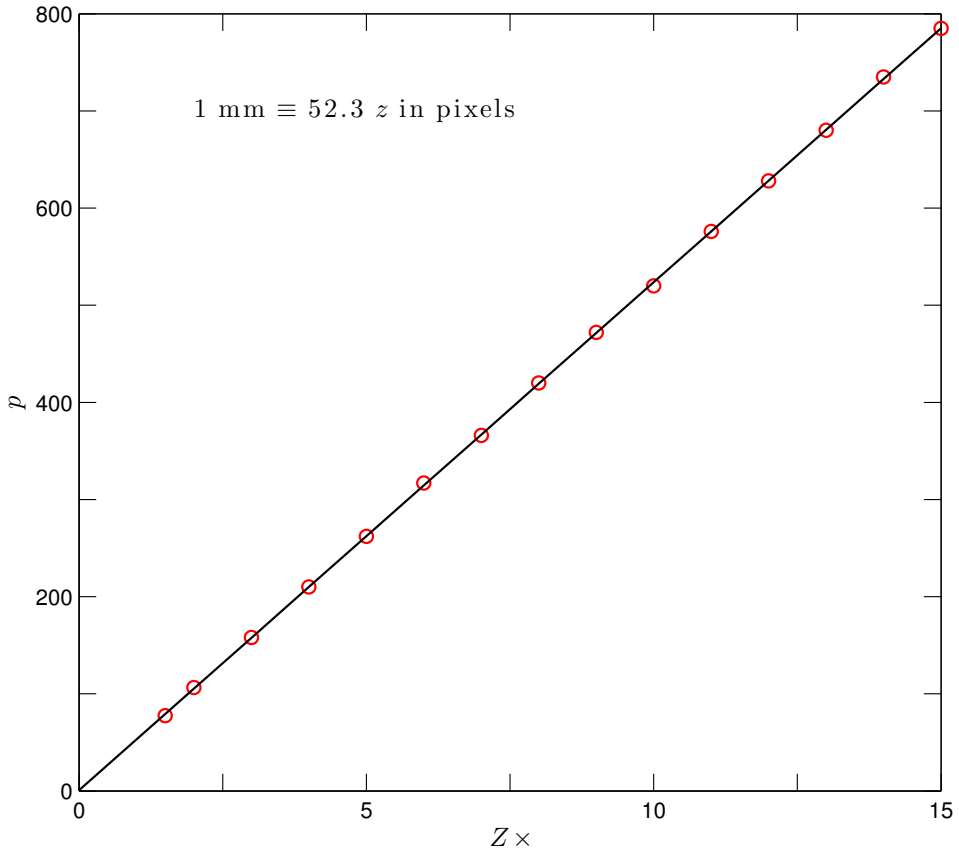

Figure 3.5. Stereomicroscope calibration curve. The fitted curve gives the number of pixels equivalent to 1 mm for a given zoom position of the pancrat, Z.

3.5.4 Flow Visualization

Particle tracking velocimetry (PTV) was utilized to characterize the flow. Polystyrene microspheres with 10 µm nominal diameter (Invitrogen, Carlsbad, CA 92008, USA) were used to seed the flow-loop as tracer particles. To maintain the sterility of the tissue-engineered constructs, the microspheres were sterilized by repeated two-hour heat cycles of 80 °C followed by twenty hours at 40 °C for a total of three cycles at 80 °C and two cycles at 40 °C.

The particles were suspended at a solid density of approximately 0.05% in a neutrally buoyant preparation of the cell culture medium to reduce the particles' sedimentation rate which would otherwise affect the flow measurements based on particle motion. The microspheres have a nominal density of 1.055 g/mL while the cell culture medium has a density of ∼1 g/mL. To raise the density of the cell culture medium, equal volumes of 2× cell culture medium and a 30% (W/V) sterile suspension of Ficoll 400 (GE Healthcare, Pittsburgh, PA 15264, USA) in ultrapure water were mixed, yielding a 1× cell culture medium supplemented with 15% (W/V) Ficoll 400. This preparation had a density close to that of the microspheres. This particle suspension was delivered to the flow-loop of the bioreactor with the aid of a 10 mL syringe through the luminal ports of the bioreactor.

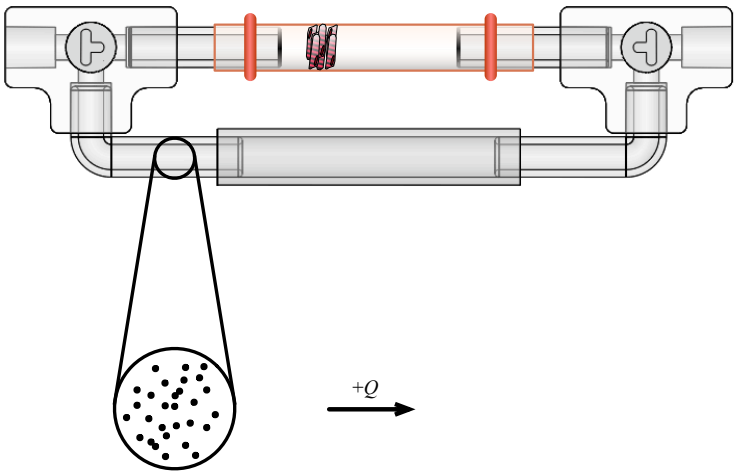

Figure 3.6. The flow-loop of the bioreactor which was used for flow characterization of the tissue-engineered pumps. Tracer particles with nominal diameter of 10 µm are used to seed the flow for visualization purposes. The positive direction for the flow is defined as the counterclockwise direction.

The particles were viewed through the clear glass tubes of the flow-loop using a pancrat zoom position of $Z = 10$ on the stereomicroscope. Images of the particles in the center plane of flow-loop were captured as previously described. A particle tracking program which will be discussed in Section 3.6.2 was used to analyze the digital images and to track the particles in order to deduce the flow behavior.

In the discussion that follow, the positive direction for the flow is defined as the counterclockwise direction which corresponds to the observed mean flow when the actuator is on the left side of the tube, as depicted in Figure 3.6.

3.6 Image Processing

An image, I, can be represented by a two-dimensional function $I(x, y)$, where x and y are the spatial coordinates, and the magnitude of I is the intensity of the image at a given coordinate. In the case of a digital image, the function I and its variables (x, y) take discrete values. For a digital image of M rows and N columns,

$$I(x,y) = \begin{bmatrix} I(1,1) & I(1,2) & \cdots & I(1,N) \\ I(2,1) & I(2,2) & \cdots & I(2,N) \\ \vdots & \vdots & & \vdots \\ I(M,1) & I(M,2) & \cdots & I(M,N) \end{bmatrix}.$$

Such representations of a digital image enable its mathematical manipulation to extract information from the image. In the present work, two classes of information were of interest. One related to the dynamics of the tube when actuated by the cardiac muscle cells, and the other concerned the tracking of particles that were used to visualize the flow. Digital processing of images was performed using programs implemented in MATLAB (Mathworks, Natik, MA 01760, USA) programming language and the associated Image Processing Toolbox.

Investigations of the tube dynamics involved the determination of the spatially and temporally

varying tube diameter and was performed by analyzing the digital images of the SIS tube using a custom edge detection program implemented in MATLAB that is discussed in detail in Section 3.6.1. Analysis of the tracer particles' positions was done using a particle tracking algorithm capable of accommodating complicated backgrounds and the accompanying code which was developed by Rogers et al. and will be briefly discussed in Section 3.6.2 [59].

3.6.1 Finding the Boundaries of the Moving Tube

The problem of finding the moving boundaries of the tube belongs to the family of image processing problems known as edge detection. To obtain the diameter of the tube along its length, one must determine the profile of the tube in its two-dimensional image representation.

An edge arises from intensity discontinuities in the digital image. The light originating from the microscope's light source travels through the chamber of the bioreactor that is filled with cell culture medium and encounters the tubular specimen. Having a lower transmittance than the background medium, the tube attenuates the amount of light reaching the camera. The attenuation of light manifests itself as a discontinuity in pixel intensity at the boundary of the tube and the background in the image. Such discontinuities in intensity can be detected by using the first and second order derivatives.

For the image I, the gradient of the pixel intensity with respect to the spatial coordinates,

$$\nabla I = \begin{bmatrix} \frac{\partial I}{\partial x} \\ \\ \frac{\partial I}{\partial y} \end{bmatrix}, \tag{3.1}$$

gives a measure of how rapidly the intensity changes. Generally, edges are detected by either comparison of the gradient with a threshold value determined by the user or by the peaks in the gradient, signifying a location of sudden change in intensity greater than the surrounding pixels [26]. Yet, such approaches are usually inadequate and lead to breaks and false edges if they ignore the characteristic properties of the features of interest to be detected.

The relatively horizontal orientation and simple geometry of a tube lends itself to some simpli-

fications. For such a tube, there are only two edges of interest: the upper and lower edges that delineate the tube from the background. Furthermore, the edges of interest lie horizontally and can be found by inspecting the changes in intensity along vertical lines.

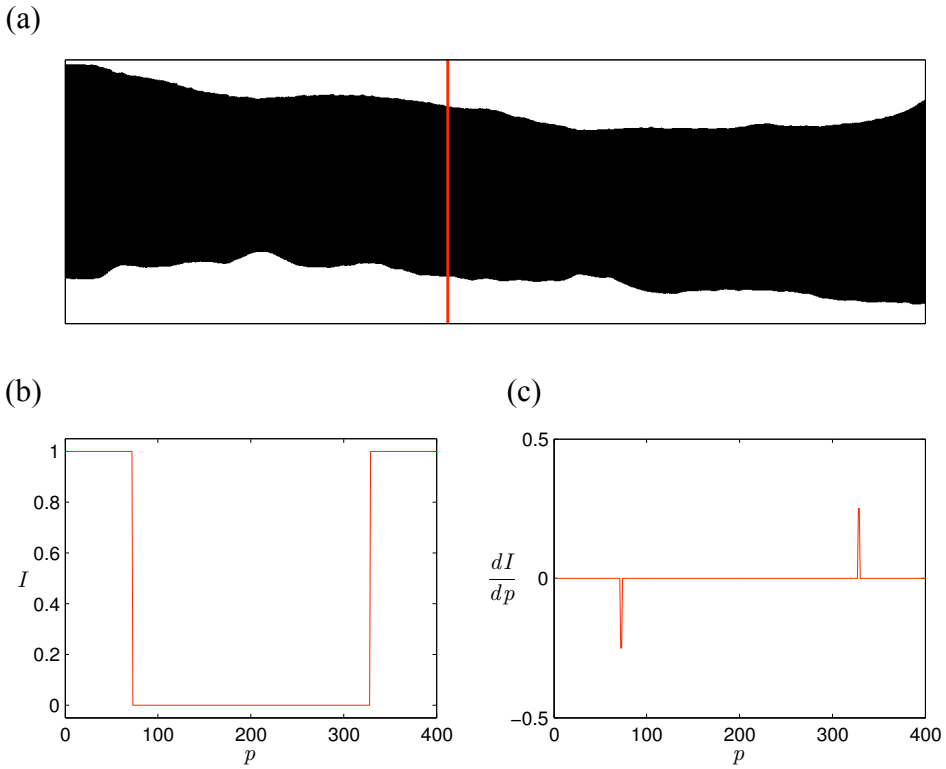

Figure 3.7. Edge detection for the ideal case of a binary representation of the tube. Panel (a) shows the binary image of a tube with an inspection line crossing the tube-background boundary. Panel (b) plots the pixel intensity along the inspection line. At the points where the inspection line cross the tube boundary, a sudden jump in pixel intensity can be observed. Panel (c) plots the magnitude of the intensity gradient in the direction of the inspection line. Minimum and maximum peaks in the gradient signify the intersection location of the inspection line and the tube boundary.

Figure 3.7 illustrates the underlying principle employed in finding the tube boundaries for the case of an ideal binary image where the tube is black, with intensity $I = 0$, and the background is white, with $I = 1$. A vertical inspection line selects a column vector in the matrix representation of the image intensity, as plotted against pixel position in Figure 3.7. As this inspection line scans the pixels, it travels the background of the image and crosses the tube, where the intensity drops suddenly to zero and remains at zero until the line crosses the tube boundary again. At this point the

intensity has another sudden jump to the background intensity, $I = 1$. These sudden discontinuities manifest as peaks in $\frac{\partial I}{\partial y}$, where the negative peak suggests the upper boundary of the tube and the positive peak represents the lower boundary of the tube. If this procedure is repeated for every column vector of image I, the location of all points where the vertical inspection line and the tube boundary intersect can be determined and the tube profile can be reconstructed.

Selecting the maximum and minimum peaks of the gradient, as in the approach described above for the ideal case of a binary image, picks the strongest edges encountered by each inspection line, and at times, leads to selection of false edges and jump discontinuities in the tube boundary, as depicted in Figure 3.8. False edges and jump discontinuities are generally due to the complexity of the actual tube and its background. These complexities include folds in the tube and aberrant particles in the background. Such jump discontinuities ought be corrected to obtain a correct representation of the tube profile. The approach taken here uses a combination of image enhancement techniques, threshold parameters, spatial filtering, local spatial comparisons, and temporal tracking to obtain a suitable result.

In the edge detection algorithm, images are read sequentially and are cropped to a region of interest determined by the user, which reduces the number of unnecessary operations to be performed. The images are preprocessed to enhance their contrast through intensity transformations. Several parameters are available to the user, including smoothing and contrast stretching parameters that allow adjustment of the images for better edge detection.

Initially, the gradients of each column vector of the image are taken as previously described and the points of maximum and minimum gradient are temporarily assumed to be points on the boundary of the tube at each column:

$$E_u(x,n) = \left\{ y_u \left| \frac{\partial I}{\partial y}\right|_{y=y_u} = \min\left(\frac{\partial I}{\partial y}\right) \right\}, \tag{3.2}$$

$$E_l(x,n) = \left\{ y_l \left| \frac{\partial I}{\partial y}\right|_{y=y_l} = \max\left(\frac{\partial I}{\partial y}\right) \right\}, \tag{3.3}$$

where E_u and E_l are the upper and lower edges, respectively, and n is the frame number.

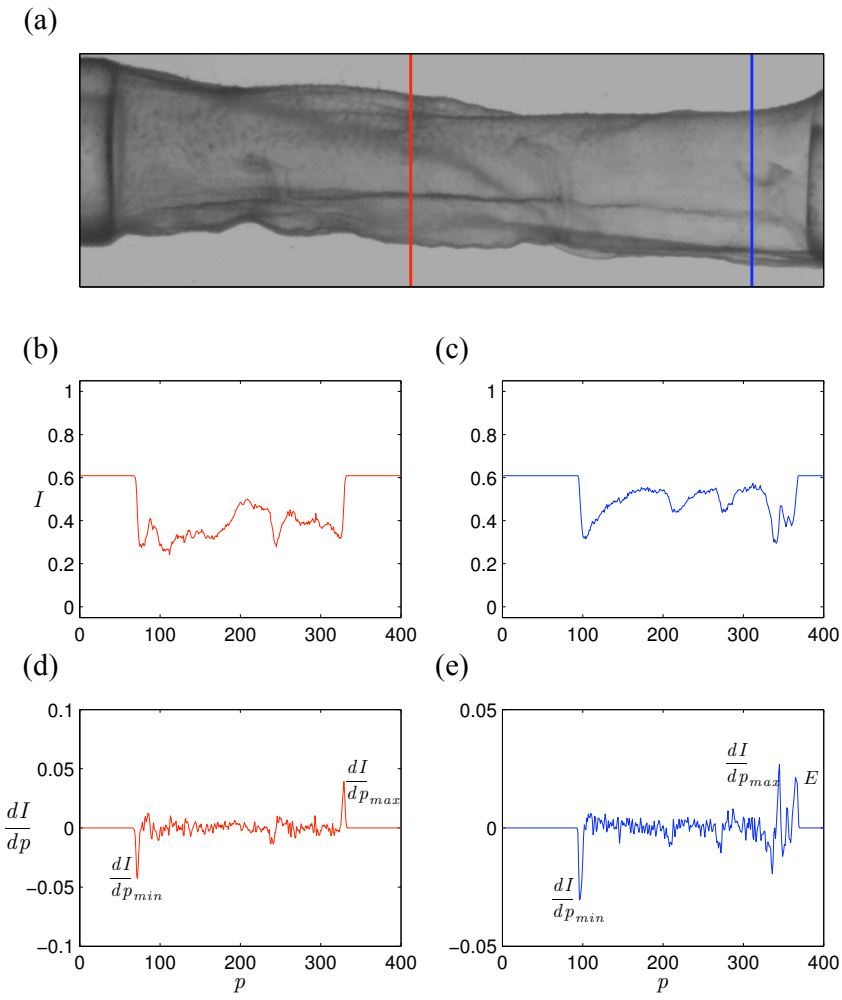

Figure 3.8. Edge detection for the case of a complex tube. Panel (a) depicts the image of a tube captured from one of the experiments, with two vertical inspection lines spanning the 400 pixel height of the image. Panels (b) and (c) are plots of pixel intensity at the left and right inspection lines, respectively. Panels (d) and (e) plot intensity gradient at the two inspection lines. For the left inspection line, the maximum and minimum gradients correctly pick the position of the edge, where for the right inspection line, the maximum gradient fails to correctly identify the tube boundary and picks a fold in the tube as a false edge.

As the tube is relatively horizontal and physically continuous, it is assumed that sudden variations in edge position between adjacent points that exceed a threshold parameter set by the user constitute a jump discontinuity due to false edge detection. The discontinuities for both upper and lower edges are discerned by the outcome of the relational expression

$$\left| \frac{\partial E_{u,l}}{\partial x} \right| > T_j, \tag{3.4}$$

where T_j is the threshold for jump discontinuity.

Generally, such regions of discrepancy are not isolated and result in more than one jump discontinuity in the tube's profile, as the detection routine alternates between the true and false edges. These edge discontinuities are closely spaced for each region and the algorithm combines the points of discrepancy with their nearest neighbors into $E^{\|}$ defined as

$$E^{\|} = E\left(x_{j:k}, n\right), \tag{3.5}$$

where $x_{j:k}$ is a region for which the edge discontinuity is identified. The program revisits these discontinuities to find the correct edge.

The algorithm resorts to the upper and lower edges from the previous frame, $n-1$, to correct for the jump discontinuities in the tube profile in the current frame, n. This is achieved by inspecting the average relative displacement of the edge in the neighborhood σ of the discontinuity between the two frames to obtain an approximation for the location of the edge in the current frame:

$$E_{u,l}\left(x_{j:k}, n\right) = E_{u,l}\left(x_{j:k}, n-1\right)\left(1 + \overline{\frac{E_{u,l}\left(x_{j-\sigma:j,k:k+\sigma}, n\right) - E_{u,l}\left(x_{j-\sigma:j,k:k+\sigma}, n-1\right)}{E_{u,l}\left(x_{j-\sigma:j,k:k+\sigma}, n-1\right)}}\right). \tag{3.6}$$

As can be expected, correct processing of the first image in the sequence is crucial due to the dependence of the algorithm on the location of the edge from the previous image where jump discontinuities arise in the detected boundary. Since there are no previous frames for the first image in the sequence, the algorithm replaces the regions of jump discontinuity by linearly interpolating

between the points immediately outside the jump discontinuity, which depending on the width of the region can be an acceptable or unacceptable representation of the profile. If the threshold parameters available to the user are not sufficient to correct points of discrepancy, the user is presented with an opportunity to mask the problematic regions through a graphics user interface (GUI). The GUI allows selection of multiple polygonal or elliptical regions in the background as well as in the tube. The mask regions are used to spatially filter the image to reduce the strength of the false edges identified by the user. At the location of the masks, the pixel intensity, $I(x, y)$, is replaced with, $I_m(x, y)$, by convolving the image with an averaging filter, w, where w is an $M \times M$ matrix [26]:

$$I_m(x,y) = \sum_{i=-a}^{a} \sum_{j=-b}^{b} w(i,j) I(x-i, y-j), \tag{3.7}$$

$$w(i,j) = \frac{1}{M^2}. \tag{3.8}$$

3.6.2 Particle Tracking Velocimetry

Tracking of the tracer particles was done according to the tracking routine developed by Rogers et al. and is briefly described here [59]. The particle tracking algorithm first reduces the image noise due to discretization by convolving the image with a Gaussian function, yielding a smoothed image with pixel intensities set to the weighted average of the neighboring pixels [14]. The particles to be tracked are then identified by the presence of local extrema in intensity with an initial estimate of the particle position at (x_0, y_0). The mean of the distance between each extremum point and its adjacent points of inflection along the orthogonal lines is used to discern an initial estimate for the radius of each particle, R. After this initial estimation of particle coordinates and radii, subpixel refinement of the particle position (x_i, y_i) is performed by an iterative process of fitting the local image intensity of the particle to a quadratic polynomial function in a domain $x_i - 2R \leq x \leq x_i + 2R$ and $y_i - 2R \leq y \leq y_i + 2R$ and finding the extremum of the fitted quadratic part. The iterations end when the change in the coordinates are less than a prescribed sub-pixel threshold.

For each particle, its eccentricity, rotation, radius, average brightness, and skewness is calculated based on the intensity map and the constants of the polynomial fit, and each parameter can be used

for thresholding and particle discrimination. Lastly, the particle tracking routine links the particle positions between the frames. This is done by first assuming that the particles do not move more than their radius in two consecutive frames, and therefore, the position of a particle in frame n provides a good initial estimate for its position in frame $n + 1$. If this assumption does not hold for a particle, the program searches for a nearby extremum in intensity that is similar in brightness to the original particle and is closer than the next-nearest identified particle.

The output from the particle tracking program includes the position of each tracked particle and their respective frame number. The time between the captured frames can be used along with particle positions to obtain instantaneous and mean particle velocities.

Chapter 4

Characterization of the Tissue-Engineered Pumps

As with any physical system, the process of characterizing and testing of the tissue-engineered construct should be done with care as to not damage the system or influence its function. This is even more crucial for a biological machine which is relatively fragile compared to its mechanical counterparts. In addition to the general practices, care must also be taken to keep the constructs contamination free by observing aseptic conditions. In this chapter, we discuss the characteristics of the tissue-engineered impedance pumps. Section 4.1 takes a look at the types of data collected and their initial processing to extract quantitative information about the function of the pumps. Section 4.2 is concerned with the general observations on the growth and spontaneous behavior of the tissue-engineered constructs. Sections 4.3 and 4.4 explore the tube dynamics and flow response to frequency of actuation for the fully seeded and partially seeded tissue-engineered pumps.

4.1 Raw Data and Preliminary Data Processing

The majority of the data collected from the tissue-engineered pumps were in the form of digital images, which offered a noninvasive method of monitoring the pump function. With the aid of digital image processing algorithms discussed in Section 3.6, these images were transformed into quantitative data that allowed for further understanding of the pump behavior.

The collected data fall into two distinct categories: images of the beating pump which enabled

the characterization of the tubular pump's dynamics and images of the tracer particles that allowed for flow visualization and quantification. Figures 4.1 and 4.2 are representative images of these two data categories after initial processing.

Figure 4.1 shows the pump body at two time points with the upper and lower boundaries of the pump profiled using the algorithm developed in Section 3.6.1. As is evident from the image, the developed image processing program is successful in correctly detecting the time-varying tube profile. From the relative location of the upper and lower boundaries of the tubular constructs, tube diameter was extracted as a function of time and position along the length of the tube. This diameter representation of the tube dynamics is the basis for the further analysis performed in the following sections.

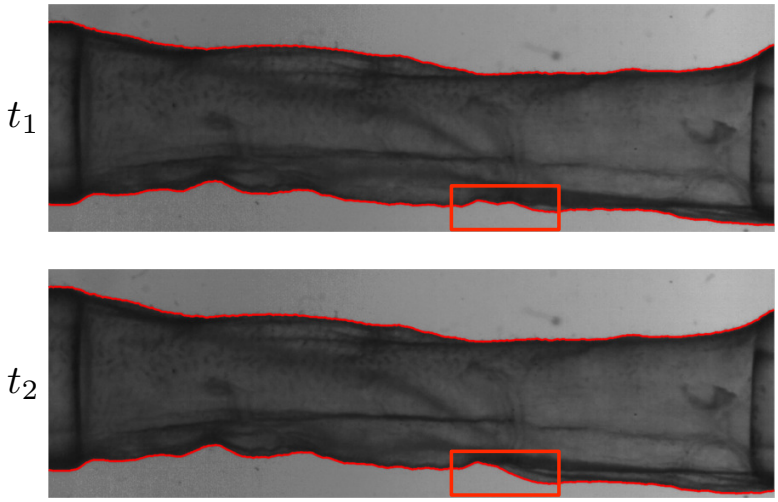

Figure 4.1. Representative images of the tubular pump at two time points. The red lines clearly trace the upper and lower boundaries of the tube at each time point. The rectangular region depicts a location along the tube for which the tube profile has distinctly changed between the two time points.

It should be noted that the diameter representation of the pump body as described above is only a partial representation as it does not contain the information from all three spatial coordinates. This representation does not fully capture the complex dynamics of the tubular body of the pump. Furthermore, as with any measurement, errors inevitably arise in the course of finding the tube profile. Appendix A discusses the sources and relative magnitudes of such errors and the steps taken to increase the reliability of the data through spatial and temporal averaging.

Figure 4.2 shows images of the tracer particles used for flow visualization at two time points. The circles at time point t_1 represent particles that were tracked by the particle tracking software for the duration of captured data. The arrows in the image of the time point t_2 represent the distance traveled by the particles for the duration $\Delta t = t_2 - t_1$. Average and instantaneous velocities and mean volumetric flow rates can be deduced from this data, as is discussed further in Sections 4.3 and 4.4.

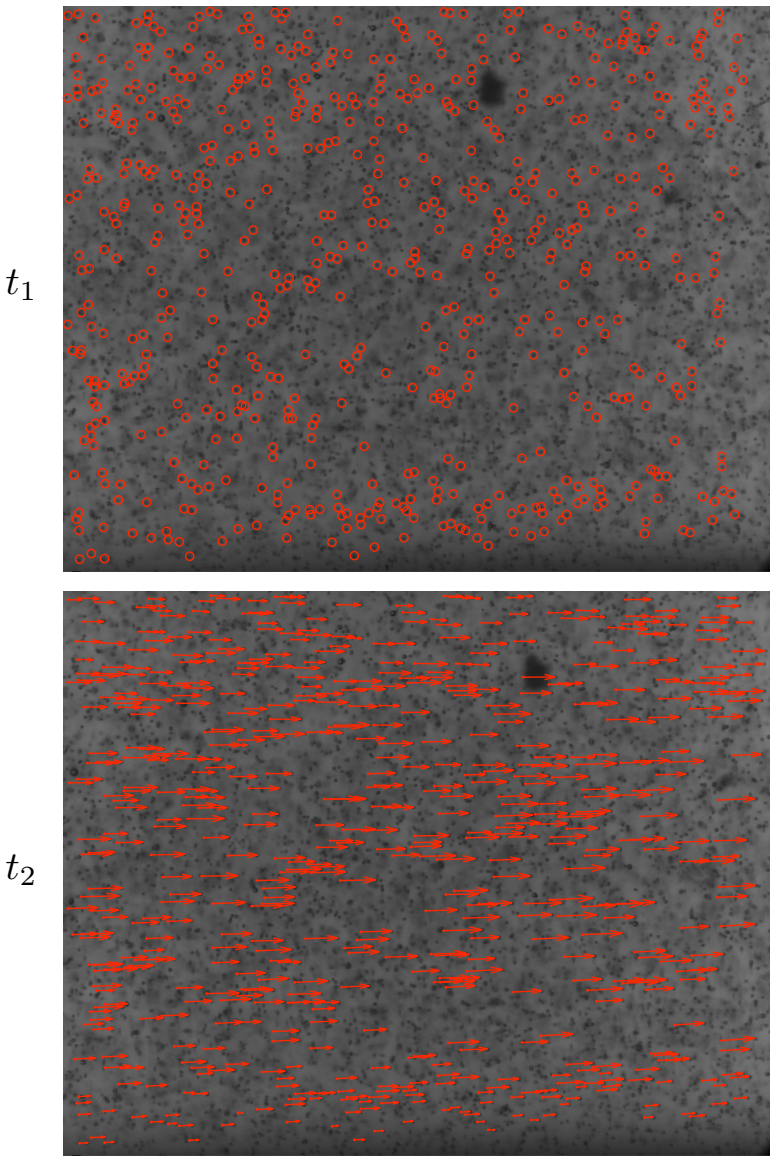

Figure 4.2. Representative images of the tracer particles tracked at two time points. The arrows signify the distance traveled by the particles in the duration of data collection and can be thought of as average velocity vectors.

4.2 Emergence of Contractile Patterns in the Tissue-Engineered Constructs

One of the first steps in tissue engineering the pumps was to investigate that the harvested cardiac muscle cells were capable of integrating with and actuating the tubular scaffold of the pump body. To this end, decellularized tubular SIS scaffolds were cannulated at both ends to the glass tubes of the bioreactor and seeded in their entirety with harvested neonatal rat ventricular cardiomyocytes, as described in Section 3.3. The constructs were maintained in the bioreactor under the standard cell culture conditions and by periodical changes of cell culture medium.

The constructs were monitored periodically for signs of animation due to the spontaneous contractions of the cardiac muscle cells. When cultured on tissue culture plastic, one can generally observe spontaneous contractions of individual cardiomyocytes within 24 hours of plating. In the case of the tissue-engineered constructs, global spontaneous contractions of the fluid filled tubes were observed within 48 hours post seeding. These contractions generally grew stronger for a period up to a week, at which point the SIS tube spontaneously transitioned from a fully open state (diastole) to a partially constricted state (systole). Spontaneous frequencies of contraction were variable during this period, but upper frequencies of $\sim$3 Hz were observed. The contraction ratio of the tube which is defined as the percent fraction of the difference between diastolic and systolic diameters to the diastolic diameter was also variable, with an upper value of $\sim$12% recorded for one construct.

Figures 4.3–4.6 represent one such construct which was tissue engineered according to the discussion above. The construct was monitored for a period of four days starting from the third day after seeding. Figure 4.3 depicts the superposition of the time varying tube profiles as obtained from the images of the tube. In other words, each panel of Figure 4.3 is akin to a long exposure image of the construct which captures several contractions of the tube. The thickness of the lines tracing the tube profile is a visual representation of the relative magnitude of wall motion compared to the diameter of the tube.

Another phenomena that is captured in the plots of Figure 4.3 is the continuous traction forces

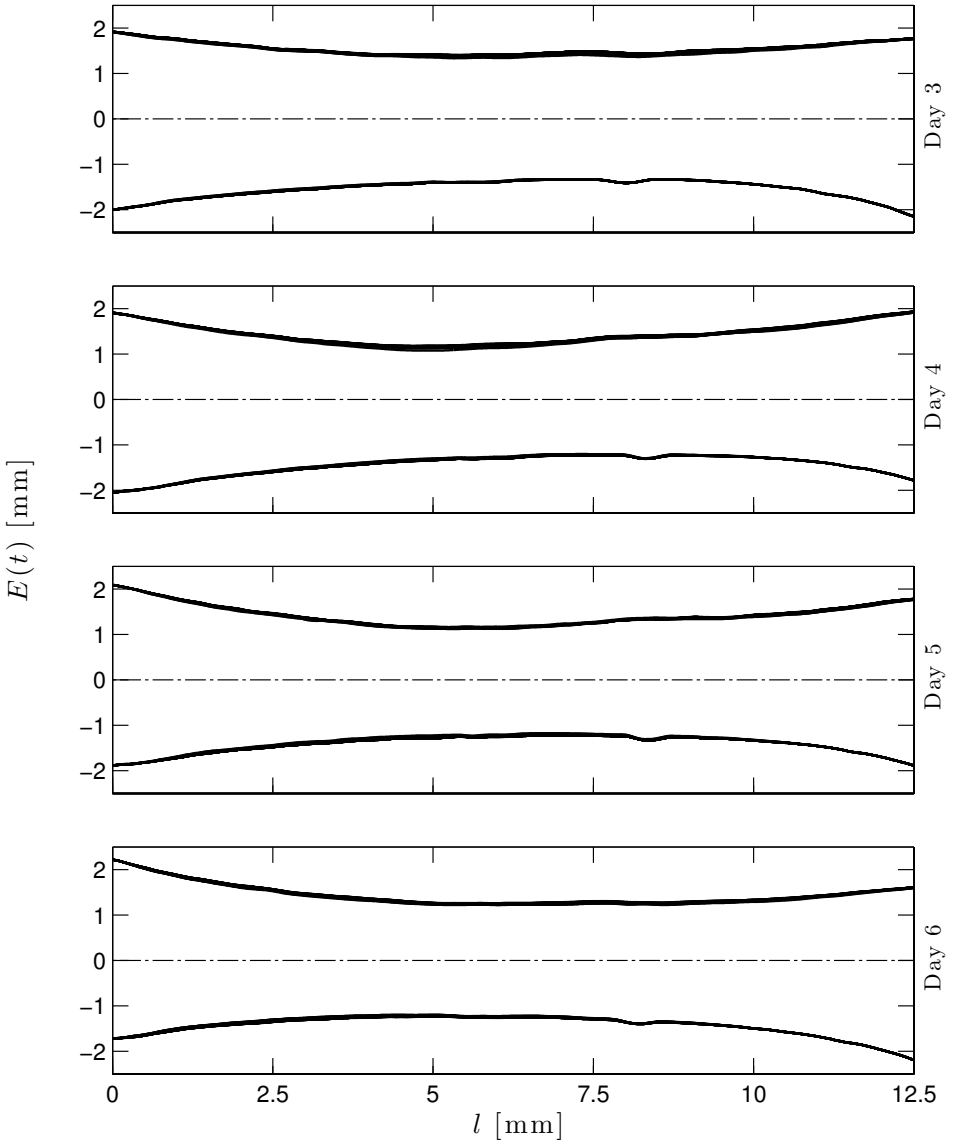

Figure 4.3. A tissue-engineered construct monitored for four consecutive days. Superposition of the tube profile for a period of 20 seconds captures several contractions of the tube. The thickness of the lines delineating the tube boundaries indicates the largest magnitude of contraction at each point through the length of the tube and can be compared relative to the tube diameter.

exerted on the tubular substrate by the cells. A close comparison between days 3, 4, and 5 reveals that the mean diameter at the midpoint of the tube has decreased with time. Living cells are known to exert mechanical forces on their substrates [33]. In fact in the absence of an opposing force, for instance the transmural pressure in the flow-loop of the bioreactor or the rigid boundary conditions imposed by the glass tubes at the ends of the tissue-engineered constructs, these traction forces can lead to the closure of the tube lumen. This further signifies the importance of the bioreactor in the proper growth of the tissue-engineered constructs in addition to providing a physiologically suitable environment.

Figure 4.4 shows the maximum deviation from mean diameter for the tubes of Figure 4.3. The mean diameter, $\overline{d}$, is calculated in a temporal sense,

$$\overline{d} = \overline{d}(l) = \frac{\sum_{i=0}^{n} d(t_i, l)}{n},$$

that is, $\overline{d}$ is variable along the longitudinal axis of the tube, l.

The dashed lines in Figure 4.4 mark the mean diameter of the tube, $\overline{d}$, and the red (light) and blue (dark) lines mark the position of two points separated from one another along the length of the tube. These points are investigated in more detail in Figures 4.5 and 4.6. It should be noted that the mean diameter $\overline{d}$ is affected by the frequency of contraction. As the frequency of contraction increases, the tube spends more time points in the contracted state which has a smaller diameter. This in turn, reduces the value of mean diameter.

Another observation that can be made by consulting Figure 4.4 is the effect of the fixed boundary condition at the ends of the tubular construct. Deviation from the mean diameter approaches zero at the ends of the tube, as would be expected from the boundary conditions imposed by the rigid glass tubes that the SIS scaffold is cannulated to.

Figures 4.5 and 4.6 clearly capture the contractile behavior of the tissue-engineered constructs over time as the cells rearrange on the scaffolding extracellular matrix and make mechanical and electrical connections with one another. Figure 4.5 shows the temporal behavior of the tube diameter

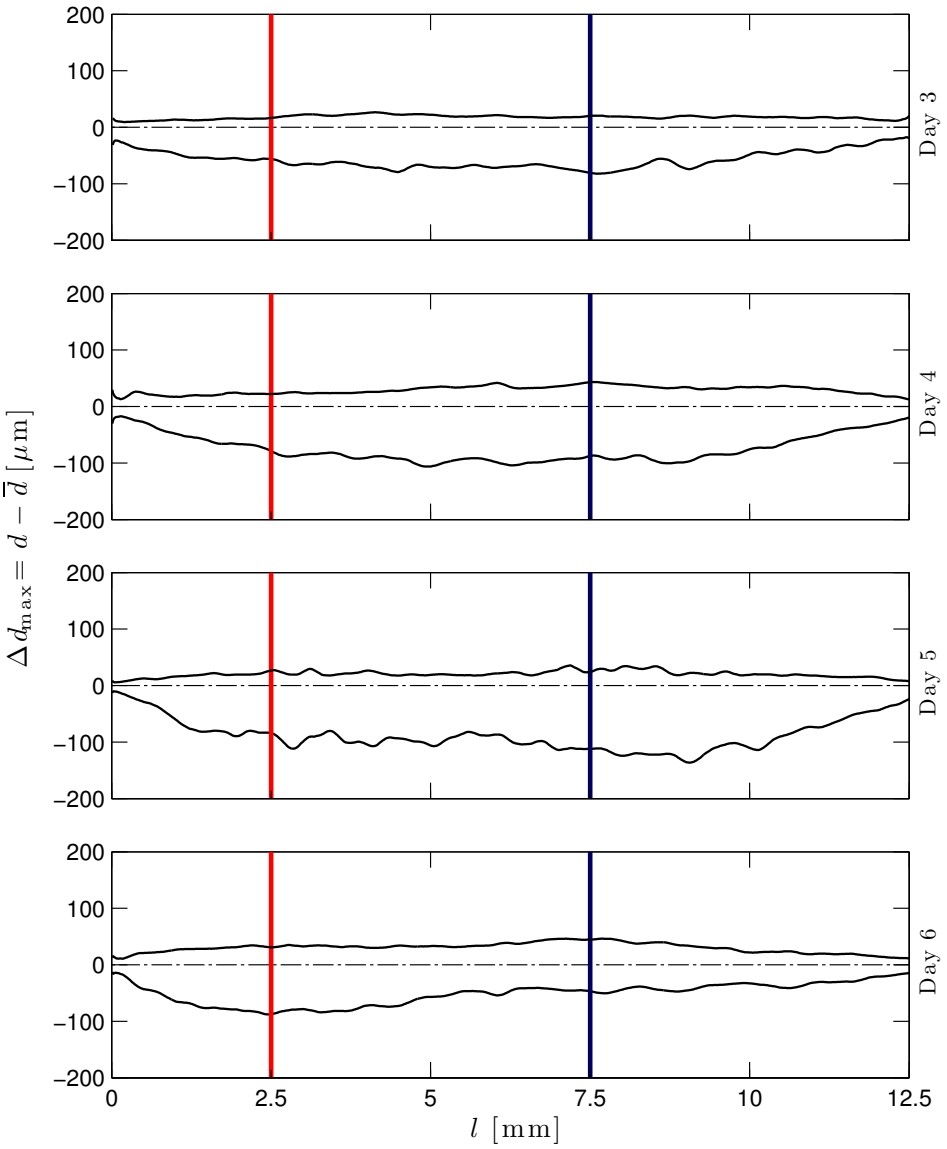

Figure 4.4. Maximum deviation from mean diameter, $\overline{d}$, reached along the longitudinal axis of the tube in the duration of data collection. The dashed lines mark the mean diameter. The red (light) and blue (dark) lines mark the position of two points along the length of the tube that are inspected in more detail.

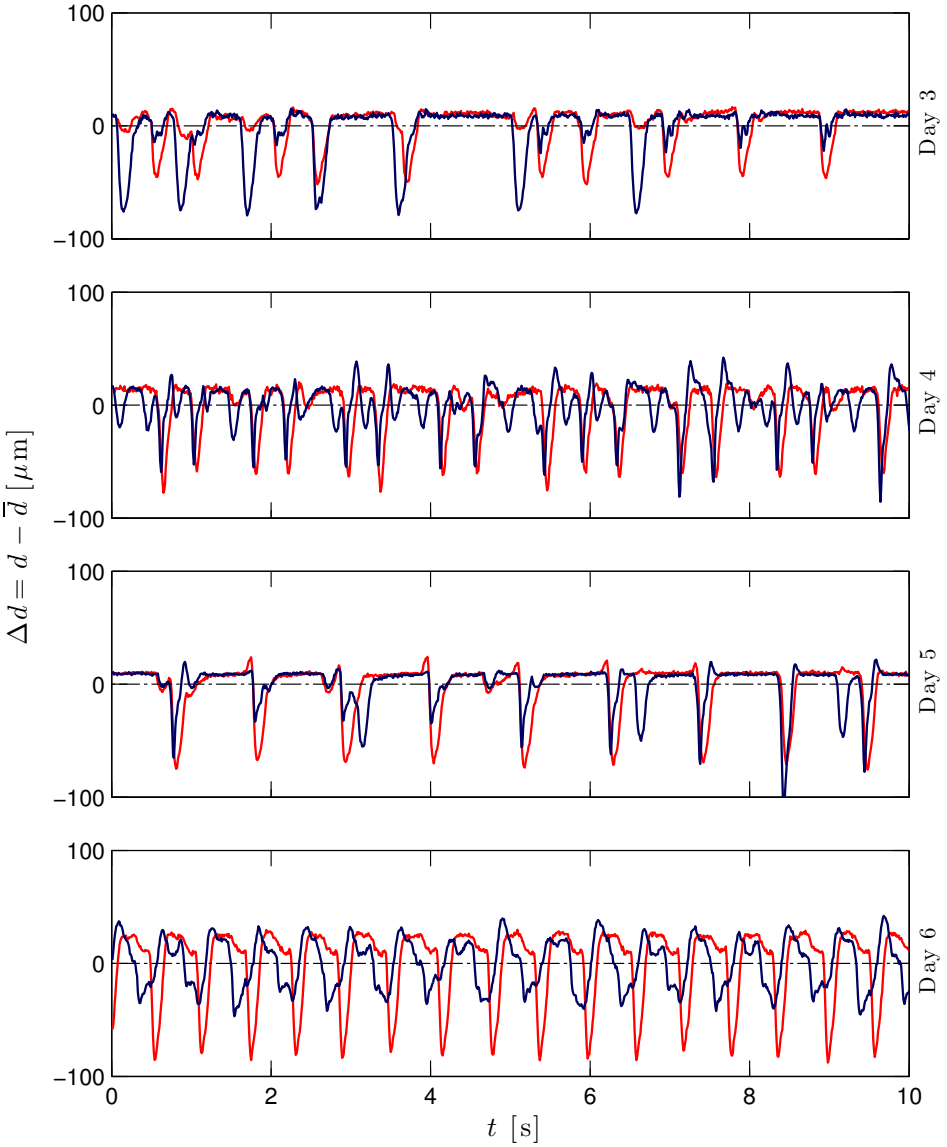

Figure 4.5. Temporal profile of the tube's spontaneous contractions. The red (light) and blue (dark) curves correspond to the points marked in Figure 4.4.

at the two points marked by the red (light) and blue (dark) lines in Figure 4.4, and the plots of Figure 4.6 depict the corresponding spectral analysis which was obtained by applying fast Fourier transform (FFT) to the time varying diameter of the tube.

As can be seen from the plots of day 3 in the time and frequency domains, no clear amplitude or frequency of contraction has been established. No dominant peak can be observed in the spectral analysis for either of the two points as the contractions are sporadic and irregular. This lack of regularity is also observable in terms of amplitudes of contraction, with neither of the two inspected points showing a persistent dominance in their strength of contraction over the other.

Over time, a pattern emerges in the contractile behavior of the spontaneously beating tube. The amplitudes of contraction become more regular and the contractions towards one end of the tube become the dominant ones. Furthermore, the contractions become periodic as can be observed from the spectral analyses of Figure 4.6. Additionally, the inspected points which are separated from one another by a distance of 5 mm exhibit synchronous activity, although their contraction profile is different.

Several factors can contribute to the synchronous activity along the length of the tube. Cardiac myocytes in culture are known to make gap junction connections which contain large, nonselective ion channels that allow electrical communication among adjacent cells by passive diffusion of ions and other small molecules between cytosol of adjoining cells [38]. Cardiac fibroblasts have also been shown to contribute to the coupling of cardiac electrical activity by making similar gap junction connection, although these connection suffer from long delays in impulse propagation [24]. Another contributing factor could be stretch activation of cardiomyocytes [64, 12]. Stretch activation is an intrinsic length-sensing mechanism in cardiac muscle and is believed to operate by cooperative recruitment of weakly bound nonforce-generating cross-bridges into strong-binding force-generating states and leads to a delayed generation of force [65]. As the tubular scaffold is actuated at one location, the mechanical disturbance can travel through the tube and can activate the contraction of the distant cardiomycytes. Both mechanisms discussed could possibly explain the apparent delay seen in the contraction profile of the investigated points in Figure 4.5 on day 6.

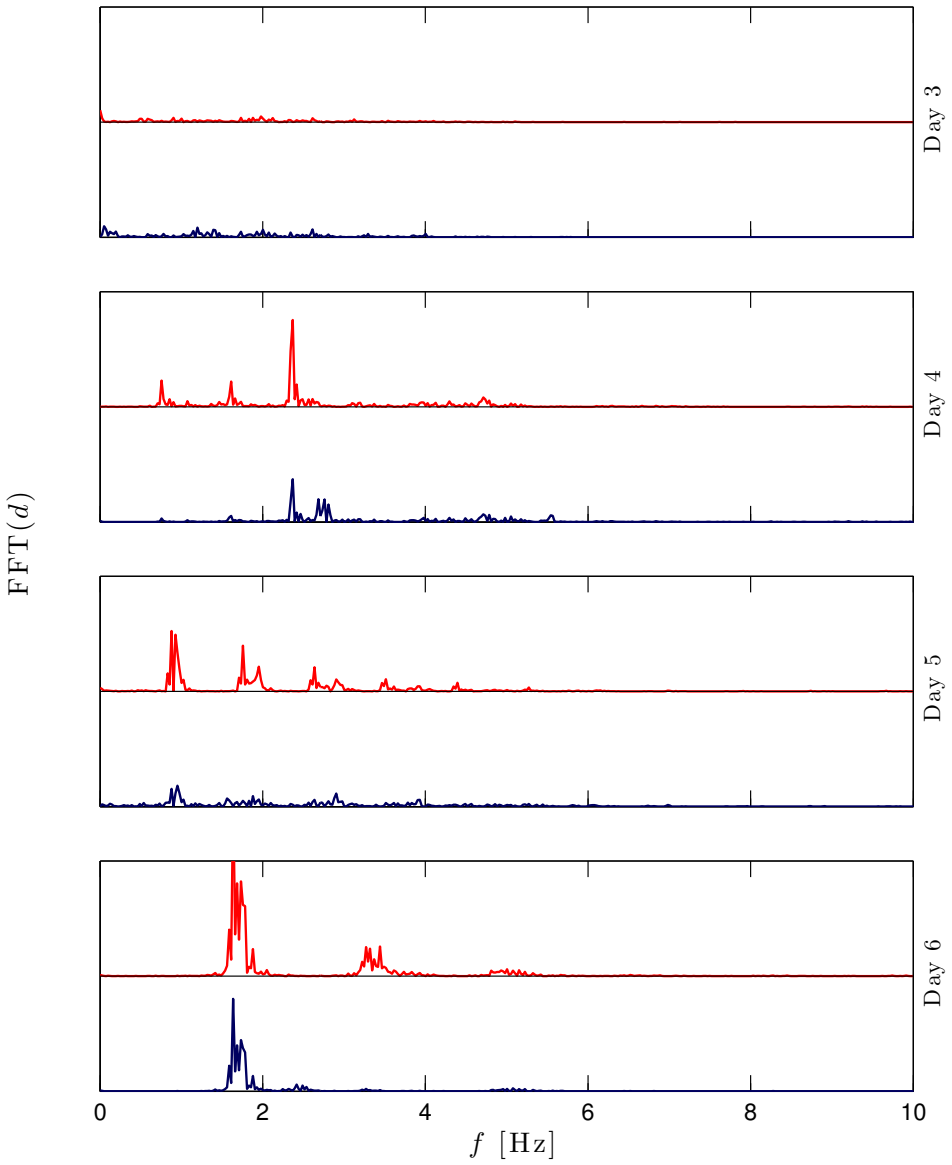

Figure 4.6. Amplitude of fast Fourier transform (FFT) analysis of the tube diameter for the spontaneously contracting construct. The red (light) and blue (dark) curves correspond to the similarly identified curves in Figure 4.5. The plots are made on the same scale.

The preceding discussions summarize general observations that were made on the spontaneously contracting constructs that are presented here. Variations exist in the amplitudes and frequencies of contractions among each construct as well as the length of time required for the discussed patterns to emerge, but the general behavior is conserved. Also notable is the oscillatory flow generated by the constructs. In essence, the tissue-engineered constructs are primitive hearts with a function similar to the valveless embryonic heart of vertebrates. The flow characteristics and the tube dynamics of these cell-based pumps will be discussed in greater detail in the following sections.

4.3 Frequency Response Characterization of a Fully Seeded Tissue-Engineered Pump

As discussed earlier in Section 2.3, one of the characteristics of the valveless impedance pump is its nonlinear flow response to the excitation frequency. This served as a motivation to explore and characterize the flow response of the tissue-engineered pumps by altering their excitation frequency.

The beating frequency of the actuating cardiomyocytes can be controlled by both chemical or electrical means [27, 19]. Addition of different concentrations of chronotropic agents such as epinephrine to the cell culture medium can be used to alter the contractile frequency of the pump. Electrical field stimulation was the favored method, though, as it could be precisely controlled. Under electrical field stimulation, both the duration and number of forced contractions could be easily controlled by adjusting the same parameters in the electrical signals that are delivered to the tissue-engineered constructs. Furthermore, the removal of the stimulating agent was immediate under electrical stimulation as opposed to chemical stimulation.

As briefly mentioned at the end of the previous section, it was observed that the fully seeded and spontaneously contracting tissue constructs generated flow. To investigate the observed contraction induced flow and the effects of contraction frequency, electrical stimulations with different frequencies were delivered to the pumps using two platinum electrodes according to the previous discussion in Section 3.4. Seven frequencies of stimulation, ranging from 1 to 4 Hz, were explored and the results

are presented and discussed in the following sections.

4.3.1 Tube Dynamics under Forced Electrical Stimulation

In order to gain insight into the dynamics of the muscular pumps, contraction ratio, CR, defined as

$$CR = -\frac{d(t,l) - d_0(l)}{d_0}, \tag{4.1}$$

was used to quantify the relative changes in tube diameter in response to the contractions of the actuating cardiac muscle cells. The nonuniformity of the scaffolding tube's diameter along its length necessitates the identification of a relevant characteristic diameter, $d_0(l)$, for normalization purposes, where d_0 is also variable along the longitudinal axis of the tube. Ideally, this characteristic diameter would be the resting diameter of the tube. Yet it is difficult to identify this rest state for a contracting tube. Mean diameter, $\overline{d}(l)$ is another possible parameter that can be used for calculations of contraction ratio, but as previously discussed, $\overline{d}$ is affected by frequency of contractions and introduces bias in the calculations at higher frequencies. Furthermore, use of mean diameter would lead to negative values for some of the time points through the contraction cycle. Therefore, the maximum value of diameter reached during the contraction cycle at each point along the length of the tube is used as the characteristic diameter in CR calculations.

Plots in Figure 4.7 represent the ensemble of contraction ratios along the length of the pump for each of the stimulation frequencies that were investigated. To obtain an average contraction profile for each frequency, the time series of the tube profile was parsed into equal sections coincident to the application of the electrical pulse. These sections were subsequently averaged to obtain a temporal mean of the contraction cycle. Each line in Figure 4.7 represents a time point in this averaged contraction cycle. The number of lines or time points decreases with increasing contraction frequency since the rate of image capture is constant for all the different frequencies.

Figure 4.7 provides an overview of the tube dynamics for the fully seeded pump. As can be seen from the plots, the contraction ratios are nonuniform along the length of the tube. This nonuni-

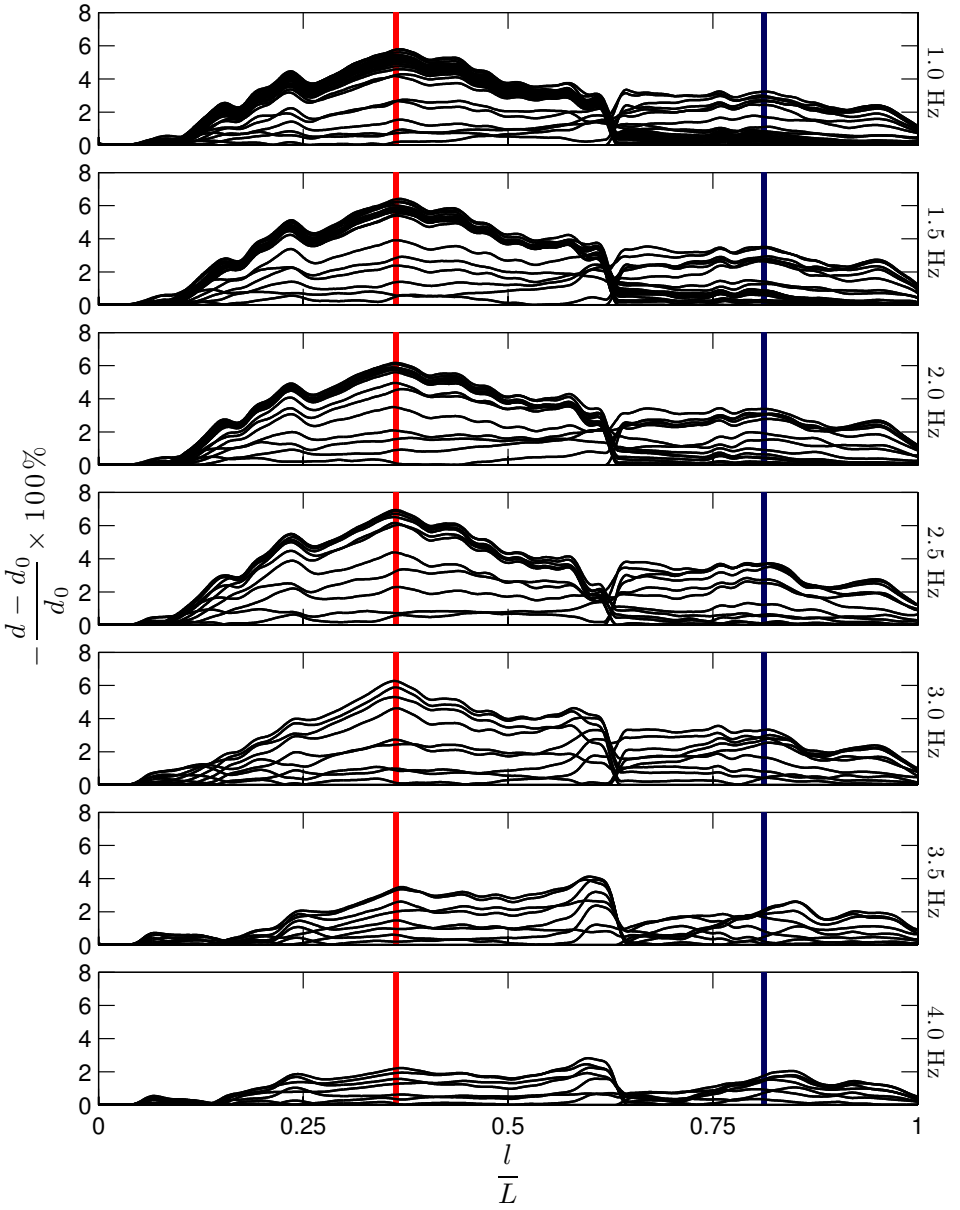

Figure 4.7. Contraction ratios along the longitudinal axis of the pump body for a fully seeded muscular pump under forced electrical stimulation. Each line represents a time point in the contraction cycle. The red (light) and blue (dark) lines mark the position of points on the left and right side of the tube where maximum expansions and contractions are observed. The plots were generated by the temporal average of all contractions for each frequency to obtain a mean contraction profile.

formity contributes to the systemic asymmetry that is required to generate flow in the impedance pump. Moreover, the plots corresponding to the the low frequencies of contraction (1 and 1.5 Hz) in Figure 4.7 reveal the resting state of the tubular body of the pump. As each contraction and recovery takes less than the full period for these frequencies, several time points corresponding to the resting state crowd together and produce the visual effect seen in the plots. Normally, one would expect the resting position of the tube to correspond to no contraction or $CR = 0$. This is true on the right side of the pump depicted in Figure 4.7, while the resting position for the left side corresponds to the maximum values of CR. This suggests that the left side of the tube experiences an expansion rather than contraction. To further explore this observation, the points where maximum expansion and contraction occur are investigated in Figures 4.8 and 4.9.

A comparison of the contraction ratios for the various frequencies of Figure 4.7 reveals an initial increase in CR values up to a beating frequency of 2.5 Hz followed by a decrease in CR values at stimulation frequencies beyond 2.5 Hz. This phenomenon could be due to a combination of factors having to do with the physiological response of the actuating cardiomyocytes to the frequency of actuation as well as physical factors relating to the deformation and restoration of the tube wall. Both positive and negative force-frequency relationships are observed in the studies of cardiomyocytes [42]. The initial positive force-frequency relationship could be due to frequency dependent uptake and release of Ca^{2+} by the sarcoplasmic reticulum, as the net uptake of calcium by the cell increases due to the higher frequency of stimulation [43]. The negative force-frequency relationship at high frequencies could be due to inadequate supply of O_2 to the constructs, reductions in levels of Ca^{2+} released from the sarcoplasmic reticulum, or a reduction in the time available for Ca^{2+} to activate the contractile machinery of the cells. Higher forces generated by the cardiac muscle cells translate to larger deformations of the elastic scaffolding tube, while smaller forces result in smaller contractions. These explanations do not take into account the complex fluid-structure interactions of the fluid-filled tube which can also contribute to the observed behavior.

An initial glance at the plots of Figure 4.8, which represents the deviation from the mean diameter at the two points of interest, indicates that the oscillations at the two points are out of phase with

one another. Decreases in the diameter or contractions at the right side of the tube (blue curves) coincide with increases in the diameter or expansions at the left side (red curves). Comparing the timing of the electrical pulses with the onset of contraction in the blue curves and expansion in the red curves along with the fact that electrical stimulation is nearly simultaneous for all the muscle cells suggest that the expanding side of the pump responds to the contraction cycles of the right side. The relatively larger amplitudes of motion at the passive side of the pump compared to the active side could be explained by the nonuniformities in the contractions around the tube circumference or by the rotations of the tube with an oblong circumference as opposed to the assumed axisymmetric profile–informations that are not captured in the two dimensional image representation of the pump body.

Further scrutiny of the plots of Figure 4.8 reveals that it takes a few cycles for the electrically stimulated tissue-engineered constructs to adjust to the frequency of stimulation and develop a uniform contraction profile. The is evident, for example, in the case of stimulation at 1 Hz, where 2 contractions are recorded within the first second of field stimulation.

At low frequencies of stimulation, clear contraction profiles with steady amplitudes of contraction develop. At higher stimulation frequencies, the contraction profiles become less regular. For instance, the plot of stimulation at 4 Hz reveals undulating amplitudes of contraction. The reduction and subsequent recovery in amplitudes of contraction point to calcium rather than oxygen supply as the determining factor for the observed negative force-frequency behavior.

Figure 4.9 shows the spectral analysis for the two inspected curves of Figure 4.8. At low frequencies of stimulation, the constructs follow the excitation frequency closely with sharp peaks coinciding with the frequency of electrical pulses and repeated peaks at the harmonics of the maximum peak. At higher frequencies, these peaks are still present with less prominence.

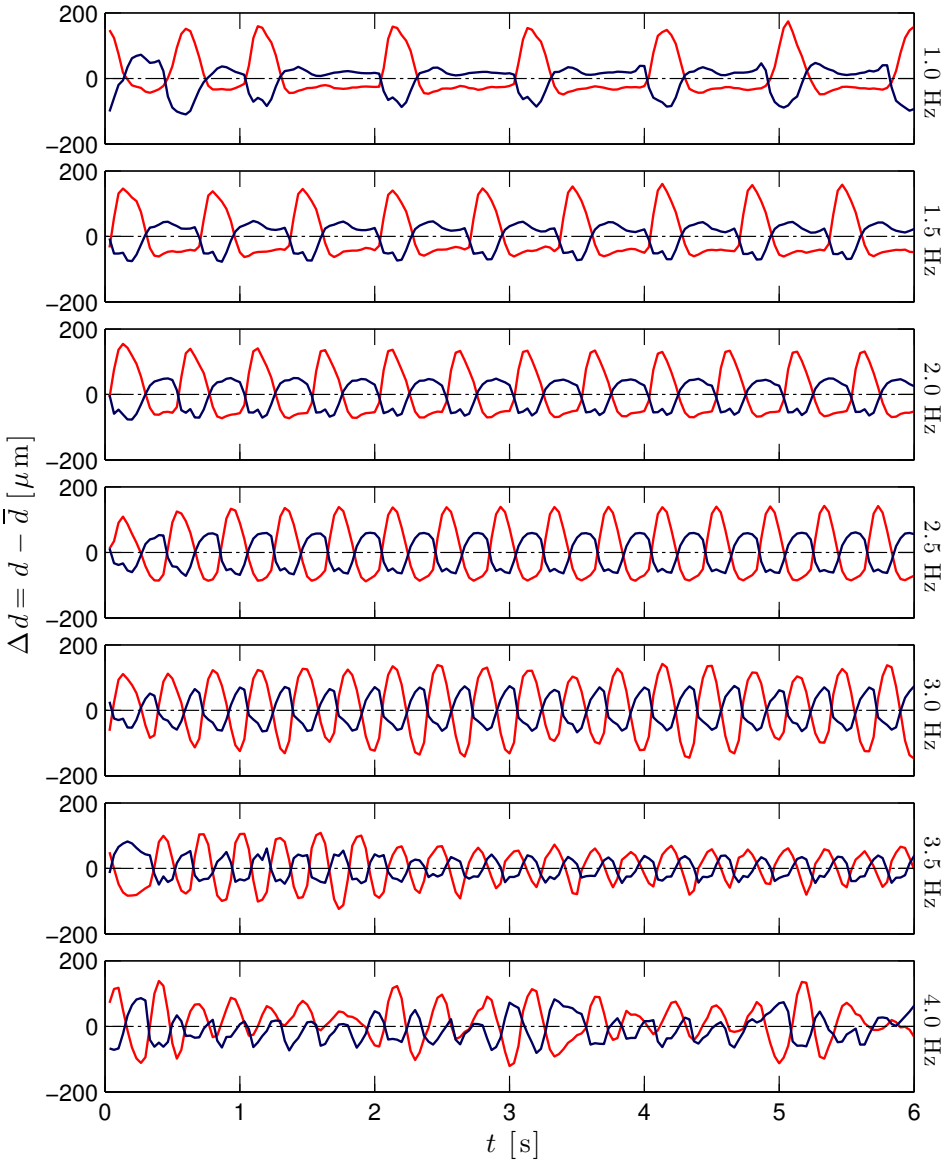

Figure 4.8. Deviations from the mean diameter at two points of interest on a fully seeded muscular pump. The red (light) and blue (dark) curves correspond to the similarly identified curves in Figure 4.7. Captured images and electrical stimuli are synchronized, and $t = 0$ corresponds to the delivery of the first electrical pulse for each plot.

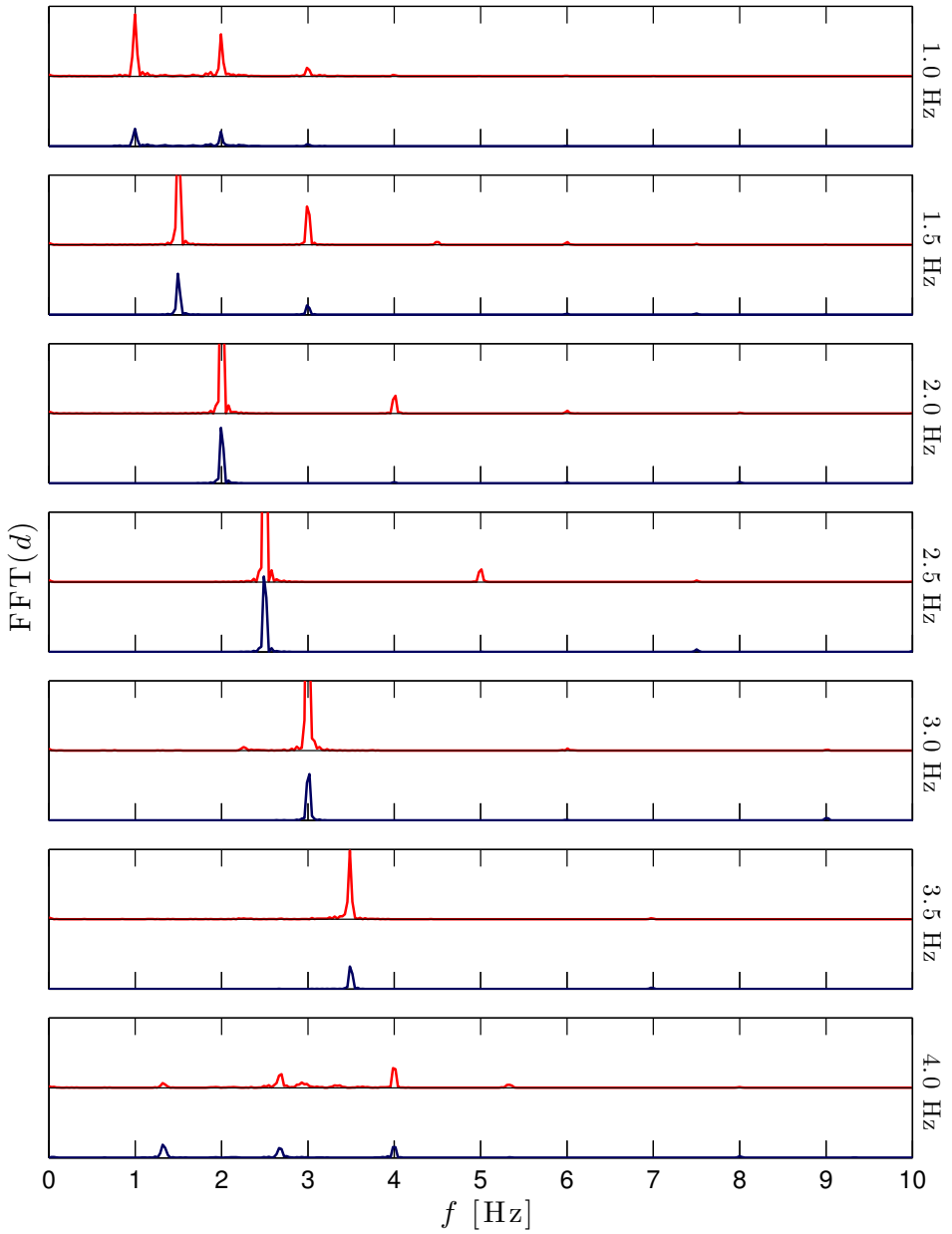

Figure 4.9. Spectral power analysis for the contraction curves of Figure 4.8. The plots are made on the same scale.

4.3.2 Flow Response under Forced Electrical Stimulation

If the pump body and its muscular actuator were symmetric in every aspect, one would expect no mean flow for the valveless impedance pump, as discussed in Section 2.3. Upon actuation of the pump, the fluid would oscillate back and forth with no net mean displacement. Such is not the case. The tube diameter along its length is not uniform. The self-assembled muscular actuator of the pump is also not uniform along its length or circumference. These asymmetric characteristics of the fully seeded tissue-engineered constructs are believed to contribute to the net flow that is observed and presented in this section.

In order to visualize and measure the flow response to the beating frequency of the pump, tracer particles were used in the flow-loop of the bioreactor as detailed in Section 3.5. The images captured from a clear section of the flow-loop were analyzed and the particles were tracked. Figure 4.10 shows the motion of representative particles for each of the frequencies of stimulation. As is evident from these plots, the tracer particles exhibit oscillatory motion in response to the oscillatory flow generated by the contracting pump. These oscillations are similar in frequency to the frequency of stimulation as can be seen in the spectral analysis of the particles' motion in Figure 4.10.

Also manifested in Figure 4.10 is the undulating amplitudes of the tracer particle's motion at 4 Hz stimulation which is also observable from the corresponding plot in Figure 4.8. The variations in the amplitudes of the oscillatory component of the flow in response to changes in the amplitudes of actuation demonstrate the close relationship between the amplitudes of excitation and generated flow, as was previously discussed in Section 2.3.

The tracer particles of Figure 4.10 move in a clockwise direction or negative sense about the flow-loop, as defined by Figure 3.6. This is consistent with the previous experimental observations of the impedance pumps where the first resonant peak occurred with flow in the direction of least compliance [47]. This is perhaps due to a pressure differential induced by the difference between the compliance of the active and passive regions of the tube. At the low frequencies of excitation, the less compliant section of the tube (the actuator region) creates higher local pressures than the more compliant section of the tube. This pressure differential drives the flow around the flow-loop in the

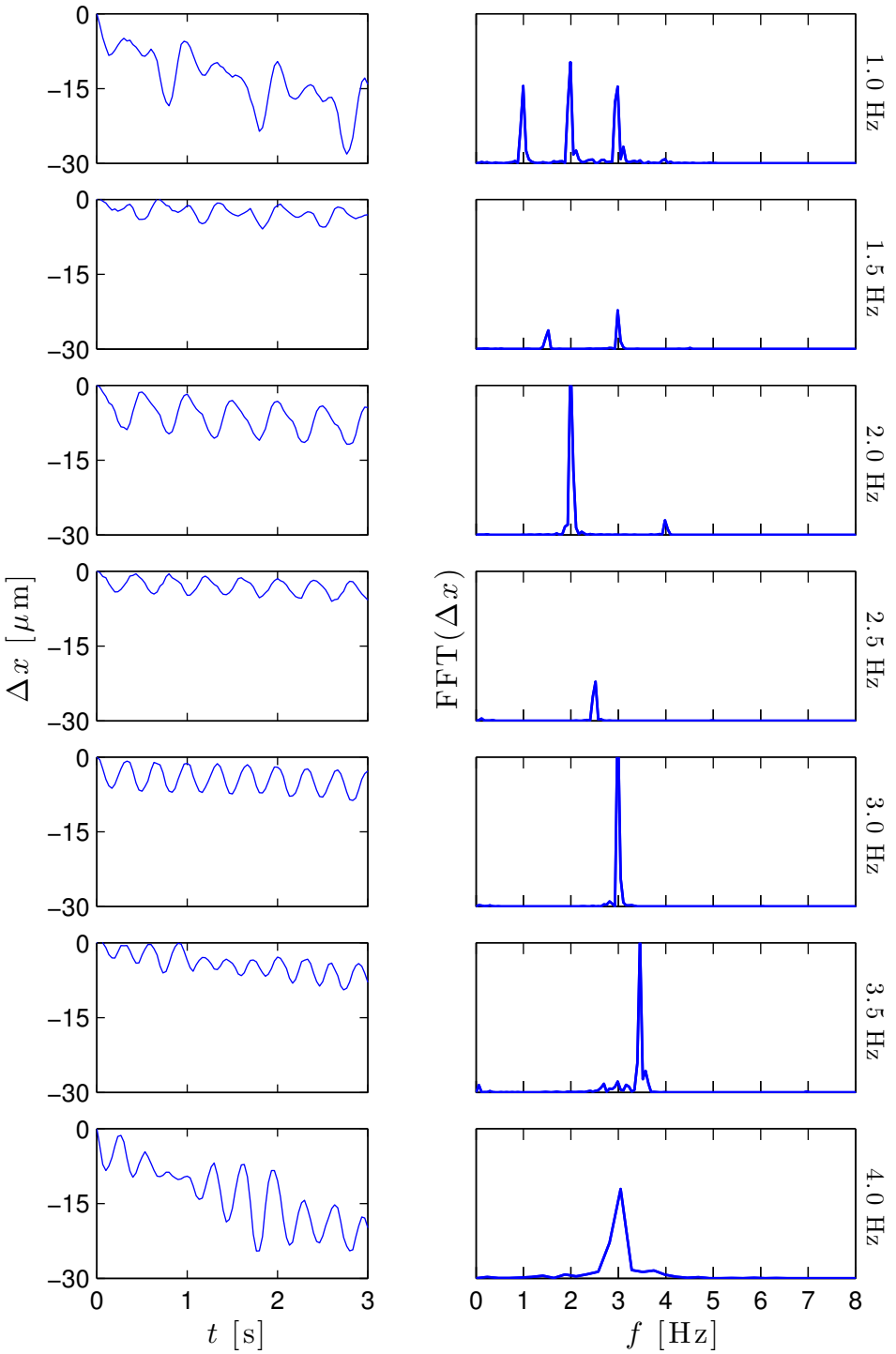

Figure 4.10. Time and frequency domain representation of selected tracer particle displacements in response to the flow generated by the fully seeded pump. The particles exhibit an oscillatory motion which follows the frequency of stimulation. The particles move in a clockwise direction or negative sense as defined in Figure 3.6

negative sense for the fully seeded pump presented here.

The mean displacements of the tracked particles were used to obtain mean flow velocities. The particle tracking program uses extrema in the image intensity for particle detection. Inevitably, undesired background extrema in intensity are falsely detected as particles. The oscillatory motion of the particles was used as a criteria for rejecting these background particles that do not move with the flow. The coordinates of each particle was fitted to the best line in a least squares sense. The slope of this line represents the mean velocity for the particle. This linear displacement of the particle was subtracted from the original coordinates to obtain the oscillatory component of the particle's motion. The particle's oscillatory component of motion was subsequently analyzed using fast Fourier transform to obtain its spectral power in the frequency domain. If the peak frequency component was not within a predefined neighborhood of the stimulation frequency, the particle would be rejected and not included in the calculations of mean velocity.

Figure 4.11 depicts the mean velocity profile for particles as viewed in the tubular region of the flow-loop and as calculated from the analysis above for the excitation frequencies that were explored. Each point represents a tracked particle that followed the criteria above. The vertical coordinate corresponds to the radial position of the particle in the tube, and the horizontal coordinate provides the mean velocity for that particle as calculated from the slope of the regression line that was fitted to the particle's motion along the longitudinal axis of the tube.

It would be expected that all particles of the same radial coordinate to have identical velocities and to coincide on the plots of Figure 4.11, yet variations exists in the calculated velocities as is evident from the horizontal spread in the plotted velocity profiles. This artifact is attributed to detection of particles outside the focal plane of the stereomicroscope. Particles detected at different z levels but at apparent identical location in the image would have unequal velocities due to their different proximity to the tube wall. This point is discussed in further detail in Appendix B. For this reason, the maximum velocity at each radial position is believed to define the velocity profile. As parabolic velocity profiles are characteristic for flow inside tubes, a parabolic fit to the outer bound of the velocity data is used to approximate the mean velocity profile generated by the pump.

It should be noted that the parabolic regression lines of Figure 4.11 do not always conform to the mean velocity profile of the particles. This is perhaps due to the shear-induced migration of the particles to the center of the tube as the particles travel along the longitudinal axis of the tube [10].

The maximum values at the cusps of the fitted curves, $\overline{u}_{\max}$, of Figure 4.11 are used to approximate the maximum flow at the center of the tube. Mean volumetric flows, $\overline{Q}$, were calculated for each frequency using

$$\overline{Q} = \frac{1}{2}\overline{u}_{\max}A_c, \tag{4.2}$$

where A_c is the cross section of the tube. Figure 4.12 is the culmination of these calculations, showing the nonlinear flow response to the frequency of excitation. Although small relative to the displacement induced by the drag forces of the moving fluid on the tracer particles, other physical driving forces such as Brownian motion can contribute to the particles' displacement. The resulting uncertainties are represented as error bounds in the flow rate calculations of Figure 4.12.

The nonlinear flow response of the muscular pump to the frequency of excitation was expected as it is a characteristic behavior of the valveless impedance pump. This observed response of the pump could be further due to the nonlinear response of the muscular actuator to the frequency of excitation, as the amplitudes of contraction could not be independently controlled.

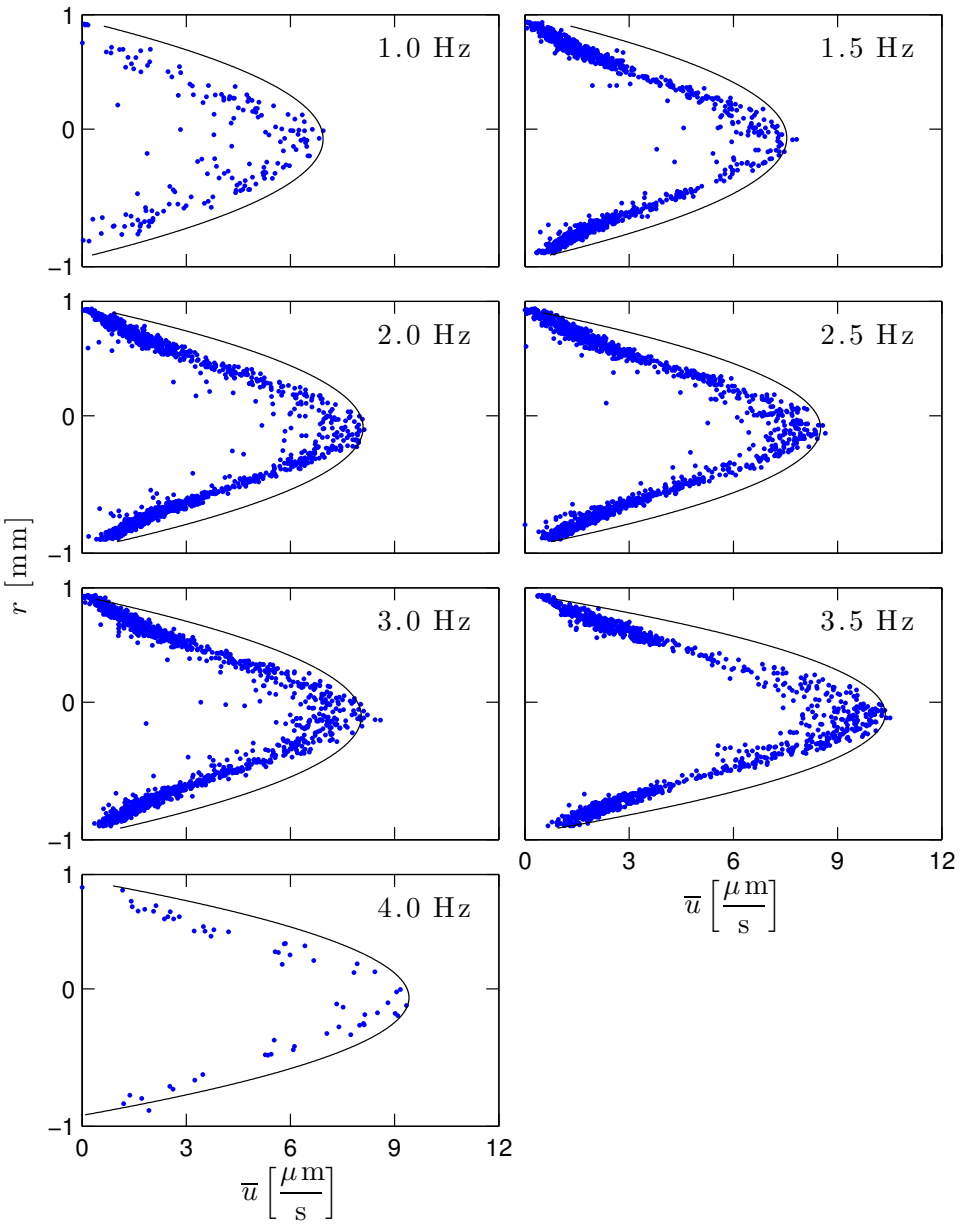

Figure 4.11. Distribution of particle mean velocity along the longitudinal axis of the tube. Each point represents a tracked particle with the vertical axis indicating the position of the particle along the radial coordinate of the tube and the horizontal axis representing the particle's mean velocity.

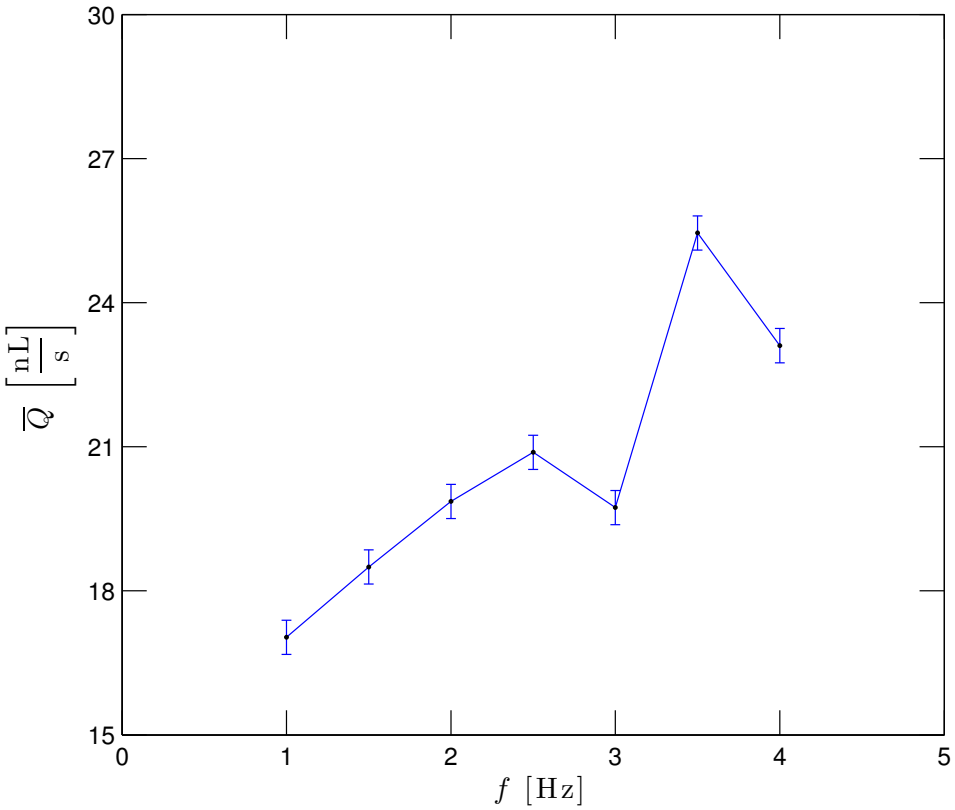

Figure 4.12. Magnitude of mean volumetric flow rate, $\overline{Q}$, as a function of the frequency of excitation for a fully seeded muscular pump.

4.4 Frequency Response Characterization of a Selectively Seeded Tissue-Engineered Pump

The initial objective of this work, as described in Chapters 1 and 2 was to tissue engineer a pump that followed the working principles of the valveless embryonic heart tube. This objective required the ability to develop a clearly defined actuator for the pump. To this end, a physical masking mechanism was developed as described in Section 3.3 to selectively seed the harvested cardiac muscle cells onto the scaffolding matrix so that they would self-assemble into a predefined muscular band. Fluorescent staining was used to verify the efficacy of this seeding method. Figure 4.13 shows Z-section fluorescent images from the muscular band region of one such pump, stained for the cell nuclei. Each bright spot in the images of Figure 4.13 represents the nucleus of a cell attached to the tubular scaffold. No concentration of cells were observed outside the defined muscular band region.

Many of the discussions presented in the prior section on the fully seeded muscular pump hold true and are observed for the selectively seeded pump that is discussed here in further detail.

4.4.1 Tube Dynamics under Forced Electrical Stimulation

The contraction ratios, as defined by Equation (4.1), are plotted for the muscular band actuated pump in Figure 4.14. The actuator of the pump had a width of 7.5 mm which is approximately equal to a third of the length of the tube. The actuator was positioned asymmetrically from the ends of the tube with its center approximately at $\frac{L}{4}$, as indicated in Figure 4.14. Contraction ratios achieved were relatively lower than those observed for the fully seeded pumps of Section 4.3. The contraction profiles displayed by the muscular band actuated pumps were also different. As can be seen from the plot of stimulation at 1 Hz, the tube's resting state coincides with zero contraction. Furthermore, similar frequency dependance was observed for the amplitudes of contraction. A positive force-frequency relationship existed for frequencies of excitation up to 2.5 Hz, at which point increases in frequency resulted in decreases in contraction amplitude.

For the explored excitation frequencies, the contraction ratio was highest at $\frac{L}{4}$, which corre-

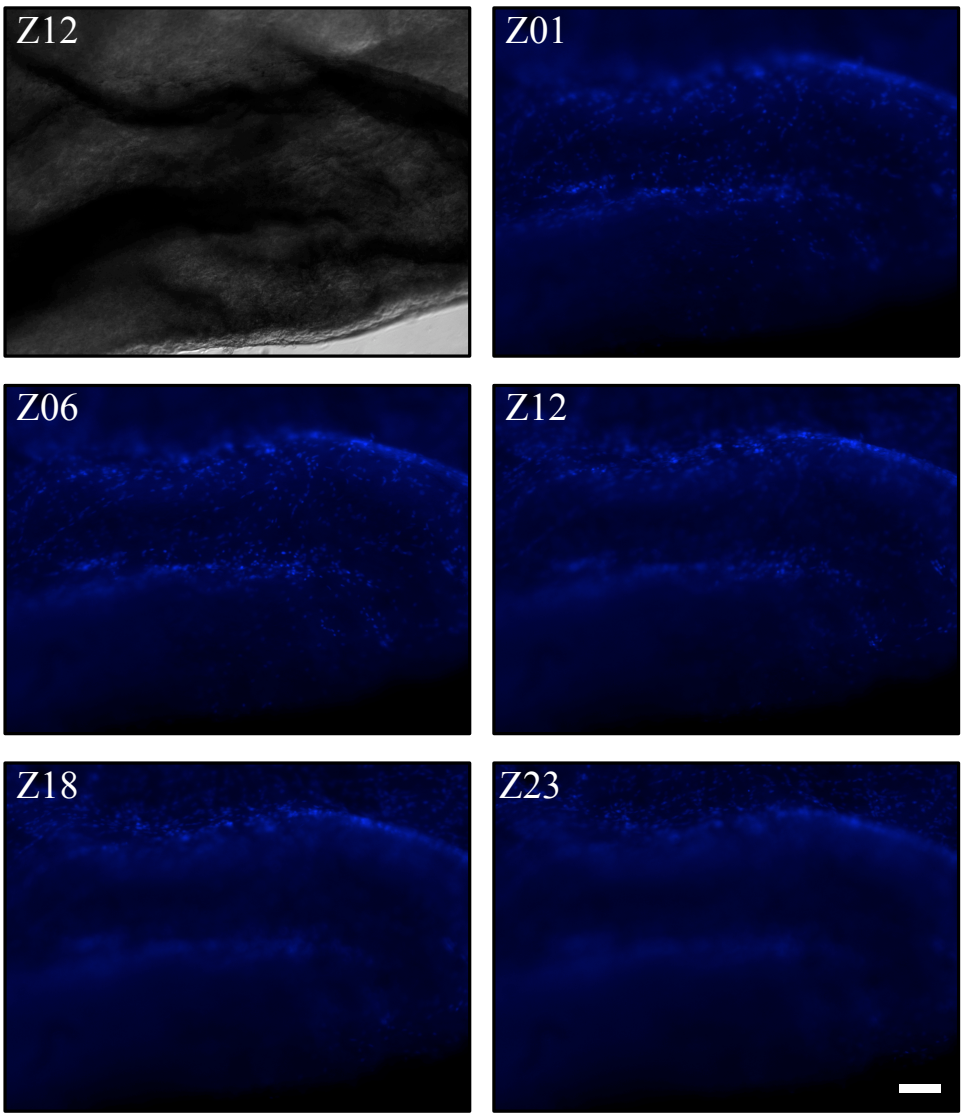

Figure 4.13. Bright field and fluorescent Z-section images for a selectively seeded region of SIS tube showing the fluorescently labeled nuclei of the cells. Scale bar = 100 µm; $\Delta Z = 12$ µm.

sponded to the location of the cardiomyocyte band. Also conserved among frequencies was diminishing of CR values at the ends of the tube where the pump was in contact with the rigid glass tubes of the flow-loop. The contraction profiles of the point of maximum contraction and a point near the center of the tube are explored in time and frequency domains as indicated by the red (light) and blue (dark) lines in Figure 4.14.

The time representation of the contraction ratios for the two points of interest in Figure 4.15 shows that the point corresponding to the passive part of the pump clearly follows the actuations from the active part with amplitudes of wall motion that are smaller than the active part. The contraction profiles for the muscular band actuated pump appear more regular compared to those of the fully seeded pump.

Fast Fourier transform analysis of the tube diameter at the actuator location reveals that the pump responds closely to the stimulation frequency with occasional exceptions in the case of stimulation at 1 Hz, as can be seen in Figure 4.16. For the forced electrical stimulation at 1 Hz, the actuator responds at a higher frequency of 2 Hz, although the waveforms are not equally spaced and are not of exact same amplitudes. The additional contractions could be attributed to the spontaneous activity of the cardiomyocytes actuating the pump which occurs at a frequency higher than the excitation frequency. This aberration provided us with an opportunity to compare the pump dynamics under spontaneous and forced actuations.

Figure 4.17 plots wall displacement as deviations from the mean diameter for the actuator location of the pump and Figure 4.18 shows the corresponding wall displacement velocity, v, defined as

$$v(l,t) = \frac{\partial d}{\partial t}, \tag{4.3}$$

where v is both a function of time and the longitudinal position along the tube.

A comparison between the plots of excitation frequency at 1 and 2 Hz in Figures 4.17 and 4.18 reveals that the spontaneous contraction which follows the electrical stimulation at 1 Hz occurs slightly after what would have been the second forced stimulation in the case of actuation at 2 Hz. This allows for further relaxation of the tube and restoration of the tube diameter to its undisturbed state.

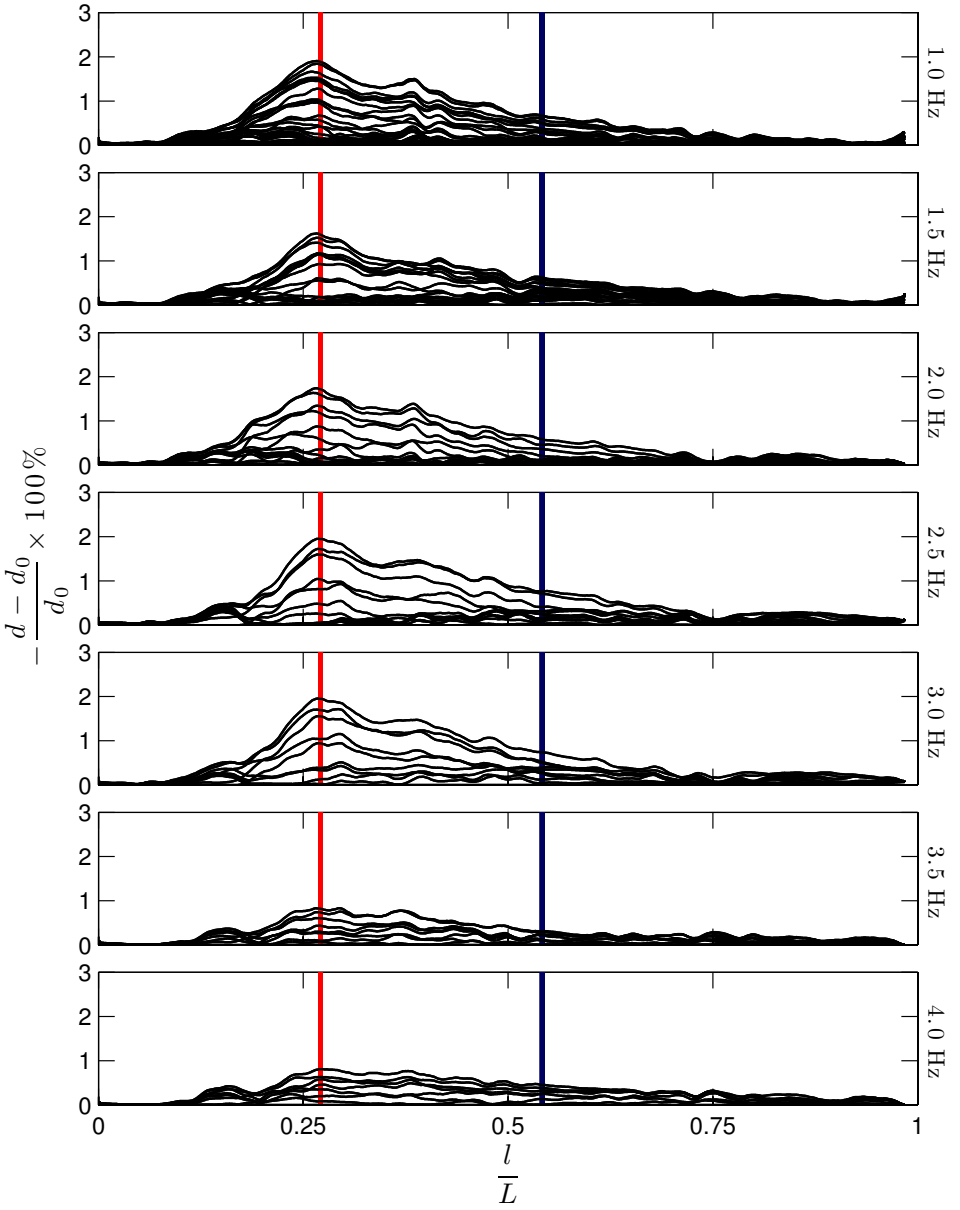

Figure 4.14. Contraction ratios along the longitudinal axis of the pump body for a selectively seeded muscular pump under forced electrical stimulation. Each line represents a time point in the average contraction cycle. The red (light) line marks the position of maximum contraction and coincides with the muscular band actuator of the tissue-engineered pump. The blue (dark) line marks the position of a second point near the center of the pump where the contraction profile is further studied.

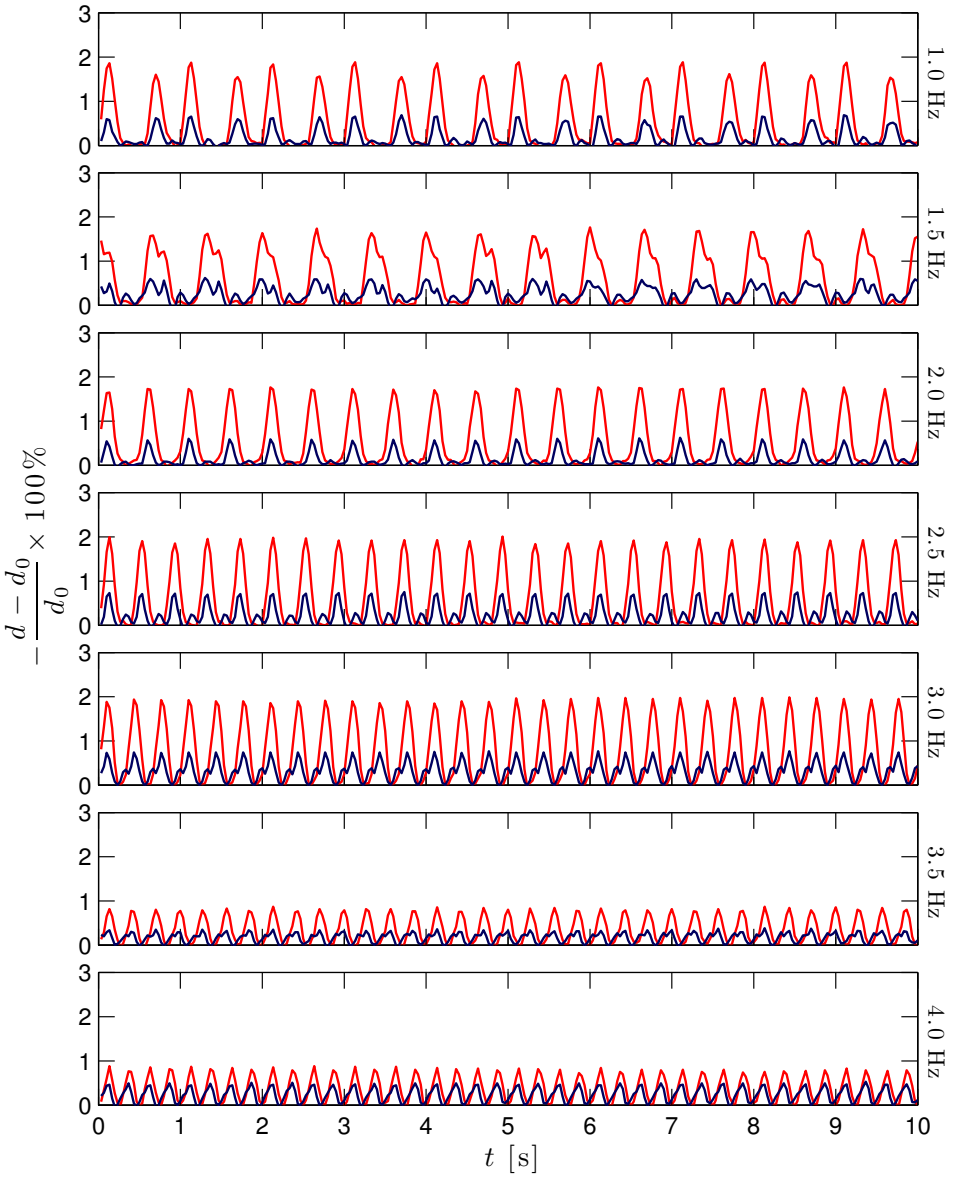

Figure 4.15. Temporal representation of the contraction ratio for two points of interest. The red (light) and blue (dark) curves correspond to the similarly identified curves in Figure 4.14.

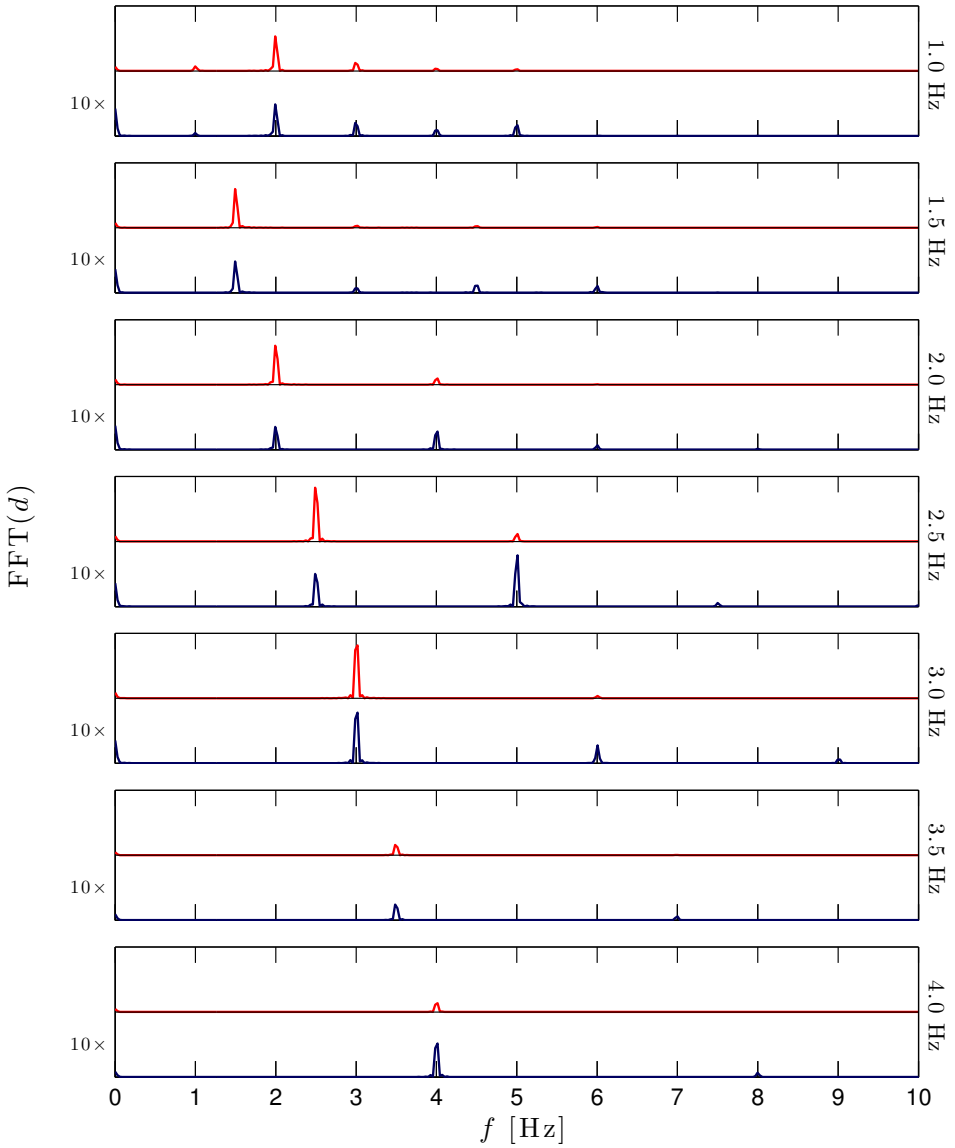

Figure 4.16. Spectral power analysis for the contraction curves of Figure 4.15. The plots for the blue (dark) curve are scaled up by a factor of 10 for clarity.

Nonetheless, both spontaneous and forced stimulations exhibit similar displacement magnitudes and velocities. These observations indicate that the synchronous activity of spontaneous contractions is due to the presence of electrical coupling among the mechanically coupled cardiomyocytes that contribute to the contraction of the tube. The spontaneous contractions following the forced electrical stimulation can also explain the distinct wall displacement and velocity profiles exhibited by the pump when stimulated at 1.5 Hz, where a small contraction follows the forced electrical stimulation. This secondary contraction apparently does not generate enough force to fully overcome the restoration force of the tube wall.

Negative velocities in Figure 4.18 correspond to the contraction of the tube diameter, while positive velocities represent the restoration phase of the tube dynamics. The relatively horizontal lines at $v = 0$ in Figure 4.18 signify rest states, while crossing the line $v = 0$ represents the onset of contraction or recoil. A closer look at the rest states of the wall displacement reveals that these rest states diminish with increasing frequency of excitation. In fact, at higher frequencies, the tube wall does not fully restore to its rest state, and oscillates between its point of maximum contraction and another constricted state. This constricted state is dictated by the frequency of contractions which determines the restoration time for the tube wall. This can additionally contribute to the observed dependance of the contraction amplitudes on the frequency of excitation.

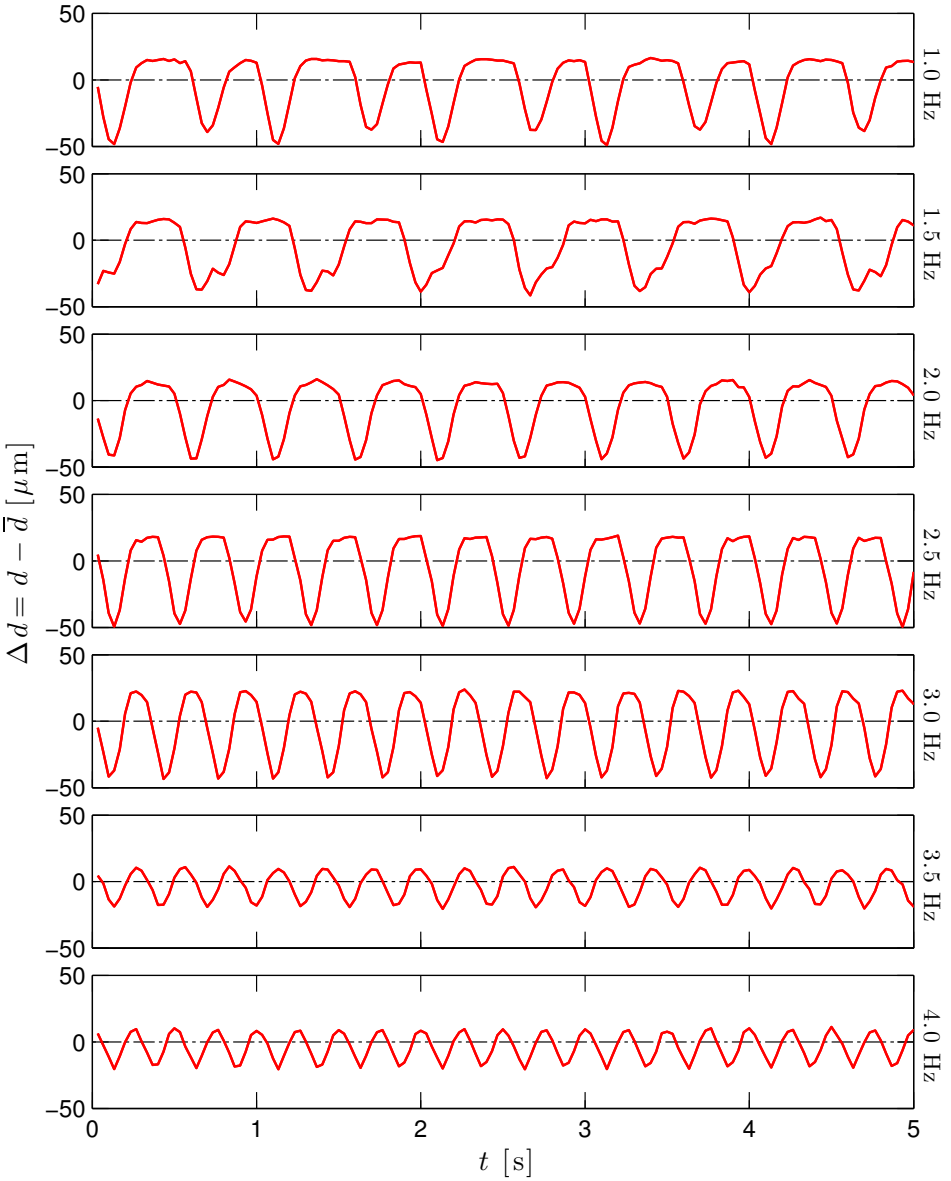

Figure 4.17. Displacement time-course for the point of maximum contraction for a partially seeded pump.

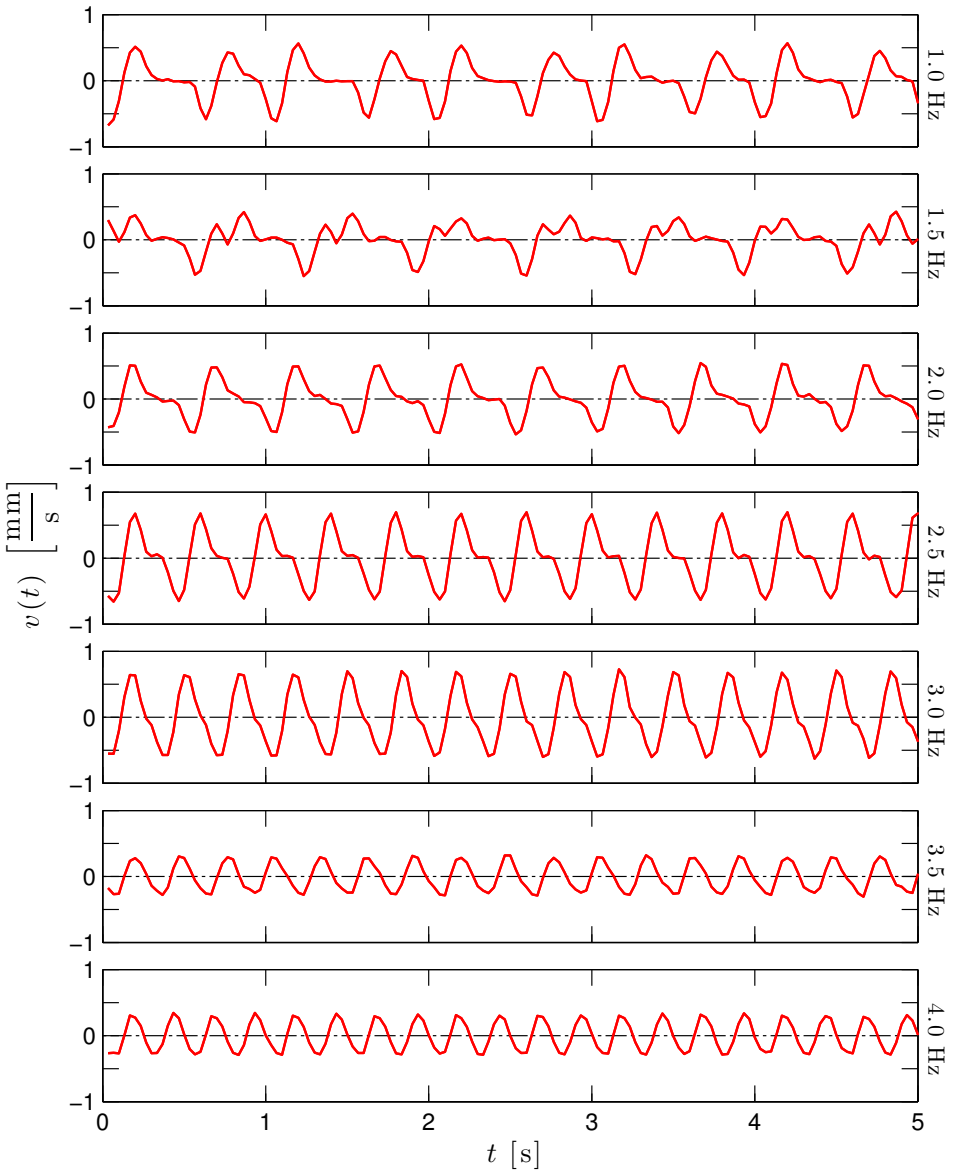

Figure 4.18. Wall displacement velocity profile for the point of maximum contraction for the muscular band actuated pump. Relatively horizontal lines at $v = 0$ signify rest states, while crossing the line $v = 0$ signifies the onset of contraction or recoil.

4.4.2 Flow Response under Forced Electrical Stimulation

The flow response for the muscular band actuated pump described here was characterized in a similar manner to the discussions of the previous section. Figure 4.19 shows representative particles tracked by the particle tracking program of Section 3.6.2. As can be seen from the plots of particle displacement versus time, at higher frequencies of excitation, the motion of the particles is more regular than the particle displacements observed for the fully seeded pump. This fact was also reflected in Figure 4.15 which showed more regular tube contractions. Also evident in Figure 4.19 is the similar peaks in the spectral analysis of the particle displacement to those seen for the tube wall motion in Figure 4.16. The smaller peaks observed in the particle displacement profile in the plot for excitation at 1 Hz could be due to the delayed spontaneous contractions following the response to the electrical stimulation.

As is evident from the particle displacement profiles of Figure 4.19, the pump generates a net mean flow with a retrograde component due to the back-flow of fluid that occurs during diastole. These flow characteristics resemble the flow behavior observed in the valveless embryonic vertebrate heart. The mean particle motion in response to the flow generated by the selectively seeded pump is in the positive sense defined previously. This is consistent with the position of the muscular actuator as discussed in Section 4.3.2.

Examining the average volumetric flow as a function of the frequency of stimulation in Figure 4.21, a nonlinear response can be observed with the maximum flow occurring close to the natural beating frequency of the pump. The volumetric flow rates generated by the selectively seeded pump are lower than those observed in the fully seeded pump. The lower flow generation could be due to the smaller contraction ratios of the muscular band actuated pumps.

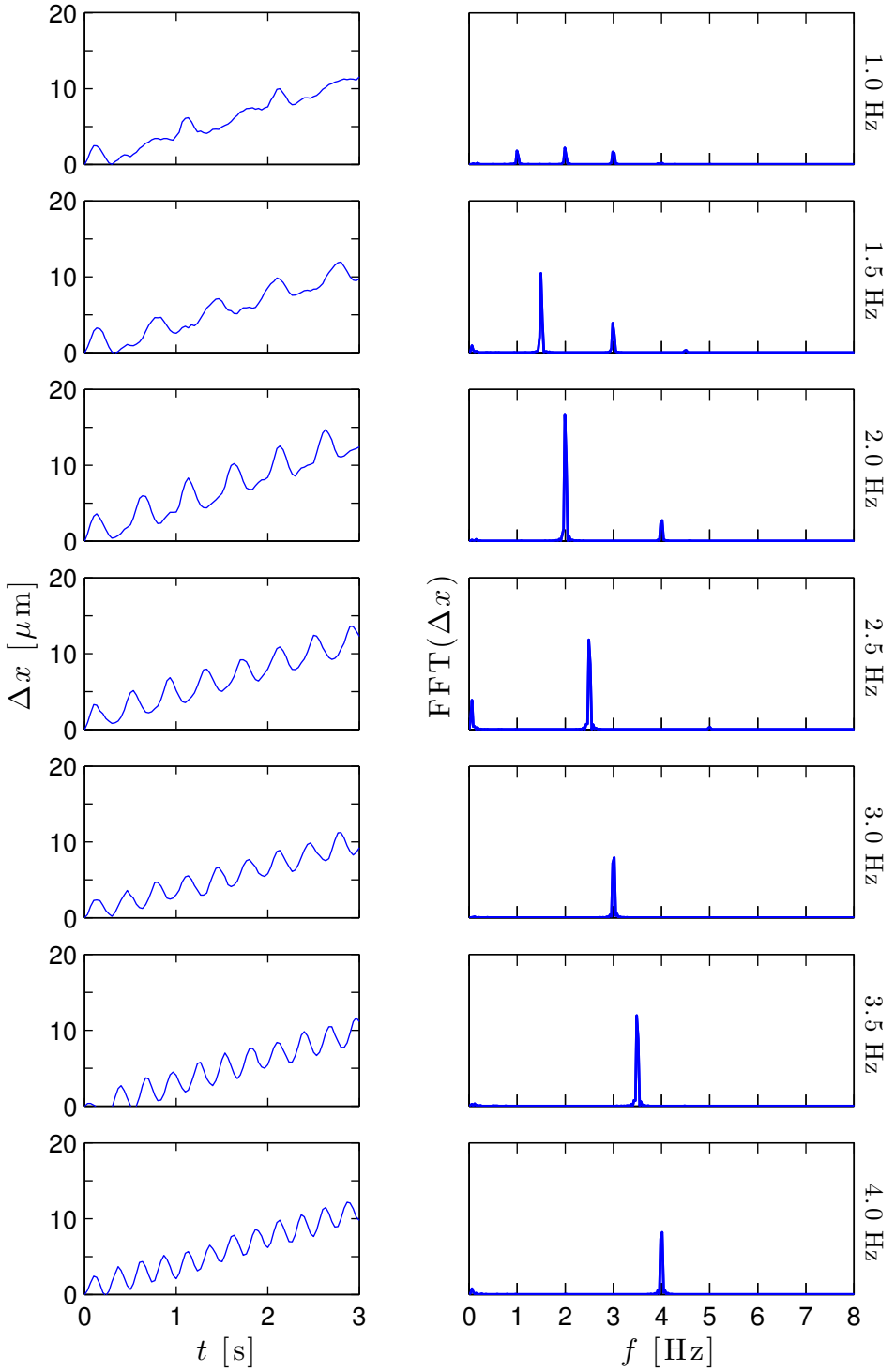

Figure 4.19. Time and frequency domain representation of selected tracer particle displacements in response to the flow generated by the partially seeded pump.

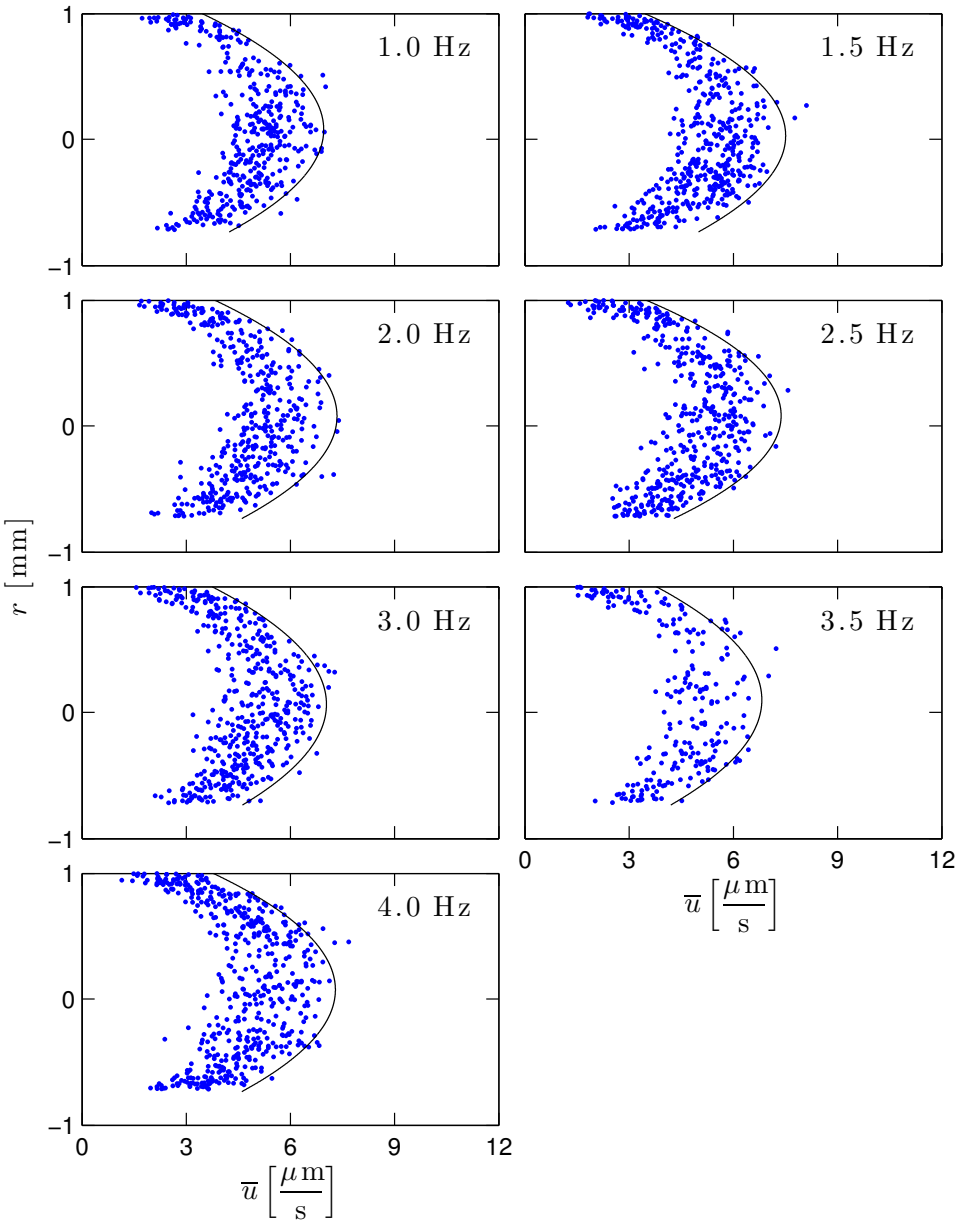

Figure 4.20. Distribution of particle mean velocity along the longitudinal axis of the tube as a consequence of the flow generated by the partially seeded pump. Each point represents a tracked particle with the vertical axis indicating the position of the particle along the radial coordinate of the tube and the horizontal axis representing the particle's mean velocity.

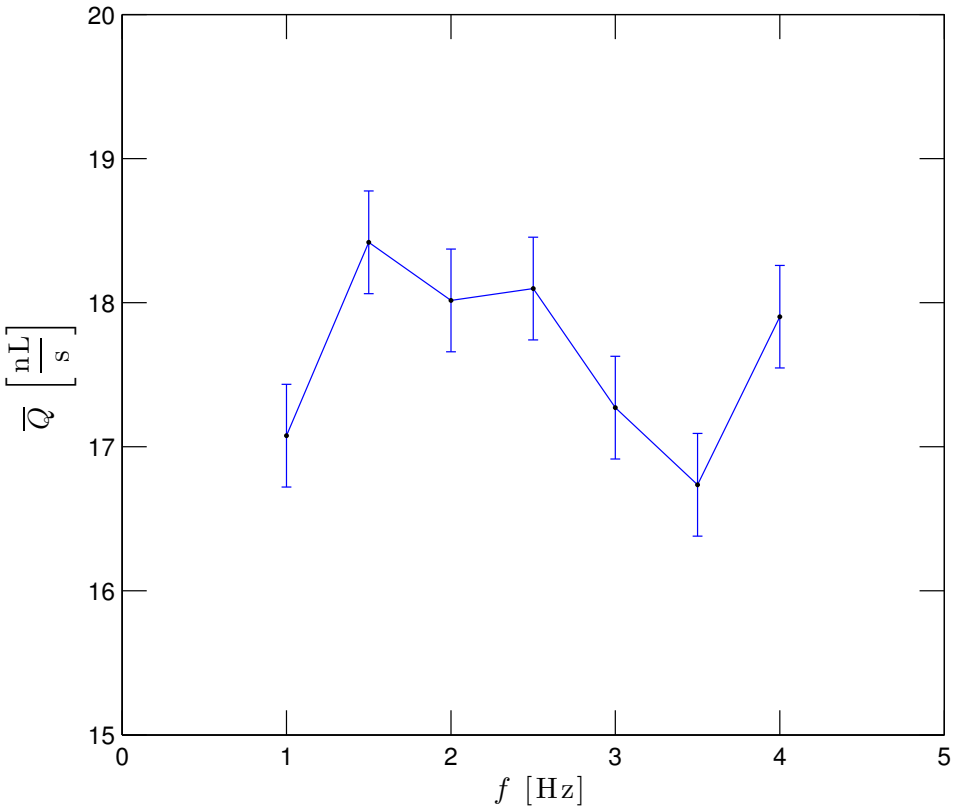

Figure 4.21. Magnitude of mean volumetric flow rate, $\overline{Q}$, as a function of the frequency of stimulation for the muscular band actuated pump.

Chapter 5

Concluding Remarks and Future Directions

The results presented in the previous chapter have clearly demonstrated the feasibility of tissue engineering valveless muscular pumps that are powered by biological means. As the complexity of biological machines increase, the need for a circulatory system for their sustenance becomes unavoidable. One can envision a more elaborately engineered biological pump, capable of transporting fluids for feeding or propulsion, serving as the heart or the engine of a more complex biological machine.

In general, it is not necessary to have a contained muscular band to generate flow. Lack of symmetry either due to tube morphology or cellular adaptations and arrangements can be a driving force for the generation of flow, as was shown for the fully seeded pumps. Nevertheless, actuation by a muscular band displayed a more regular and predictable behavior than when no clearly defined actuator was used.

Many physical factors influence the performance of the valveless impedance pump as discussed in Section 2.3. The living components of the tissue-engineered pumps are also affected by many physical and physiological factors, compounding the complexity of the system. These physiological factors should be appreciated for successful engineering of biologically powered devices.

The tube dynamics and the resulting flow inside a mechanically actuated elastic tube is a complex one that has been the subject of many studies. In characterizing the tissue-engineered pumps, it is not possible to fully decouple these complex interactions from the physiological response of the cardiac cells that were used for actuating the pump. Cellular fatigue due to lack of oxygen or nutrients can

affect the system's performance as would other factors such as the ambient temperature and the concentration of ions that are critical for the contractile behavior of the cardiac cells.

Bio-inspired design, when employed with a deeper understanding of the physical principles and parameters involved in the model system, can be a successful design strategy in the process of engineering such biological devices. In selecting the components for biologically composed machines, consideration of the building blocks' ability to fall within the parameter space satisfying these physical principles is of paramount importance.

With regard to biomedical devices and tissue-engineered artificial organs intended for patient use, the work presented here is a significant step forward in manufacturing a functional device using only living cells and biologically derived building blocks. With advances made in stem cell research, fully autologous biological pumps could be constructed in a similar fashion by using cells and tissue from patients as the primary source of required biological material. This topic and other possible future directions are discussed in the following section.

5.1 Future Directions

Human knowledge and innovation relies on the work of many generations of scientists and innovators. In the same way that this work was motivated and benefitted from the findings and observations of others, it is hoped that the demonstration of the possibility of designing and building a functional device solely out of living and biological building blocks can serve as a stepping stone for future innovation. The following discussions relate to possible future directions that hold the potential to improve the reliability and function of the tissue-engineered muscular pumps. Such improvements can possibly bring us closer to the ultimate goal of engineering patient specific living implantable devices that self-sustain and regenerate.

5.1.1 Physical Stimuli for Cellular and Subcellular Organization

Cells within the native tissue are exposed to a host of physiological stimuli from their native environment that include chemical, electrical, and mechanical signals. Electrical stimuli are present

in both the developing and adult heart. Contraction of cardiac muscle is driven by the waves of electrical stimulation generated by the pacing cells of the heart. *In vitro*, electrically stimulated tissue-engineered cardiac constructs have exhibited better electrochemical coupling and superior cytoskeletal arrangement [25]. Also present in the native cardiac tissue are mechanical stimuli brought about by the repeated contractions of the myocardium and increased pressure in the developing heart. The effect of mechanical forces exerted on muscle cells through static and cyclic stretching has been extensively investigated *in vitro*. Stretched cardiac cells become elongated and align themselves and their cytoskeleton according to the direction of stretch [70]. Mechanical stimulation has also been shown to regulate focal adhesion and costamere assembly in the cardiac cells, along with regulation of a number of other relevant proteins [61].

In tissue engineering the pumps presented in this study, these biophysical stimuli were absent and we relied on the self-assembly of the cardiac cells into a contractile band; however, the homogeneous distribution of adhesion glycoproteins such as fibronectin in the extracellular matrix of scaffolding small intestinal submucosa did not afford us the ability to align the cardiac cells anisotropically on the circumference of the tube. Future utilization of mechanical and electrical stimuli while growing the pumps may partially alleviate this problem and lead to higher degrees of cell alignment and mechanical end-to-end coupling of the cardiac cells which in turn would result in increased strength and amplitude of contractions.

5.1.2 Addition of Valves as the Next Developmental Stage

As the circulatory needs of an organism increase, nature has devised more efficient ways of transporting fluids by including valves in their hearts. The inclusion of valves allows for generation of higher pressures and prevents the back-flow of blood. Integration of valves in order to prevent back-flow can enhance the performance of the tissue-engineered muscular pumps in ways that mirror the natural course of cardiac development in vertebrates.

A possible mechanism for engineering such valvular muscular pumps is through the process of 3D printing. Both valves and tubular geometries have been developed through this technique [16, 53].

The valve and tubular components can be integrated through this additive process. Furthermore, 3D printing can allow us to explore variations in the tube diameter as well as tube materials.

5.1.3 Stem Cells for Tissue Engineering Muscular Pumps

One of the major endeavors of the field of tissue engineering is the identification of suitable cell sources for construction of tissue alternatives. For the purpose of implantable biomedical devices, recent advances in stem cell research have made several cell sources available that can be used to obtain cardiac muscle cells. There is ever growing evidence that multipotent adult stem cells capable of differentiation to cardiac myocytes are present in the adult heart [6]. Stem cells have been isolated from human heart biopsy specimen and expanded in the form of cardiospheres that are shown to exhibit cardiac properties [48]. Differentiation of human embryonic stem cells as well as human induced pluripotent stem cells into functional cardiomyocytes have also been demonstrated in recent years [77]. These cell sources can potentially be utilized in future to tissue engineer muscular pumps that are powered by cells derived from patients.

Appendix A

Error in Finding the Tube Profile

Uncertainties are inevitable consequences of any measurement. It is important to have an understanding of the relative magnitude and the sources of such errors associated with a measurement in order to make inferences on the significance of the collected data. In the case of the edge detection algorithm and measurements of the temporally varying diameter of the tissue-engineered constructs, the primary sources of uncertainty are the discretization of the images and variations in the illumination of the construct during image capture.

In order to quantify the error associated with the edge detection algorithm of Section 3.6.1, images of a stationary translucent silicone tube were captured at a frame rate of 30 fps for a duration of 20 seconds, and the images were processed using the edge detection program described previously. The diameter of the tube was calculated by subtracting the coordinates of the lower boundary from the upper one. For the stationary tube, one would expect that these values would be time invariant and any time variations in the tube diameter are considered as the combined error in finding the tube boundaries. Plots of Figure A.1 quantify this error.

The top plot in Figure A.1 depicts the resulting deviations from the mean diameter in pixels for the 600 images that were analyzed. The outer lines (blue) represent an upper and lower bound around the mean diameter. The diameter from any detected profile would lie between these bounds. The inner lines (red) represent the standard deviation from mean diameter. Variations upward of 4 pixels exist at certain point along the tube. With the low magnifications used for imaging the tubes, such uncertainties would be sufficient to render the results inconclusive without any further

manipulation of the data.

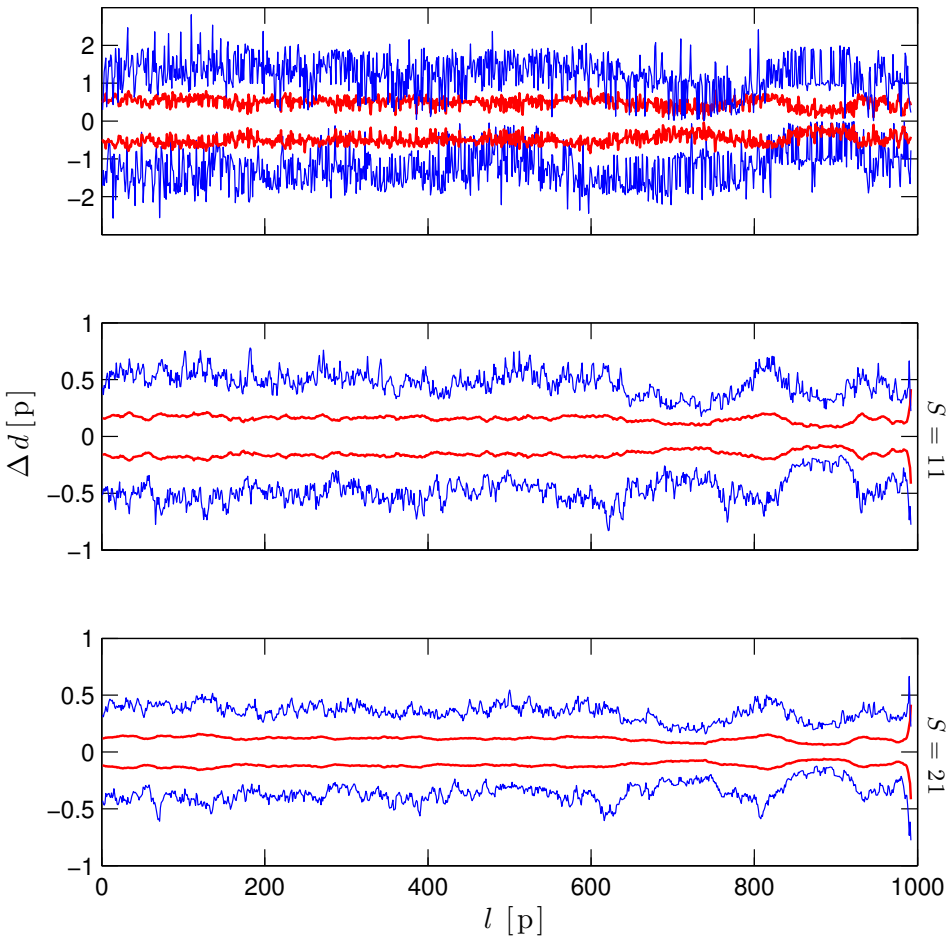

Figure A.1. Error associated with the edge detection algorithm. Top: Lower and upper bounds on variations from mean diameter. Middle and bottom: Application of a moving average filter to the diameter reduces the uncertainties to sub-pixel values.

The spikes in Δd suggest that not all points along the diameter have the same level of uncertainty associated with them. This observation motivated the use of a moving average low-pass filter which utilizes the continuity in diameter for adjacent points to reduce the error associate with edge detection. For the discrete sequence $d = d(1:n)$, the moving average, $\bar{\bar{d}}$, at a point i is defined as

$$\overline{\overline{d}} = \begin{cases} d(i) & \text{if } i = 1, \\ \frac{\sum d(1:2i-1)}{2i+1} & \text{if } i - s < 1, \\ \frac{\sum d\left(i-\frac{s-1}{2}:i+\frac{s-1}{2}\right)}{s} & \text{if } i - s > 1 \text{ and } i + s < n, \\ \frac{\sum d(n-2i:n)}{2i+1} & \text{if } i + s > n, \\ d(n) & \text{if } i = n, \end{cases} \tag{A.1}$$

where s denotes the span of the moving average.

The middle and bottom plots of Figure A.1 represent the variations from mean after applying the moving average filter of Equation (A.1) to the diameter at each time point. As can be seen from the plots, as the span of the filter increases to a value of 21, the uncertainties reduce to sub-pixel values. For this reason, a minimum span value of 21 is used in all the processed data to improve the confidence level in the data. It should be noted that this filtering does not improve the reliability of the data at the extreme end points of the sequence as is evident from Equation (A.1).

Appendix B

Calculating the Depth of Field for the Stereomicroscope in Relation to PTV Software

The optical nature of the stereomicroscope provides a wide field of view as well as a large depth of field. The large depth of field of the microscope has implications on using the tracked tracer particles in calculations of the fluid velocities and flow rates induced by the pump. Due to this artifact, particles in different z levels that have different velocities are observable through the optics and recorded in the same image. The result of this volumetric sampling is a spread in the measured particle velocities as can be seen in Figures 4.11 and 4.20.

In order to measure the depth of field as it relates to the particle detection software, a dilution of the tracer particles suspended in water were immobilized between two glass slides and were visualized with the stereomicroscope at the magnification used for particle tracking in the experiments as described in Section 3.5. The microscope was focused on the particles and an image was captured at this focal position, z_0. The objective was subsequently moved in several 50 µm steps away or towards the slide, and images were captured from the out-of-focus particles at each level. These images were analyzed by the particle tracking software, and the number of particles recognized at each out-of-focus distance was obtained, as plotted in Figure B.1. As can be seen from the plot, a large fraction of the particles detected at the focal plane are still recognized at near and far out-of-focus planes. In fact, more than 50% of the particles are detectable in a ±250 µm window of the focal plane. Furthermore, a smaller fraction of the original particles are detected in the 250–350 µm

window.

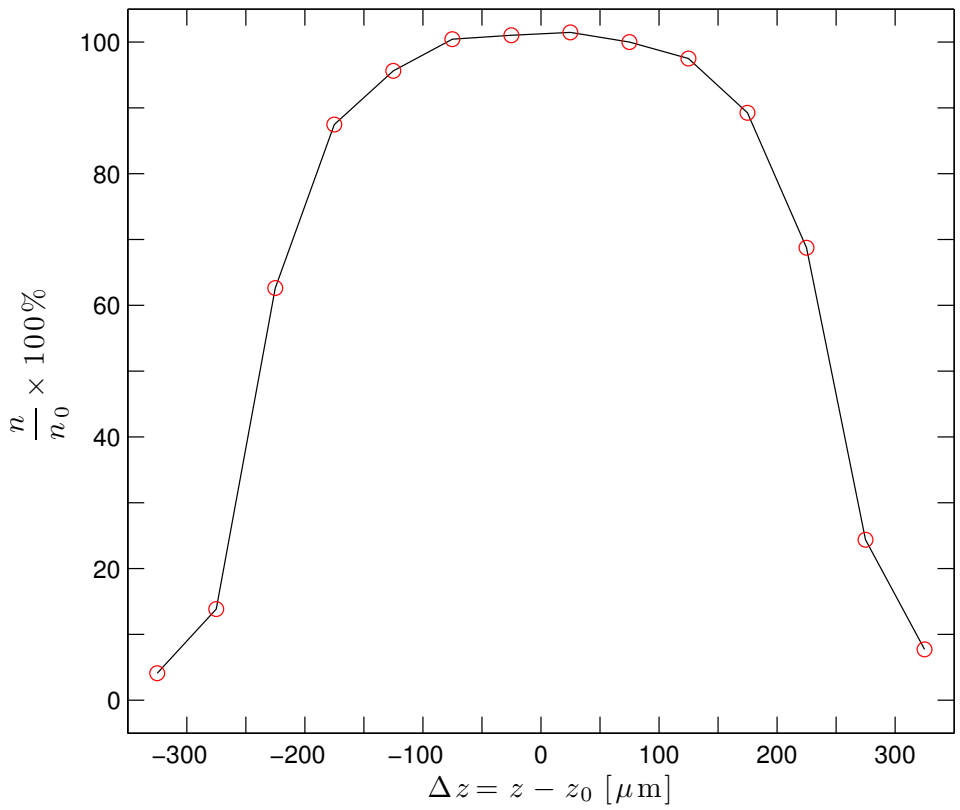

Figure B.1. The fraction of particles recognized by the particle tracking program at out-of-focus planes normalized by the number of particles detected at the focal plane z_0.

Bibliography

[1] S. Alom Ruiz and C. S. Chen. Microcontact printing: A tool to pattern. *Soft Matter*, 3:168–177, 2007.

[2] D. Auerbach, W. Moehring, and M. Moser. An analytic approach to the Liebau problem of valveless pumping. *Cardiovascular Engineering: An International Journal*, 4(2):201–207, 2004.

[3] I. Avrahami and M. Gharib. Computational studies of resonance wave pumping in compliant tubes. *Journal of Fluid Mechanics*, 608:139–160, 7 2008.

[4] Y. Bar-Cohen. Biomimetics–using nature to inspire human innovation. *Bioinspiration & Biomimetics*, 1(1):P1–P12, 2006.

[5] T. A. Baudino, A. McFadden, C. Fix, J. Hastings, R. Price, and T. K. Borg. Cell patterning: Interaction of cardiac myocytes and fibroblasts in three-dimensional culture. *Microscopy and Microanalysis*, 14:117–125, 2008.

[6] A. P. Beltrami, L. Barlucchi, D. Torella, M. Baker, F. Limana, S. Chimenti, H. Kasahara, M. Rota, E. Musso, K. Urbanek, A. Leri, J. Kajstura, B. Nadal-Ginard, and P. Anversa. Adult cardiac stem cells are multipotent and support myocardial regeneration. *Cell*, 114(6):763–776, 2003.

[7] T. K. Borg and J. B. Caulfield. Collagen in the heart. *Texas Reports on Biology and Medicine*, 39:321–333, 1979.

[8] T. K. Borg and J. B. Caulfield. The collagen matrix of the heart. *Federation Proceedings*, 40(7):2037–2041, 1981.

[9] R. D. Brown, S. K. Ambler, M. D. Mitchell, and C. S. Long. The cardiac fibroblast: Therapeutic target in myocardial remodeling and failure. *Annual Review of Pharmacology and Toxicology*, 45(1):657–687, 2005.

[10] J. E. Butler, P. D. Majors, and R. T. Bonnecaze. Observations of shear-induced particle migration for oscillatory flow of a suspension within a tube. *Physics of Fluids*, 11(10):2865–2877, 1999.

[11] P. Camelliti, T. K. Borg, and P. Kohl. Structural and functional characterisation of cardiac fibroblasts. *Cardiovascular Research*, 65(1):40–51, 2005.

[12] K. B. Campbell and M. Chandra. Functions of stretch activation in heart muscle. *The Journal of General Physiology*, 127(2):89–94, 2006.

[13] V. Chan, K. Park, M. B. Collens, H. Kong, T. A. Saif, and R. Bashir. Development of miniaturized walking biological machines. *Scientific Reports*, 2:1–7, 2012.

[14] J. C. Crocker and D. G. Grier. Methods of digital video microscopy for colloidal studies. *Journal of Colloid and Interface Science*, 179(1):298–310, 1996.

[15] R. G. Dennis and H. Herr. *Biomimetics: Biologically Inspired Technologies*, chapter "Engineered muscle actuators: Cells and tissues", pages 243–266. CRC, 2006.

[16] B. Duan, L. A. Hockaday, K. H. Kang, and J. T. Butcher. 3D bioprinting of heterogeneous aortic valve conduits with alginate/gelatin hydrogels. *Journal of Biomedical Materials Research Part A*, 101A(5):1255–1264, 2013.

[17] A. J. Engler, C. Carag-Krieger, C. P. Johnson, M. Raab, H.-Y. Tang, D. W. Speicher, J. W. Sanger, J. M. Sanger, and D. E. Discher. Embryonic cardiomyocytes beat best on a matrix with heart-like elasticity: Scar-like rigidity inhibits beating. *Journal of Cell Science*, 121(22):3794–3802, 2008.

[18] A. J. Engler, M. A. Griffin, S. Sen, C. G. Bnnemann, H. L. Sweeney, and D. E. Discher. Myotubes differentiate optimally on substrates with tissue-like stiffness: Pathological implications for soft or stiff microenvironments. *The Journal of Cell Biology*, 166(6):877–887, 2004.

[19] A. W. Feinberg, A. Feigel, S. S. Shevkoplyas, S. Sheehy, G. M. Whitesides, and K. K. Parker. Muscular thin films for building actuators and powering devices. *Science*, 317(5843):1366–1370, 2007.

[20] A. S. Forouhar. *Dynamic views of structure and function during heart morphogenesis*. PhD thesis, California Institute of Technology, 2006.

[21] A. S. Forouhar, M. Liebling, A. Hickerson, A. Nasiraei-Moghaddam, H.-J. Tsai, J. R. Hove, S. E. Fraser, M. E. Dickinson, and M. Gharib. The embryonic vertebrate heart tube is a dynamic suction pump. *Science*, 312(5774):751–753, 2006.

[22] L. E. Freed and G. Vunjak-Novakovic. *Principles of Tissue Engineering*, chapter "Tissue engineering bioreactors", pages 143–156. Academic Press, 2000.

[23] R. I. Freshney. *Culture of Animal Cells: A Manual of Basic Technique and Specialized Applications*. Wiley-Liss, 2005.

[24] G. Gaudesius, M. Miragoli, S. P. Thomas, and S. Rohr. Coupling of cardiac electrical activity over extended distances by fibroblasts of cardiac origin. *Circulation Research*, 93(5):421–428, 2003.

[25] S. Gerecht-Nir, M. Radisic, H. Park, C. Cannizzaro, J. Boublik, R. Langer, G. Vunjak-Novakovic, et al. Biophysical regulation during cardiac development and application to tissue engineering. *The International Journal of Developmental Biology*, 50(2-3):233–243, 2006.

[26] R. C. Gonzalez, R. E. Woods, and S. L. Eddins. *Digital Image Processing Using MATLAB*. Gatesmark Publishing, 2009.

[27] A. Grosberg, P. W. Alford, M. L. McCain, and K. K. Parker. Ensembles of engineered cardiac tissues for physiological and pharmacological study: Heart on a chip. *Lab on a Chip*, 11:4165–4173, 2011.

[28] M. A. Harrison and I. F. Rae. *General Techniques of Cell Culture*. Cambridge University Press, 1997.

[29] A. Hickerson, D. Rinderknecht, and M. Gharib. Experimental study of the behavior of a valveless impedance pump. *Experiments in Fluids*, 38(4):534–540, 2005.

[30] A. I. Hickerson. *An experimental analysis of the characteristic behaviors of an impedance pump*. PhD thesis, California Institute of Technology, 2005.

[31] A. I. Hickerson and M. Gharib. On the resonance of a pliant tube as a mechanism for valveless pumping. *Journal of Fluid Mechanics*, 555:141–148, 4 2006.

[32] M. C. Hiles, S. F. Badylak, L. A. Geddes, K. Kokini, and R. J. Morff. Porosity of porcine small-intestinal submucosa for use as a vascular graft. *Journal of Biomedical Materials Research*, 27(2):139–144, 1993.

[33] S. Hur, Y. Zhao, Y.-S. Li, E. Botvinick, and S. Chien. Live cells exert 3-dimensional traction forces on their substrata. *Cellular and Molecular Bioengineering*, 2(3):425–436, 2009.

[34] I. Johnson and M. T. Spence, editors. *Molecular Probes Handbook, A Guide to Fluorescent Probes and Labeling Technologies*. Life Technologies, 2010.

[35] R. D. Kamm, R. M. Nerem, and K. J. Hsia. Cells into systems. *ASME Mechanical Engineering Magazine*, 132:30–34, 2010.

[36] I. Karassik, J. Messina, P. Cooper, and C. Heald. *Pump Handbook*. McGraw-Hill, 2007.

[37] V. Kasyanov, J. J. Sistino, T. C. Trusk, R. R. Markwald, and V. Mironov. *Bioreactors for Tissue Engineering*, chapter "Perfusion bioreactors for cardiovascular tissue engineering", pages 285–307. Springer, 2005.

[38] A. M. Katz. *Physiology of the Heart*. Lippincott Williams & Wilkins, 2001.

[39] L. Khait, L. Hecker, N. Blan, G. Coyan, F. Migneco, Y.-C. Huang, and R. Birla. Getting to the heart of tissue engineering. *Journal of Cardiovascular Translational Research*, 1(1):71–84, 2008.

[40] H. Kubo, T. Shimizu, M. Yamato, T. Fujimoto, and T. Okano. Creation of myocardial tubes using cardiomyocyte sheets and an in vitro cell sheet-wrapping device. *Biomaterials*, 28(24):3508–3516, 2007.

[41] G. C. Lantz, S. F. Badylak, M. C. Hiles, A. C. Coffey, L. A. Geddes, K. Kokini, G. E. Sandusky, and R. J. Morff. Small intestinal submucosa as a vascular graft: A review. *Journal of Investigative Surgery*, 6(3):297–310, 1993.

[42] J. Layland and J. C. Kentish. Positive force- and [ca2+]i-frequency relationships in rat ventricular trabeculae at physiological frequencies. *American Journal of Physiology–Heart and Circulatory Physiology*, 276(1):H9–H18, 1999.

[43] B. Lewartowski and B. Pytkowski. Cellular mechanism of the relationship between myocardial force and frequency of contractions. *Progress in Biophysics and Molecular Biology*, 50(2):97–120, 1987.

[44] G. Liebau. Über ein ventilloses pumpprinzip. *Naturwissenschaften*, 41(14):327–327, 1954.

[45] P. S. McFetridge and J. B. Chaudhuri. *Bioreactors for Tissue Engineering*, chapter "Design of vascular graft bioreactors", pages 269–283. Springer, 2005.

[46] T. B. McPherson and S. F. Badylak. Characterization of fibronectin derived from porcine small intestinal submucosa. *Tissue Engineering*, 4(1):75–83, 1998.

[47] J. A. Meier. *A novel experimental study of a valveless impedance pump for applications at lab-on-chip, microfuidic, and biomedical device size scales*. PhD thesis, California Institute of Technology, 2011.

[48] E. Messina, L. De Angelis, G. Frati, S. Morrone, S. Chimenti, F. Fiordaliso, M. Salio, M. Battaglia, M. V. Latronico, M. Coletta, E. Vivarelli, L. Frati, G. Cossu, and A. Giacomello. Isolation and expansion of adult cardiac stem cells from human and murine heart. *Circulation Research*, 95(9):911–921, 2004.

[49] A. D. Metcalfe and M. W. Ferguson. Tissue engineering of replacement skin: The crossroads of biomaterials, wound healing, embryonic development, stem cells and regeneration. *Journal of The Royal Society Interface*, 4(14):413–437, 2007.

[50] T. Mikawa. *Heart Development*, chapter "Cardiac lineages", pages 19–33. Academic Press, 1999.

[51] M. Moser, J. W. Huang, G. S. Schwarz, T. Kenner, and N. Abraham. Impedance defined flow: Generalization of William Harvey's concept of the circulation–370 years later. *International Journal of Cardiovascular Medicine and Science*, 1(3/4):205–211, 1998.

[52] J. C. Nawroth, H. Lee, A. W. Feinberg, C. M. Ripplinger, M. L. McCain, A. Grosberg, J. O. Dabiri, and K. K. Parker. A tissue-engineered jellyfish with biomimetic propulsion. *Nature Biotechology*, 30(8):792–797, 2012.

[53] C. Norotte, F. S. Marga, L. E. Niklason, and G. Forgacs. Scaffold-free vascular tissue engineering using bioprinting. *Biomaterials*, 30(30):5910–5917, 2009.

[54] H. C. Ott, T. S. Matthiesen, S.-K. Goh, L. D. Black, S. M. Kren, T. I. Netoff, and D. A. Taylor. Perfusion-decellularized matrix: Using nature's platform to engineer a bioartificial heart. *Nature Medicine*, 14(2):213–221, Feb. 2008.

[55] D. Rinderknecht, A. I. Hickerson, and M. Gharib. A valveless micro impedance pump driven by electromagnetic actuation. *Journal of Micromechanics and Microengineering*, 15(4):861–866, 2005.

[56] D. G. Rinderknecht. *Development of a microimpedance pump for pulsatile flow transport: Part 1: Flow characteristics of the microimpedance pump. Part 2: A systematic study of steady and pulsatile transport in microscale cavities.* PhD thesis, California Institute of Technology, 2008.

[57] M. V. Risbud and M. Sittinger. Tissue engineering: Advances in in vitro cartilage generation. *Trends in Biotechnology*, 20(8):351–356, 2002.

[58] R. Roeder, J. Wolfe, N. Lianakis, T. Hinson, L. Geddes, and J. Obermiller. Compliance, elastic modulus, and burst pressure of small-intestine submucosa (SIS), small-diameter vascular grafts. *Journal of Biomedical Materials Research*, 47(1):65–70, 1999.

[59] S. S. Rogers, T. A. Waigh, X. Zhao, and J. R. Lu. Precise particle tracking against a complicated background: polynomial fitting with gaussian weight. *Physical Biology*, 4(3):220–227, 2007.

[60] H. Sekine, T. Shimizu, J. Yang, E. Kobayashi, and T. Okano. Pulsatile myocardial tubes fabricated with cell sheet engineering. *Circulation*, 114(1 suppl):I87–I93, 2006.

[61] W. W. Sharp, D. G. Simpson, T. K. Borg, A. M. Samarel, and L. Terracio. Mechanical forces regulate focal adhesion and costamere assembly in cardiac myocytes. *American Journal of Physiology–Heart and Circulatory Physiology*, 273(2):H546–H556, 1997.

[62] M. S. Spach and J. P. Boineau. Microfibrosis produces electrical load variations due to loss of side-to-side cell connections: A major mechanism of structural heart disease arrhythmias. *Pacing and Clinical Electrophysiology*, 20(2):397–413, 1997.

[63] J. P. Stegemann, S. N. Kaszuba, and S. L. Rowe. Review: Advances in vascular tissue engineering using protein-based biomaterials. *Tissue Engineering*, 13(11):2601–2613, 2007.

[64] G. Steiger. Stretch activation and myogenic oscillation of isolated contractile structures of heart muscle. *Pflügers Archiv*, 330(4):347–361, 1971.

[65] J. E. Stelzer, L. Larsson, D. P. Fitzsimons, and R. L. Moss. Activation dependence of stretch activation in mouse skinned myocardium: Implications for ventricular function. *The Journal of General Physiology*, 127(2):95–107, 2006.

[66] Y. Tanaka, K. Morishima, T. Shimizu, A. Kikuchi, M. Yamato, T. Okano, and T. Kitamori. An actuated pump on-chip powered by cultured cardiomyocytes. *Lab on a Chip*, 6:362–368, 2006.

[67] Y. Tanaka, K. Sato, T. Shimizu, M. Yamato, T. Okano, and T. Kitamori. A micro-spherical heart pump powered by cultured cardiomyocytes. *Lab on a Chip*, 7:207–212, 2007.

[68] N. Tandon, C. Cannizzaro, P.-H. G. Chao, R. Maidhof, A. Marsano, H. T. H. Au, M. Radisic, and G. Vunjak-Novakovic. Electrical stimulation systems for cardiac tissue engineering. *Nature Protocols*, 4(2):155–173, 2009.

[69] M. J. Taylor. *Advances in Biopreservation*, chapter "Biology of cell survival in the cold: The basis for biopreservation of tissues and organs", pages 15–62. CRC Press, 2006.

[70] L. Terracio, A. Tingström, W. H. Peters, and T. K. Borg. A potential role for mechanical stimulation in cardiac development. *Annals of the New York Academy of Sciences*, 588(1):48–60, 1990.

[71] S. Vogel. *Vital Circuits*. Oxford University Press, 1992.

[72] S. Vogel. Nature's pumps. *American Scientist*, 82:464–471, 1994.

[73] Z. Q. Wang, Y. Watanabe, and A. Toki. Experimental assessment of small intestinal submucosa as a small bowel graft in a rat model. *Journal of Pediatric Surgery*, 38(11):1596–1601, 2003.

[74] J. Xi, J. J. Schmidt, and C. D. Montemagno. Self-assembled microdevices driven by muscle. *Nature Materials*, 4(2):180–184, 2005.

[75] J. H. Yost. *Heart Development*, chapter "Establishing cardiac left-right asymmetry", pages 373–389. Academic Press, 1999.

[76] M. Zamir. *The Physics of Pulsatile Flow*. Springer-Verlag, 2000.

[77] J. Zhang, G. F. Wilson, A. G. Soerens, C. H. Koonce, J. Yu, S. P. Palecek, J. A. Thomson, and T. J. Kamp. Functional cardiomyocytes derived from human induced pluripotent stem cells. *Circulation Research*, 104(4):e30–e41, 2009.